UNIVERSIDADE FEDERAL DE PERNAMBUCO
CENTRO DE CIÊNCIAS EXATAS E DA NATUREZA
PROGRAMA DE PÓS-GRADUAÇÃO EM FÍSICA

Caio Nascimento D'Azevedo

INVESTIGATION OF EXCHANGE BIAS IN THIN FILMS BY FERROMAGNETIC RESONANCE SPECTROSCOPY

Recife
2024

Caio Nascimento D'Azevedo

INVESTIGATION OF EXCHANGE BIAS IN THIN FILMS BY FERROMAGNETIC RESONANCE SPECTROSCOPY

Dissertação apresentada ao Programa de Pós-Graduação em Física da Universidade Federal de Pernambuco, como requisito parcial para a obtenção do título de Mestre em Física.

Área de concentração: Física da Matéria Condensada e de Materiais

Orientador: Sergio Machado Rezende

Recife

2024

Catalogação na fonte
Bibliotecária Nataly Soares Leite Moro, CRB4-1722

D277i D'Azevedo, Caio Nascimento
Investigation of exchange bias in thin films by ferromagnetic resonance spectroscopy / Caio Nascimento D'Azevedo. – 2024.
106 f.: il., fig., tab.

Orientador: Sergio Machado Rezende.
Dissertação (Mestrado) – Universidade Federal de Pernambuco. CCEN, Física, Recife, 2024.
Inclui referências e apêndice.

1. Física da matéria condensada e de materiais. 2. Spintrônica. 3. Exchange bias. 4. Ressonância ferromagnética. 5. Antimônio. 6. Recozimento com campo magnético I. Rezende, Sergio Machado (orientador). II. Título.

530.41 CDD (23. ed.) UFPE- CCEN 2024 - 87

CAIO NASCIMENTO D'AZEVEDO

INVESTIGATION OF EXCHANGE BIAS IN THIN FILMS BY FERROMAGNETIC RESONANCE SPECTROSCOPY

Dissertação apresentada ao Programa de Pós-Graduação em Física da Universidade Federal de Pernambuco, como requisito parcial para a obtenção do título de Mestre em Física.

Data de aprovação: 24/07/2024.

BANCA EXAMINADORA

_____

Prof. Dr. Sergio Machado Rezende
Orientador
Universidade Federal de Pernambuco

_____

Prof. Dr. Fernando Luis de Araujo Machado
Examinador Interno
Universidade Federal de Pernambuco

_____

Prof. Dr. Roberto Lázaro Rodríguez Suárez
Examinador Externo
Pontificia Universidad Católica de Chile

AGRADECIMENTOS

Primeiramente à minha esposa, Márcia, por todo o apoio, encorajamento e inspiração nesta trajetória. À minha família pelo suporte incondicional. Ao meu orientador, Professor Sergio Machado Rezende, pelos conhecimentos e visões passados, bem como pela prontidão em dar as diretivas do percurso quando necessário. Aos Professores Fernando Luis de Araujo Machado e Roberto Lázaro Rodríguez Suárez, membros da banca examinadora, pelas ótimas sugestões que em muito melhoraram a versão final do texto.

Aos meus colegas de laboratório que fizeram toda a diferença. Daniel Souto e Elias Abrão por me introduzirem ao labotatório e pela disponibilidade e por tirar todo tipo de dúvidas. A Jefferson pela grande ajuda na preparação de amostras, programação do ajuste numérico e discussões divertidas. Edy pelos conhecimentos passados sobre preparação de filmes de YIG, e várias coisas cotidianas. Eduardo e João pela ajuda na deposição das amostras e pelos conhecimentos passados sobre FMR. A Diego, Carlos e Laurertan pela ajuda na execução dos tratamentos térmicos, e a Kacio por preparar o forno de LPE que expandiu as possibilidades de fabricação de amostras no nosso laboratório.

Por fim, agradeço ao Conselho Nacional de Desenvolvimento Científico e Tecnológico (CNPq), entidade ligada ao Ministério da Ciência, Tecnologia e Inovação (MCTI) do Brasil, pelo investimento na ciência brasileira que acabou por possibilitar o desenvolvimento desta, e muitas outras dissertações de mestrado.

RESUMO

Neste trabalho emprega-se a técnica experimental espectroscopia de ressonância ferromagnética para investigar mecanismos de anisotropia magnética em filmes finos de junção ferromagneto/antiferromagneto, bem como a influência de intercamadas de antimônio nestes sistemas. O antimônio é um semimetal diamagnético conhecido por possuir estados topológicos de superfície e propriedades quânticas curiosas. Espectroscopia de amostra vibratória também foi utilizada para confirmar, através das curvas de magnetização, a existência ou não de exchange bias. Na primeira seção experimental foram avaliados os efeitos do tratamento térmico conhecido como recozimento com campo magnético na estrutura cristalina e nas anisotropias magnéticas de bicamadas YIG/IrMn, a fim de estabelecer procedimentos que resultem em propriedades desejadas, com ênfase na indução de anisotropia unidirecional. Verificou-se que as anisotropias cúbica e uniaxial tornaram-se mais nítidas após o recozimento, indicando melhoria da estrutura cristalina. Além disso, um aumento expressivo de sete vezes no campo efetivo de exchange bias foi alcançado em uma das amostras. Já na segunda seção, foram encontradas evidências de exchange bias em tricamadas FM/Sb/AFM para dois FM distintos (YIG e Py) e várias espessuras de antimônio na ordem de algumas dezenas de nanômetros. Aqui apresento a hipótese de um acoplamento entre os spins travados por spin-momentum locking no antimônio e os spins do FM. Spin-momentum locking corresponde ao travamento das orientações dos spins perpendicularmente ao momento linear dos elétrons por meio do espalhamento Rashba, assim gerando polarização de spin na interface. Assumindo que o antimônio esteja mantendo seus estados de superfície, a corrente bombeada por spin pumping no antimônio estaria topologicamente travada, o que poderia resultar em um acoplamento com os spins do FM por meio da interação de exchange. Se confirmada, a indução de exchange bias mediada por spin-momentum locking possibilitaria aplicações interessantes como o controle de exchange bias através da corrente de superfície no antimônio.

Palavras-chave: spintrônica; exchange bias; ressonância ferromagnética; antimônio; recozimento com campo magnético; spin-momentum locking.

ABSTRACT

In this work the ferromagnetic resonance spectroscopy experimental technique is employed to investigate the mechanisms of magnetic anisotropy in ferromagnet/antiferromagnet thin films, as well as the influence of antimony interlayers in such systems. Antimony is a diamagnetic semimetal known to possess topological surface states and unique quantum properties. Vibrating sample spectroscopy was also used to confirm the existence of exchange bias by looking at their magnetization curves. Regarding the first experimental section, the effect of magnetic annealing on the crystal lattice and magnetic anisotropy of YIG/IrMn bilayers was evaluated in order to establish procedures that give certain desired properties, with special attention to the induction of unidirectional anisotropy. It was found that cubic and uniaxial anisotropies became neater after annealing, indicating improvement of the crystallographic structure. Furthermore, an expressive sevenfold increase of the exchange bias effective field could be accomplished for one of the samples. In the second part, evidence of exchange bias in FM/Sb/AFM trilayers was gathered in two different FM (YIG and Py), for several antimony thicknesses in the order of a few dozens of nanometers. I hereby present the hypothesis that a coupling between the spins from antimony's spin-momentum locked electrons and the FM electrons might be occurring. Spin-momentum locking stands for spins' orientations being locked perpendicular to the electrons' linear momentum due to Rashba spin-orbit splitting, thereby generating spin polarization at the interface. Assuming antimony to be hosting surface states, the spin pumped current from Sb would be topologically locked, which could result in coupling with the FM spins by means of the exchange interaction. If confirmed, the induction of exchange bias mediated by spin-momentum locking could open new avenues in spintronics, such as the control of exchange bias through the surface currents in antimony.

Keywords: spintronics; exchange bias; ferromagnetic resonance; antimony; magnetic annealing; spin-momentum locking.

CONTENTS

1 INTRODUCTION

Magnetism is one of the most active research fields in contemporary condensed matter physics. Beyond its fundamental role in the electromagnetic theory that has rendered a variety of technologies and insights -- such as electromagnetic wave communications, electric generators/motors, the theory of relativity, etc. -- magnetism is ingrained all the way down to the atomic configurations and the structure of matter, motivating basic research on its quantum mechanical origins, dynamic excitations, and thermodynamic properties; as well as drawing attention for its promising applications in material technology and electronics.

The most widespread application of magnetism in modern electronics arguably is the hard disk drive (HDD), that exploits the accumulative nature of some magnetic materials' hysteresis loops to store non-volatile information. With the discovery of the giant magnetoresistance (GMR) effect, efficient control of electric currents through the relative orientation of magnetization of multilayers was realized, causing the magnetic storage capacity of HDD to reach the gigabyte range. This breakthrough propelled research aiming next-generation electronics that could employ, in addition to the electron's charge, the magnetism of the electronic spin, culminating in the field called spintronics. Contemporary spintronics is largely about the manipulation of spin currents (i.e.: flow of spin polarization) to transport signals, exert torque on magnetic materials or to interact with charge and spin waves, having unveiled many microscopic phenomena (e.g.: the spin Hall, Rashba-Edelstein, and spin Seebeck effects, etc.) and materials (e.g.: topological insulators); as well as bringing promising technological prospects such as magnetic random-access memory (MRAM), terahertz oscillators, quantum computing and a myriad of spintronic sensors.

2 THEORETICAL BACKGROUND

2.1 Overview

In general, all substances display at least one of five basic kinds of magnetism, namely: **diamagnetism**, **paramagnetism**, **ferromagnetism**, **ferrimagnetism** and **antiferromagnetism**. Diamagnetism is due entirely to the orbital motion of electrons

associated with Larmor precession. For instance, in the case of metals, the atomic cores have completely filled subshells resulting in a small, negative susceptibility that expells magnetic fields. Paramagnetism refers to a system in which each atom carries a magnetic moment, but those point in all directions, resulting in no net magnetization. The complete disorder of atomic moments comes about because there is no magnetic interaction between neighboring atoms on one hand, and because the thermal agitation causes the moments to be aligned randomly on the other.

The remaining three kinds (ferro, ferri and antiferromagnetism) differ from the previous two on that they exhibit long-range order due to the exchange interaction (Section 2.6), a quantum electrostatic effect that bounds neighboring spins very much as if they were connected by springs. In general, a solid will be ferromagnetic if its atoms carry a magnetic moment, and if the exchange interaction causes these moments to align parallel in the long range; on the other hand the material will be antiferromagnetic if the moments align antiparallel. At last, ferrimagnetism originates from the competition between the magnetic moment of different groups of ions, resulting in non-zero net magnetization -- and this is why they are only found in compounds or alloys. Many ferrimagnets offer atractive properties for magnetic applications at high frequencies, such as the yittrium iron garnet (YIG) that has been for many years the prototype material for the study of the dynamics of spin excitations. This classification is summarized in terms of the magnetic susceptibilities in **Table 1**, and illustrated in **Figure 1**.

Table 1 - Summary of susceptibilities for different kinds of magnetism.

	Diamagnetism	Paramagnetism	Ferromagnetism and ferrimagnetism
Susceptibility	< 0	$\gtrsim 0$	$\gg 0$

Source: Chih-Wen (1977).

Figure 1 – Spin arrangement in a crystal or domain illustrating (a) paramagnetism, (b) ferromagnetism, (c) antiferromagnetism and (d) ferrimagnetism.

(a) (b) (c) (d)

Source: Chih-Wen (1977).

Atoms derive their magnetic moments essentially from electrons, which are about three orders of magnitude larger than those from the nuclei. There are two sources from which an electron can obtain its magnetic moment: its orbital motion around the nucleus (Section 2.4.4), and its spin. The latter is an intrinsic form of angular momentum similar to (but emphatically not equal to) a rotation around its own axis.

The orbital magnetic moment and can be rewritten to account the quantum mechanical expression for angular momentum ($\boldsymbol{p}_l$) as in,

$$\boldsymbol{\mu}_l = -\left(\frac{e}{2m_0}\right)\boldsymbol{p}_l = -\mu_B \boldsymbol{L} \qquad \boldsymbol{p}_l = \hbar \boldsymbol{L} \qquad \boldsymbol{L} = [l(l+1)]^{1/2}\hat{\boldsymbol{l}} \tag{1}$$

Where l is the orbital momentum quantum number, $\hat{\boldsymbol{l}}$ is the versor normal to the orbit, and $\mu_B = e\hbar/2m_0 = 9.2732 \times 10^{-24}\ \mathrm{A \cdot m^2}$ is the Bohr magneton, the conventional unit of magnetic moment.

Extrapolating from their orbital moment counterparts, the spin magnetic moment and angular momentum may be defined as,

$$\boldsymbol{\mu}_s = -g\mu_B \boldsymbol{S} \qquad \boldsymbol{p}_s = \hbar \boldsymbol{S} \qquad \boldsymbol{S} = [s(s+1)]^{1/2}\hat{\boldsymbol{\sigma}} \tag{2}$$

Where s is the spin momentum quantum number, $\hat{\boldsymbol{\sigma}}$ is the versor in the direction of spin angular momentum, and g is the Landé factor (≈ 2 for the electron's spin). The negative sign comes from that the electron has negative charge. Despite their similarities, unlike the orbital mortion, the electron's spin is strictly a quantum-mechanical effect.

Due to the so-called spin-orbit interaction (Section 2.4.5) the orbital and spin magnetic moments combine into a resultant magnetic moment, also known as *ls* coupling. The result is that both the spin and orbital axes will precess as one with the same angular velocity, and in the same direction about a common axis (**Figure 2**). The resultant angular momentum $\boldsymbol{p}_j$ is, thereby,

$$\boldsymbol{\mu}_j = -g\mu_B \boldsymbol{J}$$
$$\boldsymbol{p}_j = \hbar \boldsymbol{J} \qquad\qquad \boldsymbol{J} = [j(j+1)]^{1/2}\hat{\boldsymbol{j}} \tag{3}$$

Where $j = l + s$ is the total angular momentum quantum number.

Figure 2 - Vector model showing the spin-orbital coupling for a bound electron.

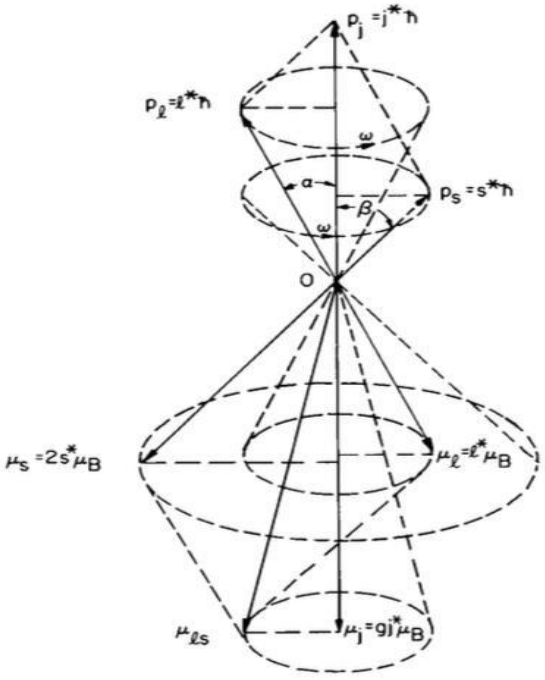

Source: Brailsford (1966).

2.2 Atomic configuration and magnetism

In the periodic table, groups of elements can be asigned to certain kinds of magnetism depending on their atomic configurations. For instance, inert gases and noble metals (Cu, Ag and Au) are diamagnetic; alkali metals (Li, Na, K and Rb) and all transition metals except Fe, Co and Ni are paramagnetic. Besides the conventional trio Fe, Co and Ni, six elements in the lanthanide series (Gd, Tb, Dy, Ho, Er and Tm)

become ferromagnetic at $\sim 20\,°\mathrm{C}$ and subzero temperatures. The list of magnetic materials, nevertheless, is infinitely long because an inlimited number of magnetic solid solutions and compounds can be formed of magnetic and certain nonmagnetic elements.

The magnetic properties of a material can be inferred from some atomic principles. For one, only electrons in the incompletely filled atomic subshell have a significant role in magnetism. Furthermore, quantum mechanics establishes that each n-th atomic shell comprises up to $2n^2$ electrons and each l subshell comprises at most $2(2l+1)$ electrons. Those principles, along with the renowned Hund's rules provide the basis to obtain the configuration of states; as well as the s, l and j values of an ion or atom, thereby giving the corresponding magnetic moment. Namely, Hund's rules are:

(1) Electrons occupy states so as to maximize the total spin, without violating Pauli's exclusion principle;
(2) Electrons occupy orbitals so as to mazimize the total orbital momentum, consistent with the first rule and the Pauli's exclusion principle;
(3) When the shell is less than half full, the total angular momentum is given by $j = |l - s|$; and, when more than half full, $j = |l + s|$. When exactly half filled $l = 0$ and s is maximum.

For instance, consider the ion Fe^{3+}, which is the key agent behind the magnetism of the yttrium iron garnet (YIG). The atom of iron comprises 26 bound electrons, but only 8 are in the subshells outside the filled $3p$ subshell. Furthermore, 2 of the 8 electrons fill the $4s$ subshell. Hence, only the remaining 6 electrons of the $3d$ subshell contribute to magnetism. Now, subtracting 3 electrons from Fe (the two $4s$ electrons and one of the six $3d$ electrons), there remain 5 electrons in the $3d$ subshell, so that $l = 0$, $s = 5/2$, and the total angular momentum is $j = 5/2$. The absence of orbital momentum results in an weak spin-orbit coupling, thereby "lightening" the inertia of the magnetic response of Fe^{3+}.

2.2.1 The yttrium iron garnet

Because YIG's magnetism is solely due to its Fe^{3+} ions, it exhibits remarkably low magnetic damping, resulting in low magnetic/acoustic losses and long spin

relaxation time, making of it arguably the best known material to the study of the dynamics of spin excitations such as spin waves (Section 2.6.1). YIG is a ferrimagnetic insulator with Currie temperature $T_C = 559\ \mathrm{K}$; lattice parameter $a \approx 1.24\ \mathrm{nm}$; and magnetization $M = 195\ \mathrm{Oe}$ at $T = 0$, and $M = 140\ \mathrm{Oe}$ at $T = 300\ \mathrm{K}$ [22,23,41].

As previously mentioned, ferrimagnetism originates from the competion of at least two magnetic moments carried by ions of different species. In the case of YIG, its conventional body centered cubic (bcc) unit cell contains eight formula units $Y_3Fe^{3+}{}_2Fe^{3+}{}_3O^{2-}{}_{12}$, with the magnetic Fe^{3+} ions occupying two asymmetric positions with respect to their O^{2-} ligands (**Figure 3**). This results in two competing tetrahedral (d) and octahedral (a) magnetic sublattices that couple antiferromagnetically *between each other*, and ferromagnetically *within themselves*. Quantitatively, this means that, provided that each of the two primitive cells have 12 ions in d-sites and 8 ions in a-sites, the 12 d-ions will align antiparallelly to the 8 a-ions, resulting in a total magnetic moment $\mu = 2 \times 4 \times (5/2) g\mu_B = 20 g\mu_B$.

Figure 3 – Crystal structure of YIG. (a) bcc lattice. (b) first octant of the unit cell of YIG, indicating the two different Fe^{3+} sites, with the tetrahedral sites in green and the octahedral sites in blue. (c) conventional unit cell of YIG, with the majority tetrahedral sites in green and the minority octahedral sites in blue.

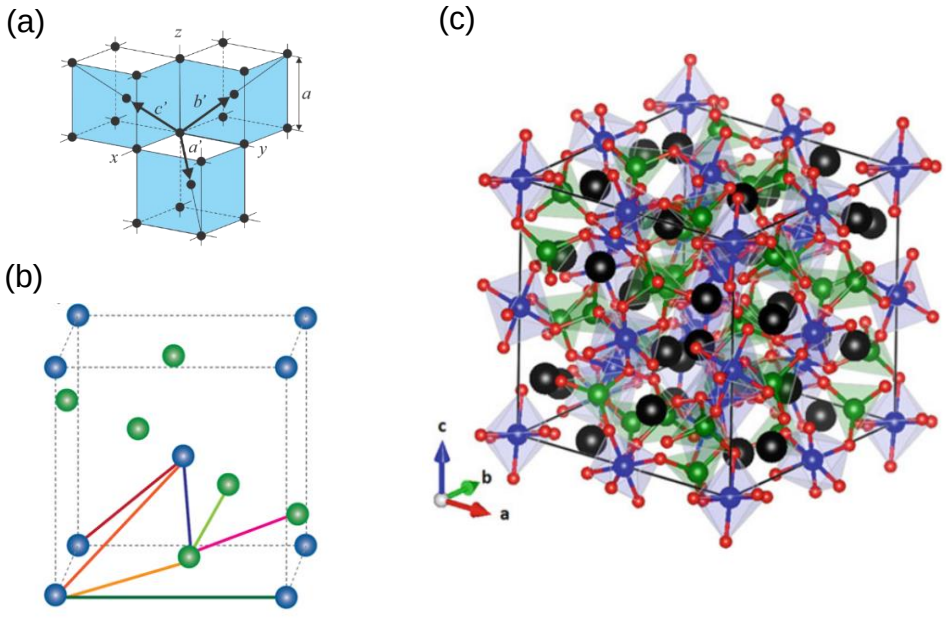

Source: (a) Rezende (2022); (b) and (c) Princep et al (2017).

Moreover, the combination of YIG's insulating and magnonic properties enable spin transmission by magnon diffusion with no motion of charges by the so-called magnonic spin currents, thereby preventing energy dissipation from ohmic losses. YIG thin films can be grown by liquid beam epitaxy, pulsed laser, and sputtering deposition.

2.3 Magnetization

Magnetic polarization is measured by the vector quantity called magnetization. The magnetization is an extensive state variable -- in contrast to magnetic field, which is intensive -- defined as the average per unit volume of the microscopic magnetic moments:

$$\mathbf{M} = \frac{1}{\mathrm{V}} \sum_{i} \boldsymbol{\mu_i} \tag{4}$$

The sum runs over all points at which there are dipole moments. The volume is chosen large enough so as to have a good macroscopic average, but small relative to the sample size so that the magnetization represents a local property. In turn, the magnetic induction $\boldsymbol{B}$ is given by the combination of $\boldsymbol{M}$ and $\boldsymbol{H}$,

$$\boldsymbol{B} = \mu_0(\boldsymbol{H} + \boldsymbol{M}) \tag{5}$$

And the magnetic field $\boldsymbol{H}$ relates to magnetization through the magnetic susceptibility tensor, which is characteristic of the medium, and not necessarily isotropic,

$$\boldsymbol{M} = \widetilde{\mathcal{X}}\boldsymbol{H} \tag{6}$$

In paramagnetic and diamagnetic materials, the susceptibility is constant, so that the magnetization increases linearly with the applied magnetic field and vanishes when the field is removed. The situation with ferromagnetis is entirely different. In an iron crystal, for instance, not only the atoms carry a magnetic moment, but also the metal is broken up into small competing regions in which all the atomic moments are coupled together in a preferential crystallographic direction, known as magnetic domains, so that the magnetization settles in a constant value even when no field is applied.

The dependence of magnetization with the magnetic field in ferromagnetic materials is therefore non-linear, and the curve that portrays this dependence is called the hysteresis loop. The shape of the histeresis loop is determined by the gradual

rotation of the domains towards the external magnetic field. For small fields, those displacements are reversible, so that when the field is removed the domains return to their initial configuration due to the demagnetizing effect (Section 2.7.3); however, stronger fields cause the material to attain its net magnetization even when the field is off, as depicted in **Figure 4**. The domais are thus said to be spontaneously magnetized.

Figure 4 – Illustration of gradual rotation of magnetic domains due to magnetic field.

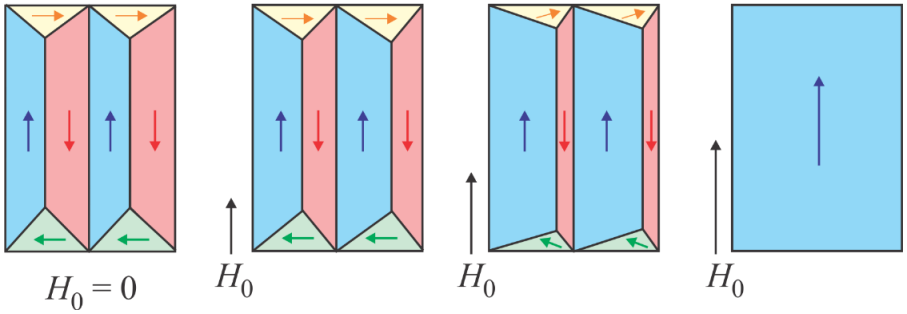

Source: Rezende (2022).

To account for the spontaneous magnetization, Weiss postulated in 1907 an intense internal field, known as the Weiss molecular field, that acts on the atomic moments of a ferromagnet together with the external field ($H_{total} = H_{external} + H_{Weiss}$). Later it was discovered that the molecular field originates from the **exchange interaction**, a quantum mechanical facet of the Coulomb interaction between neighboring electrons (Section 2.6).

Because magnetization is the macroscopic average of microscopic magnetic moments, the thermodynamic properties of a given system can be approximated by a combinatorial problem of the statistical distribution of states. According to ensemble theory, the probability that a spin chosen at random is in a given state is,

$$p_a = \frac{e^{-E_a/kT}}{\sum_i e^{-E_i/kT}} = Z^{-1} e^{-E_a/kT}$$

Where E_a corresponds to the energy of the interaction between the local spin state and the molecular field.

Assuming the exchange energy (Equation 42) to be dominated by the nearest neighbors of each electron, and the spin moments to be quantized in a given axis (thereby having only two degrees of freedom), the magnetization is given by the relative population of positive and negative spin magnetic moments in a fixed axis. In this scenario, if a spin at the i-th site was to revert its orientation (spin flip), this event would cause a change in the energy given by:

$$\Delta E_{i\to f} = E_f - E_0 \approx 4J\boldsymbol{S}_i \cdot \left(\sum_{\substack{j \in nearest \\ neighbors}} \boldsymbol{S}_j\right)$$

And the probability of this transition occurring is,

$$p_{i\to f} = \frac{Z^{-1}e^{-E_f/kT}}{Z^{-1}e^{-E_i/kT}} = e^{-\Delta E_{i\to f}/kT} \tag{7}$$

Equation 7 tells that, as temperature increases, the probability of a spin fliping event increases, so that the thermal fluctuations gradually become large enough to overcome the magnetic order created by the exchange interaction; causing the magnetization to decay until it vanishes in a paramagnetic phase. This is known as the Curie's law and the threshold temperature at which the ferromagnetic-paramagnetic phase transition occurs is called the Curie temperature.

Figure 5 – (a), (b), (c) Illustration of the relative orientations of spins at representative temperature ranges. (d) Temperature dependence of spontaneous magnetization in ferromagnets.

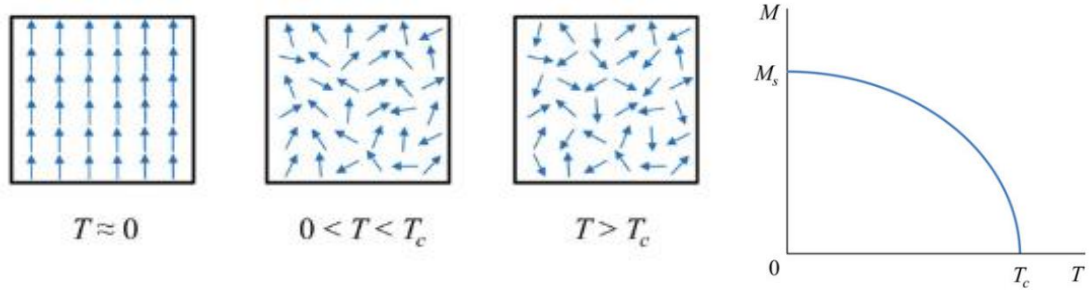

(a) (b) (c) (d)

Source: Rezende (2022).

Despite its importance in explaining the overall temperature dependence of the magnetization in ferromagnets, an important drawback of this model is that it

neglects the S_x and S_y components of the spins, thus not accounting with the so-called spin waves, which are fundamental excitations that govern the behavior of the magnetization at low temperatures.

2.4 Electromagnetic interactions

2.4.1 The Maxwell's equations

Having successfully synthesized electricity, magnetism and optics into one unified theory called electromagnetism, the Maxwell's equations lay the framework of electromagnetic interactions:

$$\boldsymbol{\nabla} \cdot \boldsymbol{D} = \rho \tag{8}$$

$$\boldsymbol{\nabla} \cdot \boldsymbol{B} = 0 \tag{9}$$

$$\boldsymbol{\nabla} \times \boldsymbol{E} = -\frac{\partial \boldsymbol{B}}{\partial t} \tag{10}$$

$$\boldsymbol{\nabla} \times \boldsymbol{H} = \boldsymbol{J} + \frac{\partial \boldsymbol{D}}{\partial t} \tag{11}$$

The remarkable consistency and completeness of those equations motivated Einstein to formulate his theory of special relativity, upon the requirement that Maxwell's laws should hold true in all inertial reference frames, ultimately unveiling revolutionary concepts such as time dilation, length contraction and the fact that the speed of light is a universal constant. As a consequence of special relativity, electricity and magnetism are fundamentally interlinked, so that even if a phenomenon appears purely electric or magnetic to one observer, it should be a mix of both in another reference frame.

2.4.2 Magnetic energy

We may define the magnetic energy as the work done by the a spatially distributed electric currents against the counteracting electromotive forces in order to build up a certain magnetic induction ($\boldsymbol{B}$) field spatial configuration. This energy is quantifiable and recoverable, so that it can be regarded as stored in the magnetic fields.

The energy density in a generalized distribution of electric fields and currents is given by,

$$U_M = \int \boldsymbol{\mathcal{E}} \cdot \boldsymbol{J} dt$$

Where $\boldsymbol{\mathcal{E}}$ stands for the electric field, and $\boldsymbol{J}$ is the current density. Application of Ampère's law (11) gives for the integrand,

$$\boldsymbol{\mathcal{E}} \cdot \boldsymbol{J} = \boldsymbol{\mathcal{E}} \cdot (\boldsymbol{\nabla} \times \boldsymbol{H}) - \boldsymbol{\mathcal{E}} \cdot \frac{\partial \mathbf{D}}{\partial \mathrm{t}}$$

Now, let's apply the following vectorial identity,

$$\boldsymbol{u} \cdot (\boldsymbol{\nabla} \times \boldsymbol{v}) = \boldsymbol{v} \cdot (\boldsymbol{\nabla} \times \boldsymbol{u}) - \boldsymbol{\nabla} \cdot (\boldsymbol{u} \times \boldsymbol{v})$$

Resulting in,

$$\boldsymbol{\mathcal{E}} \cdot \boldsymbol{J} = [\boldsymbol{H} \cdot (\boldsymbol{\nabla} \times \boldsymbol{\mathcal{E}}) - \boldsymbol{\nabla} \cdot (\boldsymbol{\mathcal{E}} \times \boldsymbol{H})] - \boldsymbol{\mathcal{E}} \cdot \frac{\partial \mathbf{D}}{\partial \mathrm{t}}$$

Then, accounting Faraday's law (10),

$$\boldsymbol{\mathcal{E}} \cdot \boldsymbol{J} = -\boldsymbol{H} \cdot \frac{\partial \boldsymbol{B}}{\partial t} - \boldsymbol{\mathcal{E}} \cdot \frac{\partial \mathbf{D}}{\partial \mathrm{t}} + \boldsymbol{\nabla} \cdot (\boldsymbol{\mathcal{E}} \times \boldsymbol{H})$$

Now, integrating over volume and applying the theorem of the divergence ($\oint (\boldsymbol{\nabla} \cdot \boldsymbol{u}) dV = \oint \boldsymbol{u} \cdot \boldsymbol{dS}$) to the last term,

$$\frac{dU}{dt} = \oint (\boldsymbol{\mathcal{E}} \cdot \boldsymbol{J}) dV = \oint - \left(\boldsymbol{H} \cdot \frac{\partial \boldsymbol{B}}{\partial t} \right) dV + \oint - \left(\boldsymbol{\mathcal{E}} \cdot \frac{\partial \boldsymbol{D}}{\partial t} \right) dV + \oint (\boldsymbol{\mathcal{E}} \times \boldsymbol{H}) \cdot \boldsymbol{dA}$$

This expression shows that, for a closed surface, the magnetic energy carries one contribution from the volume and from the boundary. The latter is associated with electromagnetic radiation and goes to zero if we take the integration over a sufficiently large volume since $\lim_{r \to \infty} |\boldsymbol{\mathcal{E}}||\boldsymbol{H}||\boldsymbol{A}| = 0$ (posed that $\mathcal{E} \propto r^{-2}$, $H \propto r^{-1}$ e $A \propto r^{2}$).

Moreover, the first two term correspond to the energies stored in the magnetic field (left) and in the electric field (right). The magnetic portion then is given by,

$$u_M = -\int \boldsymbol{H} \cdot \frac{\partial \boldsymbol{B}}{\partial t} dt = -\int \boldsymbol{H} \cdot d\boldsymbol{B} = -\mu_0 \int \boldsymbol{H} \cdot d\boldsymbol{M} - \mu_0 \int \boldsymbol{H} \cdot d\boldsymbol{H}$$

Where we have substituted the expression for the magnetic induction (5),

$$u_M = -\mu_0 \int \boldsymbol{H} \cdot d\boldsymbol{M} - \mu_0 \frac{|\boldsymbol{H}|^2}{2} \tag{12}$$

The first term represents the work necessary to magnetize the material, and the second term is the energy stored in the magnetic field. The former can be rewritten so to consider the magnetic moments:

$$u_M = -\mu_0 \int \boldsymbol{H} \cdot d\boldsymbol{M} = -\frac{\mu_0}{V} \sum_i \int \boldsymbol{H} \cdot d\boldsymbol{\mu_i}$$

So that the contribution of each individual magnetic moment to the total energy is,

$$u_{H,i} = -\mu_0 \int \boldsymbol{H} \cdot d\boldsymbol{\mu_i} \tag{13}$$

It might strike as strange that magnetic fields store energy in spite of the fact that they do no work. This complication may be settled by realizing that the magnetic induction field is a state variable, that, as such, is gradually built up by electric currents, which in turn, do work. Moreover, magnetized objects also exhibit this correspondence, so that the magnetization field corresponds to a distribution of bound currents at the surface. The whole system then, is equivalent to a single ribbon of current flowing around the boundary. This bound surface current is the net macroscopic current flowing over the surface of the magnetized object from the combination of many tiny current loops of electrons moving around their orbits.

The expression for the torque comes straightforwardly from the energy. Consider the interaction between a magnetic dipole moment and a constant magnetic field applied along the z-axis,

$$u_H = -\mu_0(\boldsymbol{\mu} \cdot \boldsymbol{H}) = -\mu_0 |\boldsymbol{\mu}||\boldsymbol{H}| \cos\theta$$

Then the torque is,

$$\boldsymbol{\tau} = -\boldsymbol{\nabla}_{\varphi,\theta} u_H = -\left(\frac{\partial E_{mag}}{\partial \theta}\widehat{\boldsymbol{\theta}} + \frac{\partial E_{mag}}{\partial \varphi}\widehat{\boldsymbol{\varphi}}\right) = \mu_0 |\boldsymbol{\mu}||\boldsymbol{H}| \sin\theta \, \widehat{\boldsymbol{\theta}}$$

Or, more generally,

$$\boldsymbol{\tau} = \mu_0(\boldsymbol{\mu} \times \boldsymbol{H}) \tag{14}$$

The force, on the other hand is,

$$\boldsymbol{F} = -\boldsymbol{\nabla} u_H = \mu_0 H_z \left(\frac{\partial \mu_z}{\partial x}\hat{\boldsymbol{\imath}} + \frac{\partial \mu_z}{\partial y}\hat{\boldsymbol{\jmath}} + \frac{\partial \mu_z}{\partial z}\widehat{\boldsymbol{k}}\right) \tag{15}$$

2.4.3 The Landau-Lifshitz equation

Consider now the magnetic torque felt by the spin magnetic moment subject to a magnetic field. The magnetic moment produced by the spin angular momentum is given by,

$$\boldsymbol{\mu} = -g\mu_B \boldsymbol{S}$$

Substitution in the equation of torque gives,

$$\boldsymbol{\tau} = -\mu_0 g \mu_B (\boldsymbol{S} \times \boldsymbol{H})$$

From Newton's laws the torque is the time derivative of the angular momentum,

$$\boldsymbol{\tau} = \frac{d(\hbar \boldsymbol{S})}{dt}$$

Combination of both gives,

$$\frac{d\boldsymbol{S}}{dt} = -\frac{\mu_0 g \mu_B}{\hbar}(\boldsymbol{S} \times \boldsymbol{H})$$

Finally, by applying the average over volume as in equation (4), we can express this equation in terms of the magnetization:

$$\frac{d\boldsymbol{M}}{dt} = -\gamma(\boldsymbol{M} \times \boldsymbol{H}) \tag{16}$$

which is the Landau-Lifshitz equation, and $\gamma = g\mu_B/\hbar$ is known as the gyromagnetic ratio.

In applying a magnetic field along the z axis ($\boldsymbol{H_0} = H_0\hat{\boldsymbol{z}}$), equation (16) gives,

$$\frac{dM_x}{dt} = -\gamma H_0 M_y \qquad\qquad \frac{dM_y}{dt} = \gamma H_0 M_x$$

Taking the time derivative it becomes,

$$\frac{d^2M_x}{dt^2} = -\gamma H_0 \frac{dM_y}{dt} = -(\gamma H_0)^2 M_x$$

$$\frac{d^2M_y}{dt^2} = \gamma H_0 \frac{dM_x}{dt} = -(\gamma H_0)^2 M_y$$

This is a wave equation with solution,

$$M_x(t) = m_x e^{-i\omega_0 t} \tag{17}$$

$$M_y(t) = m_y e^{-i\omega_0 t} \tag{18}$$

Moreover, by noticing that

$$\frac{dM_y}{dt} = \gamma H_0 M_x \quad \rightarrow \quad (-im_y)\omega_0 e^{-i\omega_0 t} = (m_x)\omega_0 e^{-i\omega_0 t}$$

It is clear that m_y is delayed $90°$ from m_x (i.e.: $m_y = -im_x$). As in the phasor representation well-known to circuit analysis, m_x and m_y are complex numbers that carry information about the amplitude and phase of the corresponding quantity, in contrast to the sinusoidal multiplier ($e^{-i\omega_0 t}$) that brings about the oscillatory part. In practice, the tangible part of a phasor corresponds to its real portion ($Re[M_i(t_0)]$), which is the instantaneous value at a given time t_0. Equations (17) and (18) can be assembled in one by the definition of circularly polarized magnetization,

$$M^{-}(t) = m^{-}e^{-i\omega_0 t}$$
$$m^{-} \equiv m_x - im_y \tag{19}$$

Equation (19) then describes the natural response of a magnetized sample to a magnetic field: a precession regime of frequency $\omega_0 = \gamma H_0$. It further tells us that for magnetic fields in the order of a few kOe, the frequencies lie in the microwave frequency range, since $\gamma = 2\pi \times 2.8 = 17.5929\ \mathrm{GHz/kOe}$.

Figure 6 - Precession of spin about magnetic field.

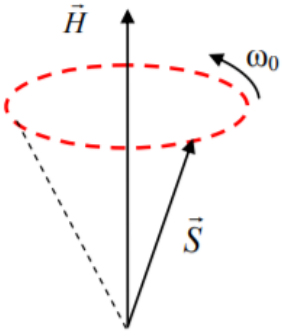

Source: the author.

2.4.4 Vector potential and magnetic dipole moment

The expression for the orbital magnetic moment can be obtained by a multipolar expansion of the magnetic vector potential as demonstrated in [11]. The formulation of the latter follows from the fact that magnetic field lines form a closed loop ($\nabla \cdot \boldsymbol{B} = 0$). Since the divergence of the curl of a given vector is null, one may write the relation,

$$\boldsymbol{B} \equiv \boldsymbol{\nabla} \times \boldsymbol{A}$$

Now, we shall demonstrate that the vector potential, as defined, *can* exist. Ampère's law (11) gives,

$$\boldsymbol{\nabla} \times \boldsymbol{B} = \boldsymbol{\nabla} \times (\boldsymbol{\nabla} \times \boldsymbol{A}) = \mu_0 \boldsymbol{J}$$
$$\boldsymbol{\nabla}^2 \boldsymbol{A} - \boldsymbol{\nabla}(\boldsymbol{\nabla} \cdot \boldsymbol{A}) = -\mu_0 \boldsymbol{J} \tag{20}$$

Where we have used the following vectorial identity,

$$\boldsymbol{\nabla} \times (\boldsymbol{\nabla} \times \boldsymbol{u}) = \boldsymbol{\nabla}(\boldsymbol{\nabla} \cdot \boldsymbol{u}) - \boldsymbol{\nabla}^2 \boldsymbol{u}$$

which can be straightforwardly obtained by applying the corresponding derivatives to the vector components and rearranging them.

This equation can be simplified by forcing the second lefthand term to zero by means of the Coulomb gauge transform. This gauge exploits the property that the curl is invariant upon addition of the gradient of a scalar function in order to construct a null divergence version of $\boldsymbol{A}$. Assume we have an arbitrary unaltered vector potential $\boldsymbol{A_0}$ whose divergence is not zero. We then construct the following:

$$\boldsymbol{A_{CG}} = \boldsymbol{A_0} + \boldsymbol{\nabla}\lambda$$

and force the divergence of $\boldsymbol{A_{CG}}$ to zero,

$$\boldsymbol{\nabla} \cdot \boldsymbol{A_{CG}} = \boldsymbol{\nabla} \cdot \boldsymbol{A_0} + \boldsymbol{\nabla}^2 \lambda = 0 \qquad \xrightarrow{\boldsymbol{\nabla} \cdot \boldsymbol{A_{CG}} = 0} \qquad \boldsymbol{\nabla}^2 \lambda = -\boldsymbol{\nabla} \cdot \boldsymbol{A_0}$$

This is a Poisson equation, whose solution is well known to electrostatics,

$$\lambda = \frac{1}{4\pi} \int \frac{dV' a}{r} = \frac{1}{4\pi} \int \frac{dV' \boldsymbol{\nabla} \cdot \boldsymbol{A_0}}{r}$$

This proves that the Coulomb gauge transform is realizable, so that equation (20) reduces to:

$$\boldsymbol{\nabla}^2 \boldsymbol{A} = -\mu_0 \boldsymbol{J} \tag{21}$$

Which is a set of independent Poisson's equation for each orthogonal component of the current density, so that,

$$\boldsymbol{A} = \frac{\mu_0}{4\pi} \sum_i \boldsymbol{\hat{x}_i} \int \frac{dV' J_i}{r_i} \tag{22}$$

Therefore, each component of the vector potential behaves in relation to its corresponding component of electric current like the electrostatic potential does in relation to the electric charge. The formulation of the vector potential further allows us to redefine the electric potential by substituting it into Faraday's law (10),

$$\boldsymbol{\nabla} \times \boldsymbol{E} = -\frac{\partial \boldsymbol{B}}{\partial t} = -\frac{\partial(\boldsymbol{\nabla} \times \boldsymbol{A})}{\partial t} \quad \rightarrow \quad \boldsymbol{\nabla} \times \left(\boldsymbol{E} + \frac{\partial \boldsymbol{A}}{\partial t}\right) = 0$$

So that,

$$\boldsymbol{E} + \frac{\partial \boldsymbol{A}}{\partial t} = -\boldsymbol{\nabla} V \tag{23}$$

Now we have the tools to define the magnetic dipole moment. A multipole expansion of $\boldsymbol{A}$ is obtained by expanding in a series of powers of $1/r$. The first order term is the monopole term, the second order term is the dipole term, the third order is the quadrupole term and so on:

$$\boldsymbol{A}(\boldsymbol{r}) = \frac{\mu_0 I}{4\pi}\left\{\frac{1}{r}\oint d\boldsymbol{l}' + \frac{1}{r^2}\oint r' \cos\theta'\, d\boldsymbol{l}' + O[(1/r)^3]\right\}$$

According to Maxwell's equation (9), there are not such things as magnetic monopoles, so that the dipole term is the dominant one. Thus, it can be written in the form,

$$\boldsymbol{A}_{dip}(\boldsymbol{r}) = \frac{\mu_0}{4\pi}\frac{\boldsymbol{\mu} \times \hat{\boldsymbol{r}}}{r^2} \tag{24}$$

Where $\boldsymbol{\mu}$ is the magnetic dipole moment,

$$\boldsymbol{\mu} \equiv I \oint d\boldsymbol{S} \tag{25}$$

Now, consider a collective motion of electrons revolving circularly around the atomic nucleus, the contribution of one electron to the total current I is given by,

$$I_e = \frac{I}{N_e} = \frac{\lambda}{N_e}\frac{dl}{dt} = -\left(\frac{e}{2\pi R}\right)v$$

Where R is the orbit radius, N_e is the total number of electrons, and $\lambda = -Ne/2\pi R$ is the linear charge density of the system. Then, the magnetic moment due to one electron reads,

$$\boldsymbol{\mu}_l = -\left(\frac{ev}{2\pi R}\right)(\pi R^2)\hat{\boldsymbol{l}} = -\left(\frac{evR}{2}\right)\hat{\boldsymbol{l}}$$

On the other hand, the orbital angular momentum is given by,

$$\boldsymbol{p}_l = m_0(\boldsymbol{r} \times \boldsymbol{v}) = m_0 v R \hat{\boldsymbol{l}}$$

So that,

$$\boldsymbol{\mu}_l = -\left(\frac{e}{2m_0}\right)\boldsymbol{p}_l \tag{26}$$

Is the orbital magnetic moment.

2.4.5 The spin-orbit interaction

Consider again the semiclassical case of an electron revolving circularly in its orbit about the atom's nucleus with tangential velocity $\boldsymbol{v}$ (**Figure 7.a**). If we take the electron's reference frame, this problem can be regarded as the nucleus revolving around the electron with tangential velocity $-\boldsymbol{v}$ (**Figure 7.b**).

Figure 7 – Circular orbital motion of an electron. (a) in the frame of reference from the nucleus. (b) from the frame of reference of the electron.

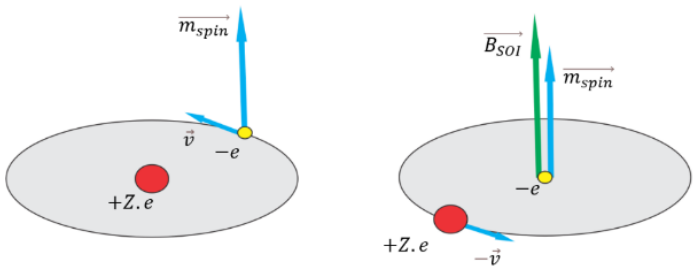

(a) (b)

Source: the author.

Because the nucleus has positive charge, its motion represents an electric current that, according to Biot-Savart's law, corresponds to a magnetic field at the electron's site given by:

$$\boldsymbol{H}_L = -\frac{q}{4\pi}\frac{(\boldsymbol{r} \times \boldsymbol{v})}{|\boldsymbol{r}|^3} = -\frac{q}{4\pi m_e}\frac{\boldsymbol{p_l}}{|\boldsymbol{r}|^3} = \left(\frac{\mu_B \varepsilon_0}{m_e}\right)\frac{1}{|\boldsymbol{r}|}\left(\frac{-q}{4\pi\varepsilon_0|\boldsymbol{r}|^2}\right)\boldsymbol{L}$$

Or,

$$\boldsymbol{H}_L = \left(\frac{\mu_B \varepsilon_0}{m_e}\right)\frac{1}{R}\left(\frac{\partial V}{\partial r}\right)_R \boldsymbol{L} \tag{27}$$

Where $\boldsymbol{p_l}$ is the orbital angular momentum of the electron. In turn, this effective field interacts with the electron's spin magnetic moment, thus producing a torque that tends to align the spin and the field. The energy and torque are given by,

$$E_{SL} = -\mu_0 \boldsymbol{\mu_s} \cdot \boldsymbol{H_{so}} = \left[\frac{ge^2\hbar^2}{4m^2c^2m_e}\right]\frac{1}{R}\left(\frac{\partial V}{\partial r}\right)_R \boldsymbol{S} \cdot \boldsymbol{L} \tag{28}$$

$$\boldsymbol{\tau}_{SL} = \mu_0 \boldsymbol{\mu_s} \times \boldsymbol{H_{so}} = -\left[\frac{ge^2\hbar^2}{4m^2c^2m_e}\right]\frac{1}{R}\left(\frac{\partial V}{\partial r}\right)_R (\boldsymbol{S} \times \boldsymbol{L}) \tag{29}$$

The spin-orbit torque (SOT) thereby woks as a relaxation mechanism, that brings about the inertia of the crystal lattice into a material's magnetic response.

2.5 The Stern-Gerlach experiment and the quantum nature of the spin

Before proceeding, I would like to provide an account of the quantum nature of the spin. Although originally designed to test the space quantization of atomic orbitals predicted by Bohr's atomic model, the Stern-Gerlach's experiment (1921) was the first to provide convincing evidence of the electron's spin. The principle was fairly simple: if atoms have magnetic moments that can point in any direction as classical physics would suggest, then the magnetic force produced by an inhomogeneous field would cause the beam of atoms to broaden in a continuous bundle of beams. On the other hand, if the magnetic moments of the atom are quantized – that is, pointing in opposite directions (say, *up* and *down*) along the field – then the beam of atoms would be split in two.

In the original version of the experiment, Stern and Gerlach vaporized silver in an oven and allowed some atoms to escape through a hole. They then sent the atoms through a pair of collimators, which created a beam that travelled between the two pole pieces of an electromagnet – assuming that Ag atoms are considered heavy enough to apply the classical concept of trajectory. In order to provide a magnetic field with the required level of inhomogeneity, one of the pieces had a groove cut into it, while the other had a sharp, knife-like edge, being held above the groove. After passing through

the magnet, the beam struck a detector plate where the presence of silver could be revealed by a chemical development process similar to that used in photography. The setup is depicted in **Figure 8** taken from [13].

Figure 8 – The Stern-Gerlach experimental setup.

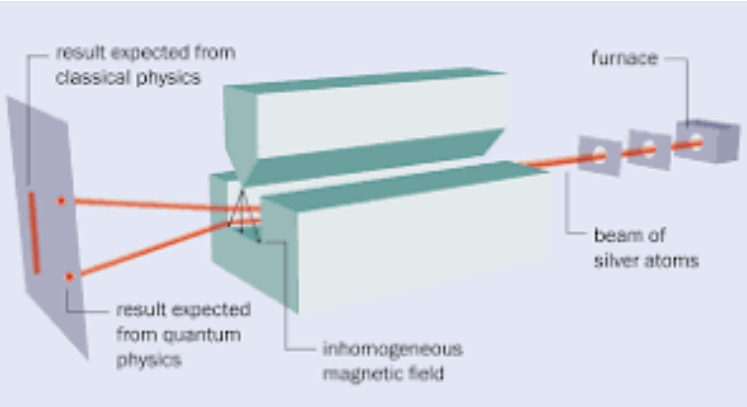

Source: Hamish (2024).

The experiment was fairly difficult to undertake. First, the apparatus had to be small (about $20\ cm$ long), and high-vacuum conditions were needed so that atoms could travel without scattering from air molecules. In fact, the apparatus often broke, making it difficult to achieve the long run time needed to accumulate enough silver on the detector plate to create a visible image. The following interpretation of the Stern-Gerlach experiment, and definition of spin ½ systems are based on the derivations from [27].

Silver atom comprises 47 electrons, from which 46 form a magnetically neutral electron cloud so that the angular momentum is solely due to the spin of the 47^{th} unpaired electron in the $5s$ subshell. If the field gradient is much stronger in a certain direction x_i, each atom will be subject to a force proportional to its spin magnetic moment,

$$\boldsymbol{F} = -\nabla\mathcal{H} = \mu_i \frac{\partial B_i}{\partial x_i}\hat{\boldsymbol{x}_\boldsymbol{\imath}}$$

This shall be called a x_i-oriented Stern-Gerlach apparatus, or $SG(\hat{\boldsymbol{x}_\boldsymbol{\imath}})$. Assuming the magnetic field gradient to be in the positive $\hat{\boldsymbol{x}_\boldsymbol{\imath}}$ direction, for $\mu_i > 0$ the atoms experience an upwards force, whereas for $\mu_i < 0$ there is a downwards force. From the perspective of classical mechanics, all values between $|\mu_i|$ and $-|\mu_i|$ should

be realized. As a matter of fact, the beams were split onto two quite well-defined loci, suggesting that the spin is quantized in the direction of the magnetic field with two possible values.

Further insights are obtained from the combination of three subsequent Stern-Gerlach apparatuses. The experiment goes as follows:

(1) The beam passes through $SG_1(\hat{\boldsymbol{z}})$, thereby being split in two loci: *upwards* and *downwards* along the z axis, meaning the existence of positive and negative z components of the magnetic moment. Namely:

Table 2 – Output beams from step (1).

Up-z	*Down-z*
$\mu_z > 0$	$\mu_z < 0$

Source: the author.

Moreover, it is important to note that feedbacking $SG_1(\hat{\boldsymbol{z}})$ with one of the split beams from step (1), the outcome would be a beam split in the same direction, so that there would be no change in the result.

(2) The *down-z* beam from (1) is blocked, whilst the remaining *up-z* beam ($\mu_z > 0$) is allowed to reach the next apparatus, $SG_2(\hat{\boldsymbol{x}})$. In turn, the beam is split in two loci: *right* and *left* along the x axis. Assuming the result in (1) to be preserved, we would have the outputs summarized in **Table 3**.

Table 3 – Expected output beams from step (2) assuming the outcome of (1) to be preserved.

Right-x	*Left-x*
$\mu_x > 0$	$\mu_x < 0$
$\mu_z > 0$	$\mu_z > 0$

Source: the author.

(3) The (*right-x*, *up-z*) beam from (2) is allowed to reach $SG_3(\hat{\boldsymbol{z}})$ at the end of the circuit. At this point, one might expect that, since the *down-z* beam ($\mu_z < 0$) was blocked in step (2), the output would be *up-z* polarized resulting in an upwards deflection. This expectation is, however, frustrated, as the result gives again two

loci, *upwards* and *downwards* along the z axis; as if there never was a selective blocking of the *down-z* beam at the first step.

Alternatively, if in step (2), after blocking the *down-z* beam, we had replaced $SG_2(\hat{\boldsymbol{x}})$ for an z oriented apparatus, the outcome would be an upwards deflected beam, consistent with $\mu_z > 0$ from step (1). Those results suggest that the intermediate $SG_2(\hat{\boldsymbol{x}})$ apparatus somehow erases the polarization from the up-z beam coming from the $SG_1(\boldsymbol{z})$, thus resetting the system.

The nuance in the SG experiment is somewhat similar to the interaction of polarized light with polarizers. Consider a beam of light polarized in the xy plane propagating in the z direction toward a detector. If a x-polarizer $P_1(x)$ is placed in the path, the y component of light will be blocked and only the x component will reach the detector,

$$\boldsymbol{A}_I = A_{I,x}\hat{\boldsymbol{x}} + A_{I,y}\hat{\boldsymbol{y}} \qquad \xrightarrow{P_1(\hat{\boldsymbol{x}})} \qquad \boldsymbol{A}_{II} = A_{I,x}\hat{\boldsymbol{x}}$$

It follows that a subsequent y polarizor $P_3(y)$ would result in no light reaching the detector because both components have been blocked. This picture changes if a new polarizer, say $P_2(x')$, polarized in the direction x', obtained by tilting the x axis by an $45°$ degree angle counterclockwise about the z axis, is placed in between $P_1(x)$ and $P_3(y)$. The projections of the x and y components on $x'$and y' are given by,

$$A_{x'} = A_x\cos(\theta) + A_y\sin(\theta) \qquad\qquad A_{y'} = -A_x\sin(\theta) + A_y\cos(\theta)$$

And the inverse operations are,

$$A_x = A_{x'}\cos(\theta) - A_{y'}\sin(\theta), \qquad A_y = A_{x'}\sin(\theta) + A_{y'}\cos(\theta)$$

So that we get,

$$\boldsymbol{A}_{II} = A_{I,x}\hat{\boldsymbol{x}} = \tfrac{A_{I,x}}{\sqrt{2}}\hat{\boldsymbol{x}}' - \tfrac{A_{I,x}}{\sqrt{2}}\hat{\boldsymbol{y}}' \qquad \xrightarrow{P_2(\hat{\boldsymbol{x}}')} \qquad \boldsymbol{A}_{III} = \frac{A_{I,x}}{\sqrt{2}}\hat{\boldsymbol{x}}' = \frac{A_{I,x}}{2}\hat{\boldsymbol{x}} + \frac{A_{I,x}}{2}\hat{\boldsymbol{y}}$$

The remark here is that the y component has been recovered after passing through $P_2(\hat{\boldsymbol{x}}')$, such that the light reaching the detector after the three polarizers is:

$$\boldsymbol{A}_{III} = \frac{A_{I,x}}{2}\hat{y} \neq 0$$

The mathematical similarity of this setting with the Stern-Gerlach experiment invites an useful insight: the x components of the spin (S_x) can be represented in a basis of *up* ($\mu_z > 0$) and *down* ($\mu_z < 0$) z-components, in the same way that the x' polarized light can be represented in a basis of x and y polarized light. Moreover, the addition of a SG apparatus in another coordinate axis mixes the state of the system, thus recovering blocked components from the former axis.

In order to obtain analytical expressions for the results observed, it is convenient to invoke the formalism of quantum mechanics. As previously discussed, from the first $SG_1(\hat{\boldsymbol{z}})$ apparatus we get two output beams, one deflected upwards and another deflected downwards, or, in the famous terms, the spin states *up* and *down*, let's call them $|S_z, -\rangle$ and $|S_z, +\rangle$. Furthermore, upon passing one of the beams through $SG_2(\hat{\boldsymbol{x}})$,

$$|\langle S_x, \pm|S_z, \pm\rangle|^2 = p(\pm) = \frac{1}{2}$$

Where p is the probability of a spin going from the state indicated in the ket to the state in the bra. This enables us to construct,

$$|S_x, \pm\rangle = \frac{1}{\sqrt{2}}\left(|S_z, +\rangle \pm e^{i\delta_x}|S_z, -\rangle\right)$$

For generality's sake, an arbitrary phase factor was introduced since it does not interfere in the probability. Note also, that $\langle S_x, +|S_x, -\rangle = 0$, so that orthonormality is preserved. For symmetry reasons, and the invariance of physical phenomena to the coordinate axis, the same should happen to the y axis,

$$|S_y, \pm\rangle = \frac{1}{\sqrt{2}}\left[|S_z, +\rangle \pm e^{i\delta_y}|S_z, -\rangle\right]$$

And an upstream $SG(\hat{\boldsymbol{y}})$ apparatus followed by an $SG(\hat{\boldsymbol{x}})$ gives,

$$\left|\langle S_x,\pm|S_y,\pm\rangle\right|^2 = p = \frac{1}{2}$$

$$\left|\frac{\left[\langle S_z,+|S_z,+\rangle + e^{i\delta_y}\langle S_z,+|S_z,-\rangle + e^{-i\delta_x}\langle S_z,-|S_z,+\rangle + e^{i(\delta_y-\delta_x)}\langle S_z,-|S_z,-\rangle\right]}{2}\right|^2 = \frac{1}{2}$$

Resulting in,

$$\left|1 + e^{i(\delta_y-\delta_x)}\right| = \sqrt{2} \qquad \longrightarrow \qquad \delta_y - \delta_x = \frac{\pi}{2}$$

By conveniently choosing $\delta_x = 0$, we get,

$$|S_x,\pm\rangle = \frac{1}{\sqrt{2}}|+\rangle \pm \frac{1}{\sqrt{2}}|-\rangle \tag{30}$$

$$|S_y,\pm\rangle = \frac{1}{\sqrt{2}}|+\rangle \pm \frac{i}{\sqrt{2}}|-\rangle \tag{31}$$

Where I have conveniently changed the notation to: $|S_z,\pm\rangle \rightarrow |\pm\rangle$.

Furthermore, in spin ½ systems it is useful to have operators that return the spin angular momentum of a given state, namely,

$$\tilde{S}_z|\pm\rangle = \pm\tfrac{\hbar}{2}|\pm\rangle \qquad \tilde{S}_x|S_x,\pm\rangle = \pm\tfrac{\hbar}{2}|S_x,\pm\rangle \qquad \tilde{S}_y|S_y,\pm\rangle = \pm\tfrac{\hbar}{2}|S_y,\pm\rangle$$

These properties are fulfilled by the following constructions:

$$\tilde{S}_z = \frac{\hbar}{2}(|+\rangle\langle+| - |-\rangle\langle-|) \tag{32}$$

Likewise,

$$\tilde{S}_y = \frac{\hbar}{2}\left(|S_y;+\rangle\langle S_y;+| - |S_y;-\rangle\langle S_y;-|\right)$$

$$= \frac{\hbar}{4}\left((1-1)|+\rangle\langle+| + (i^2-i^2)|-\rangle\langle-| + (-i-i)|+\rangle\langle-| + (i+i)|-\rangle\langle+|\right)$$

$$\tilde{S}_y = \frac{i\hbar}{2}(-|+\rangle\langle -| + |-\rangle\langle +|) \tag{33}$$

And, for S_x,

$$\tilde{S}_x = \frac{\hbar}{2}(|+\rangle\langle -| + |-\rangle\langle +|) \tag{34}$$

These operators, in turn, exhibit the following commutation relations,

$$\left[\tilde{S}_x, \tilde{S}_y\right] = \tilde{S}_x\tilde{S}_y - \tilde{S}_y\tilde{S}_x = \frac{i\hbar^2}{4}[|+\rangle\langle +| - |-\rangle\langle -| - (-|+\rangle\langle +| + |-\rangle\langle -|)] = i\hbar\tilde{S}_z$$

$$\left[\tilde{S}_z, \tilde{S}_x\right] = \frac{-\hbar^2}{4}[-|+\rangle\langle -| + |-\rangle\langle +| - (-|+\rangle\langle -| + |-\rangle\langle +|)] = i\hbar\tilde{S}_y$$

Or, in general,

$$\left[\tilde{S}_i, \tilde{S}_j\right] = i\hbar\varepsilon_{ijk}\tilde{S}_k \tag{35}$$

Which is the simplest realization of the angular momentum commutation relations, whose importance can hardly be overstated. Other two important operators are,

$$\tilde{\boldsymbol{S}}^2 = \tilde{\boldsymbol{S}} \cdot \tilde{\boldsymbol{S}} = \tilde{S}_x^2 + \tilde{S}_y^2 + \tilde{S}_z^2 = \frac{3\hbar^2}{4}$$

And,

$$\tilde{S}_\pm = \hbar|\pm\rangle\langle\mp| = \tilde{S}_x \pm i\tilde{S}_y$$

Which is the spin flip operator.

2.6 The exchange interaction

As discussed, ferromagnetism, ferrimagnetism and antiferromagnetism differ from other magnetic phases in that their spins exhibit long-range order, which led Weiss to postulate its molecular field theory. Later on, it was discovered that this effect

is actually due to the exchange interaction: a fundamental interaction that arises naturally from a quantum mechanical treatment of the electron-nucleus Coulomb interaction between different atoms.

Consider the simplest case of a system with two hydrogen atoms, which means that each atom consists of one nucleus and one electron. The Hamiltonian can be split in two terms, the self-energy term (e.g.: the kinetic energy of the electrons and each electron's interaction with its own nucleus), and the term corresponding to the cross interaction between the two atoms.

$$\mathcal{H} = \mathcal{H}_{self} + \mathcal{H}_{inter}$$

$$\mathcal{H}_{self} = -\left[\frac{\hbar^2}{2m_0}(\nabla_1^2 + \nabla_2^2) + \frac{e^2}{r_{a1}} + \frac{e^2}{r_{b2}}\right]$$

$$\mathcal{H}_{inter} = \left[\frac{e^2}{r_{ab}} + \frac{e^2}{r_{12}} - \frac{e^2}{r_{a2}} - \frac{e^2}{r_{b1}}\right]$$

Where the numbers refer to the nuclei, and the letters to the electrons. Provided that $\varphi_a(1)$, $\varphi_a(2)$, $\varphi_b(1)$, $\varphi_b(2)$ are the solutions to each of the electron-nucleus Schrödinger equations, as in,

$$\left[-\frac{\hbar^2}{2m_0}\nabla^2{}_1 - \frac{e^2}{r_{a1}}\right]\varphi_a(1) = E_a\varphi_a(1)$$

In order to account for indistinguishability of electrons, the total wave function must be a linear combination of all possible permutations of the individual solutions. Then, the spatial wave function of the system can be written as,

$$\varphi_{\substack{sym \\ antisym}}(1,2) = \frac{1}{\sqrt{2}}[\varphi_a(1)\varphi_b(2) \pm \varphi_a(2)\varphi_b(1)] \tag{36}$$

And the spin wavefunction,

$$\chi_{\substack{sym \\ antisym}}(1,2) = \frac{1}{\sqrt{2}}[\alpha(1)\beta(2) \pm \alpha(2)\beta(1)] \tag{37}$$

α and β are the single electron up and down spin wavefunctions respectively, such that when a magnetic field H_i is applied, it gives: $\alpha = \frac{\hbar}{2}\hat{\boldsymbol{\imath}}$ $\beta = -\frac{\hbar}{2}\hat{\boldsymbol{\imath}}$.

Moreover, the Pauli exclusion principle states that two fermions cannot occupy the same spin-orbital state. The asymmetric wavefunction is the only to fulfill this constraint because it vanishes for the case of two or more particles occupying the same quantum state; whereas the symmetric wavefunction is non-zero, violating the principle. For instance, consider the effect of taking $|\varphi_a(1)\rangle = |\varphi_b(1)\rangle$ and $|\varphi_a(2)\rangle = |\varphi_b(2)\rangle$ in the spatial wavefunction (36).

Figure 9 – Overlap of spin and spatial wavefunctions for neighboring ions. The directions of spins depend on the spatial charge distribution of the electrons of neighboring ions.

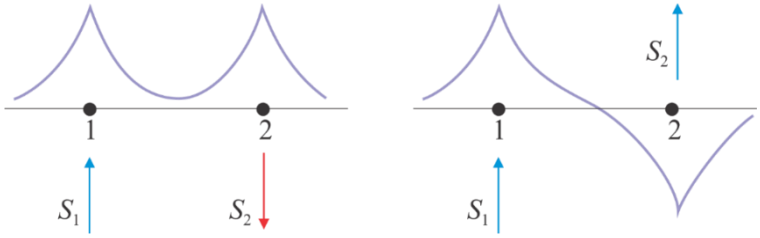

Source: Rezende (2022).

It follows that the total wave function with orbital and spin components has to be asymmetric. Thus, if the two spins are parallel, the orbital wave function is antisymmetric in space, whereas if the two spins are antiparallel, the orbital wave function is symmetric. So that,

$$\psi_I = A_I \varphi_{asym} \chi_{sym} \qquad \psi_{II} = A_{II} \varphi_{sym} \chi_{asym}$$

Then, the crossed interaction energy is given by,

$$U_{I/_{II}} = \int d\tau \left[\psi^*_{I/_{II}} \mathcal{H}_{inter} \psi_{I/_{II}} \right]$$

$$U_{I/_{II}} = A^2_{I/_{II}} 2(K_{12} \mp J_{12}) \tag{38}$$

Where,

$$J_{12} = \int d\tau[\varphi_a^*(1)\varphi_b^*(2)\mathcal{H}_{inter}\varphi_a(2)\varphi_b(1)] \tag{39}$$

$$K_{12} = \int d\tau[\varphi_a^*(1)\varphi_b^*(2)\mathcal{H}_{inter}\varphi_a(1)\varphi_b(2)] \tag{40}$$

K_{12} is the Coulomb integral and J_{12} is called the exchange integral because it only differs from K_{12} in the exchanged arrangement of the terms in the end of the integrand. Categorically, this term appears due to the cross electron-nucleus interaction from different atoms. Since the orbital wave function represents the charge distribution, the two states have different electrostatic Coulomb energies.

Moreover, since the demonstration of Equation (38) assumes the spins to be quantized in a given direction. Consider, for instance, that the i-th spin is quantized in the z-axis, while its neighbor, say the j-th spin, is partially tilted so to have a component on the x-axis. Because state $|S_x, +\rangle$ is a superposition of $|S_z, +\rangle$ and $|S_z, -\rangle$, its contribution to energy consists of an asymmetric term and a symmetric term, cancelling each other out. Therefore, only the component of $\boldsymbol{S}_j$ parallel to $\boldsymbol{S}_i$ account for the exchange energy, resulting in,

$$E_{exch,i,j} = -2J_{ij}\boldsymbol{S}_i \cdot \boldsymbol{S}_j \tag{41}$$

Where the inner product accounts only the parallel or antiparallel components of the spins. Furthermore, each spin S_i adds up to the exchange energy,

$$E_{exch,i} = -J\boldsymbol{S}_i \cdot \sum_j \boldsymbol{S}_j \tag{42}$$

Where each spin site is counted twice in the summation. If $J > 0$, the energy is minimum when the two spins are parallel to each other, thus leading to ferromagnetic ordering. On the other hand, if $J < 0$, the antiparallel alignment is favored, thus leading to antiferromagnetic ordering.

2.6.1 Spin waves

The exchange interaction leads to the formulation of non-localized, collective spin deviations from the magnetically ordered states called spin waves. Those are quantized by the name of magnons, which are bosons corresponding to low lying excitations of spin system that can be generated, for instance, by microwaves or thermal fluctuations. Rewriting equation (42) in terms of an effective field:

$$E_{exch,i} = -2J\boldsymbol{S_i} \cdot \sum_{j \neq i} \boldsymbol{S_j} = \boldsymbol{\mu_i} \cdot \left[\frac{2J}{g\mu_B} \sum_{j \neq i} \boldsymbol{S_j} \right] = -\boldsymbol{\mu_i} \cdot \boldsymbol{B_{exch,i}}$$

so that,

$$\boldsymbol{H_{exch,i}} = -\frac{2J}{g\mu_B\mu_0} \sum_{j \neq i} \boldsymbol{S_j} \tag{43}$$

Considering next neighbor contributions only, for a thin film with an elementary excitation propagating in the x axis it writes,

$$\boldsymbol{H_{exch,i}} = -\frac{2J}{g\mu_B\mu_0} (\boldsymbol{S_{i-1}} + \boldsymbol{S_{i+1}})$$

Assuming an external field in the $-z$ direction, the total field is,

$$\boldsymbol{H_{total,i}} = \boldsymbol{H_0} + \boldsymbol{H_{exch,i}}$$

Substituting this into the Landau-Lifshitz equation for the spins,

$$\frac{d\boldsymbol{S_i}}{dt} = -\gamma\mu_0 \boldsymbol{S_i} \times (\boldsymbol{H_0} + \boldsymbol{H_{exch,i}})$$

For the x component we get

$$\frac{dS_i^x}{dt} = -\gamma\mu_0 \left[S_i^y (H_0^z + H_{exch}^z) - S_i^z \left(H_{exch}^y \right) \right]$$

$$= -\gamma\mu_0 \left\{ S_i^y \left[-H_0 - \frac{2J}{g\mu_B\mu_0} (S_{i-1}^z + S_{i+1}^z) \right] - S_i^z \left[-\frac{2J}{g\mu_B\mu_0} \left(S_{i-1}^y + S_{i+1}^y \right) \right] \right\}$$

Since the sample is polarized in the z direction, we can assume $S_i^x, S_i^y \ll S_i^z \approx S$,

$$\frac{dS_i^x}{dt} = \gamma\mu_0 H_0 S_i^y + \frac{2JS}{\hbar} \left(2S_i^y - S_{i-1}^y - S_{i+1}^y \right) \tag{44}$$

Likewise, for the y component,

$$\frac{dS_i^y}{dt} = -\gamma\mu_0 H_0 S_i^x - \frac{2JS}{\hbar} (2S_i^x - S_{i-1}^x - S_{i+1}^x) \tag{45}$$

This equation tells us that the motion of the spin in any site is coupled to the motion of the neighboring spins, so that their solutions must be collective excitations. Assuming a travelling wave solution of the form,

$$S_i^x = A_x e^{i(kx_i - \omega t)} \qquad\qquad S_i^y = A_y e^{i(kx_i - \omega t)} \tag{46}$$

Substitution of (46) in equations (44) and (45) gives for the x component,

$$-i\omega A_x e^{i(kx_i - \omega t)} = A_y \left[\gamma\mu_0 H_0 + \frac{2JS}{\hbar} \left(2 - e^{-ika} - e^{ika} \right) \right] e^{i(kx_i - \omega t)}$$

Or, rearranging the terms,

$$(i\omega) A_x + \left[\gamma\mu_0 H_0 + \frac{4JS}{\hbar} (1 - \cos ka) \right] A_y = 0$$

And from the y component,

$$-\left[\gamma\mu_0 H_0 + \frac{4JS}{\hbar} (1 - \cos ka) \right] A_x + (i\omega) A_y = 0$$

The dispersion relation for this equation system is,

$$\omega_k = \gamma\mu_0 H_0 + \frac{4JS}{\hbar} (1 - \cos ka) \tag{47}$$

Substitution of ω_k in the above gives the relation between the amplitudes and phase of the spin components $A_x = iA_y = A_0$. **Figure 10** depicts a spin wave in a linear chain of classical spins.

Figure 10 - Spin wave in a linear chain of classical spins propagating in the $+x$ direction. (a) Top view. (b) Side view.

(a) (b)

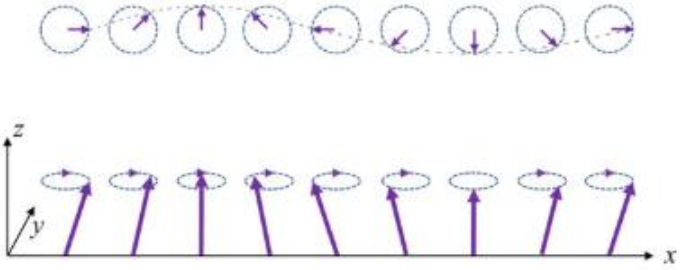

Source: Rezende (2020).

Moreover, for the more general case of a bulk sample, if the wavelength is much higher than the spacing between spins $\left({}^{2\pi}/_{k} \gg a\right)$, we can regard the spin distribution as continuous and expand it in a power series. In a particular direction it gives,

$$\boldsymbol{S}(\boldsymbol{r_i} + a\hat{\boldsymbol{x}}) = \boldsymbol{S}(\boldsymbol{r_i}) + \left.\frac{\partial \boldsymbol{S}}{\partial x}\right|_{\boldsymbol{r_i}} a + \frac{1}{2}\left.\frac{\partial^2 \boldsymbol{S}}{\partial x^2}\right|_{\boldsymbol{r_i}} a^2 + \mathcal{O}(a^3) \tag{48}$$

The same goes for the y and z axes. In equation (48), due to spatial symmetry, the odd powers cancel out at the $\pm a$ displacements from the equilibrium position; whereas the even powers add up ($(-a)^2 + a^2 = 2a^2$). Moreover, the 4th order or higher terms can be neglected, so that in three dimensions it reads,

$$\boldsymbol{H_{exch}} = -\frac{2J}{g\mu_B\mu_0}\sum_{\boldsymbol{\delta}} \boldsymbol{S}(\boldsymbol{r_i} + \boldsymbol{\delta})$$

$$= -\frac{2J}{g\mu_B\mu_0}\sum_{j=x,y,z} \hat{\boldsymbol{j}}\left[6S_j(\boldsymbol{r_i}) + a^2\left(\frac{\partial^2 S_j}{\partial x^2} + \frac{\partial^2 S_j}{\partial y^2} + \frac{\partial^2 S_j}{\partial z^2}\right)\Bigg|_{\boldsymbol{r_i}}\right]$$

$$= -\frac{2J}{g\mu_B\mu_0}[6\boldsymbol{S}(\boldsymbol{r_i}) + a^2\nabla^2\boldsymbol{S}(\boldsymbol{r_i})]$$

Which can be rewritten in the form,

$$\boldsymbol{H_{exch}} = w\boldsymbol{M} + \frac{D}{M}\nabla^2\boldsymbol{M}(\boldsymbol{r_i}) \tag{49}$$

Applying this to the Landau-Lifshitz equation, and omitting the first term since it will be in a cross product with itself, we get,

$$\frac{\partial \boldsymbol{M}}{\partial t} = -\gamma\mu_0\boldsymbol{M} \times (\boldsymbol{H_0} + \boldsymbol{H_{exch}}) = -\gamma\mu_0\boldsymbol{M} \times \left(\boldsymbol{H_0} + \frac{D}{M}\nabla^2\boldsymbol{M}(\boldsymbol{r_i})\right)$$

$$\frac{\partial M_x}{\partial t} = -\gamma\mu_0\left(M_y H_0 - M_z\frac{D}{M}\nabla^2 M_y\right) \qquad \frac{\partial M_y}{\partial t} = -\gamma\mu_0\left(M_z\frac{D}{M}\nabla^2 M_x - M_x H_0\right)$$

Where $M_z \approx M$. The circularly polarized magnetization (19) then reads,

$$i\frac{\partial M^-}{\partial t} = -\gamma\mu_0(D\nabla^2 M^- + H_0 M^-)$$

This is a wave equation in the form of harmonic travelling waves with solution,

$$M^-(\boldsymbol{r}, t) = m^- e^{i(\boldsymbol{k}\cdot\boldsymbol{r} - \omega_k t)} \tag{50}$$

And dispersion relation,

$$\omega_k = \gamma\mu_0(H_0 + Dk^2) \tag{51}$$

So that, in addition to the natural precession regime, the exchange interaction adds up a space dependency. It is worth noting, however, that in the ferromagnetic resonance all spins precess in phase, corresponding to $k = 0$, so that the magnetization response reduces to equation (19).

2.7 Structural mechanisms in thin films

This section addresses the mechanisms that govern magnetization inside a material. In this sense, magnetic anisotropy plays pivotal role, accounting for the

preferential orientation of magnetic moments in certain directions that produces the so-called easy axes and hard axes – that is, the symmetry axes that respectivelly attract and repel the magnetization. The magnetic anisotropy energy is thereby defined as the change in energy necessary to shift the magnetization from an easy axis to a hard axis. In ferromagnets, magnetic anisotropy originates either from their crystallographic structure, shape, or, in the case of ferromagnet/antiferromagnet systems, from the exchange interaction with the neighboring antiferromagnet.

Regarding spintronic applications, magnetic anisotropy is required for long-range magnetic order in thin films and nanostructures. Additionally, a variety of microscopic phenomena enable generation and control of spin currents to transport signals, exert torque or to interact with charge and spin waves.

2.7.1 Interaction with an external field

The interaction of the magnetized body with an applied field results in a potential energy in the same fashion of equation (12), also called the Zeeman energy,

$$E_Z = -\mu_0 \boldsymbol{H}_0 \cdot \boldsymbol{M}$$

Since characterization of magnetic samples usually involves the response at different angles, it is convenient to write the energy in spherical coordinates,

$$E_Z = -\mu_0 M H_0 (\cos\theta_M \cos\theta_H + \sin\theta_M \sin\theta_H \cos\varphi_M \cos\varphi_H + \sin\theta_M \sin\theta_H \sin\varphi_M \sin\varphi_H)$$

$$E_Z = -\mu_0 M H_0 [\cos\theta_M \cos\theta_H + \sin\theta_M \sin\theta_H \cos(\delta\varphi_H)]$$

Moreover, in this work we are mostly interested in thin films (2D) and their characteristics in the film plane, so that the polar angle is $\theta_H = \pi/2$, simplifying the energy expression,

$$E_Z = -\mu_0 M H_0 [\sin\theta_M \cos(\delta\varphi_H)] \quad (52)$$

Since the axis of the various sources of energy may not necessarily be in the origin of the coordinate axis, I hereby opt to write the displacements of the magnetization angle in relation to the angle of the i-th anisotropy term,

$$\delta\varphi_i = \varphi_M - \varphi_i \qquad \delta\theta_i = \theta_M - \theta_i$$

This shall be implied in the rest of the session.

2.7.2 Magnetocrystalline anisotropy

In the bulk of a sample, the torque generated by the spin-orbit interaction (Equation 29) depends on the crystalline electric potential which, in turn, is directly related to the lattice structure. As a result, a kind of magnetic anisotropy that reflects the lattice symmetry emerges, called magnetocrystalline anisotropy. With effect, magnetocrystalline anisotropy exhibit the lattice's periodicity, so that its contributions can be phenomenologically estimated by separating the different energy frequencies with respect to the angle of application of the magnetic field. In this work two forms of symmetry are most relevant: the uniaxial and cubic symmetries, which exhibit two and four cycles per revolution respectively.

Consider the energy as a power series of the director cosines in the spherical coordinate system [18] as in **Figure 11**,

$$E_{MC} = E_0 + \sum_i c_i a_i + \sum_{i,j} c_{ij} a_i a_j + \sum_{i,j,k} c_{ijk} a_i a_j a_k + \sum_{i,j,k,l} c_{ijkl} a_i a_j a_k a_l + \mathcal{O}(a^5)$$

Figure 11 - Spherical coordinate system and the directing cosines.

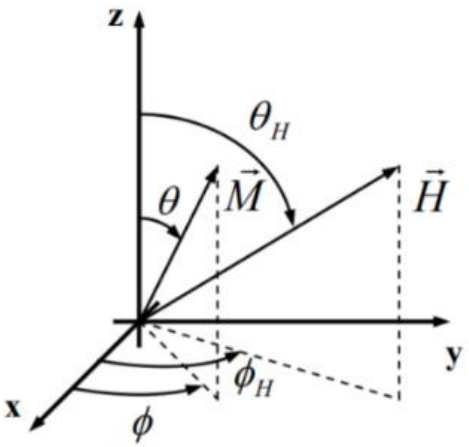

$$a_1 = \frac{\boldsymbol{M}\cdot\hat{\boldsymbol{x}}}{M} = \sin\delta\theta\cos\delta\varphi$$

$$a_2 = \frac{\boldsymbol{M}\cdot\hat{\boldsymbol{y}}}{M} = \sin\delta\theta\sin\delta\varphi$$

$$a_3 = \frac{\boldsymbol{M}\cdot\hat{\boldsymbol{z}}}{M} = \cos\delta\theta$$

Source: Bonfim (2009).

A few general considerations simplify this expression, namely: seventh and higher order terms are usually negligible; constant terms don't have physical significance; and the lattice looks the same with the reversal of magnetization so that the odd powers cancel out.

Uniaxial anisotropy is characterized by one single easy axis, thus having a twofold periodicity. The first order energy term is given by,

$$E_u = K_u \sin^2(\delta\theta_u)\sin^2(\delta\varphi_u) \tag{53}$$

It naturally emerges along the c-axis of materials that have hexagonal lattices, like cobalt. Moreover, uniaxial anisotropy may be induced relatively easily during the film growth by means of permanent magnets that produce a magnetic field nearby, or from mechanical strains (e.g.: due to the mismatching between the lattice parameters of subsequent materials, superficial rugosity, and oblique deposition); and after the film growth by thermal annealing.

On the other hand, materials with cubic lattice like YIG, Fe and Ni, exhibit **cubic anisotropy**. The number of cycles per revolution is fourfold and the energy is generally given by,

$$E_c = E_0 + K_{c0}({a_1}^2 + {a_2}^2 + {a_3}^2) + K_{c1}({a_1}^2{a_2}^2 + {a_1}^2{a_3}^2 + {a_2}^2{a_3}^2) + K_{c2}({a_1}^2{a_2}^2{a_3}^2) + K_{c3}({a_1}^4 + {a_2}^4 + {a_3}^4)$$

The terms E_0 and $K_{c0}({a_1}^2 + {a_2}^2 + {a_3}^2) = K_{c0}$ have no physical significance since they are constants; and, usually, $K_{c1}, K_{c2} \gg K_{c3}$. Therefore, first and second order terms, K_{c1} and K_{c2}, dominate the anisotropic behavior.

It has been shown that the relative values of the constants K_{c1} and K_{c2} determine the easy and hard axes orientations to be along one of the main the crystallographic axes $< 100 >$, $< 110 >$, or $< 111 >$, which are depicted in **Figure 12**. Namely, for $K_{c1} > 0$ and $K_{c2} \geq -9K_{c1}$ the easy axis will be parallel to the $< 100 >$ direction; on the other hand, for $K_{c1} < 0$ and $K_{c2} < -9K_{c1}$ the easy axis will be along $< 111 >$. For instance, at room temperature YIG has $K_{c1} = -5 \times 10^3\ \mathrm{erg/cm^3}$, while K_{c2} is negligible, resulting in easy axes along the $< 111 >$ direction, and hard axes long $< 100 >$. Moreover, the easy axes of Fe and Ni, the components of permalloy, are $< 100 >$ and $< 111 >$, respectively [23].

Figure 12 - Illustration of crystallographic symmetry planes.

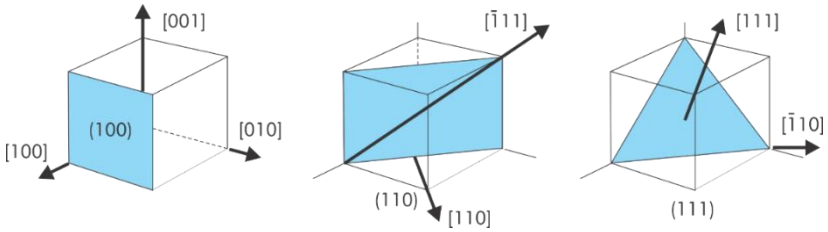

Source: Rezende (2022).

The first order cubic anisotropy energy E_{c1} is then,

$$E_{c1} = K_{c1}\{[\sin(\delta\theta_c)\cos(\delta\varphi_c)]^2[\sin(\delta\theta_c)\sin(\delta\varphi_c)]^2 + [\sin(\delta\theta_c)\cos(\delta\varphi_c)]^2[\cos(\delta\theta_c)]^2 + [\sin(\delta\theta_c)\sin(\delta\varphi_c)]^2[\cos(\delta\theta_c)]^2\}$$

$$= K_{c1}\{\sin^4(\delta\theta_c)\sin^2(\delta\varphi_c)\cos^2(\delta\varphi_c) + \sin^2(\delta\theta_c)\cos^2(\delta\theta_c)\,[\cos^2(\delta\varphi_c) + \sin^2(\delta\varphi_c)]\}$$

That gives,

$$E_{c1} = \frac{1}{4}K_{c1}[\sin^4(\delta\theta_c)\sin^2(2\delta\varphi_c) + \sin^2(2\delta\theta_c)] \tag{54}$$

And the second order cubic is,

$$E_{c2} = K_{c2}(\sin\theta\cos\varphi)^2(\sin\theta\sin\varphi)^2(\cos\theta)^2 = \frac{K_{c2}}{4}\sin^4\theta\cos^2\theta\sin^2 2\varphi$$

$$E_{c2} = \frac{K_{c2}}{64}(1 - \cos 2\theta - \cos^2 2\theta + \cos^3 2\theta)(1 - \cos 4\varphi) \quad (55)$$

Although often much smaller than the first order counterpart, the second order cubic anisotropy may be significant in some situations, such as the case of films grown in the {111} planes [25].

2.7.3 Shape anisotropy

The discontinuity of magnetization at the boundaries of a material generates a magnetic field in order to counteract the uncompensated magnetic dipoles. This field is called demagnetization field and follows from the inexistence of magnetic monopoles (Equation 9),

$$\nabla \cdot \boldsymbol{B} = \mu_0 \nabla \cdot (\boldsymbol{H} + \boldsymbol{M}) = 0$$

$$\nabla \cdot \boldsymbol{H}_D = -\nabla \cdot \boldsymbol{M}$$

Figure 13 - Demagnetization field appearance to balance uncompensated magnetic dipoles.

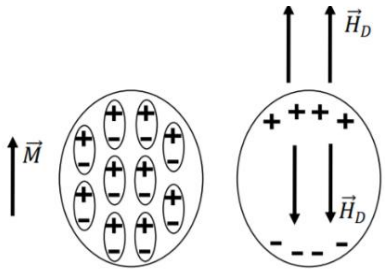

Source: Mendes (2009).

In order to the magnetic induction flux to remain constant, the demagnetization field is generated at the interface with the external medium (illustrated in **Figure 13**), thereby connecting the external magnetic influences with the internal energy. The demagnetization field inside the sample is given by,

$$\boldsymbol{H}_D = -\boldsymbol{D} \cdot \boldsymbol{M}$$

Where $\boldsymbol{D}$ is the demagnetization tensor that depends on the sample's geometry and angle of the magnetic field. For this reason, the demagnetization is considered a shape effect. This effect is behind the formation of magnetic domains, since it tends to conceal the magnetic induction inside the magnetic material (**Figure 14**).

Figure 14 - Illustration of the gradual formation of domains due to demagnetization fields from left to right.

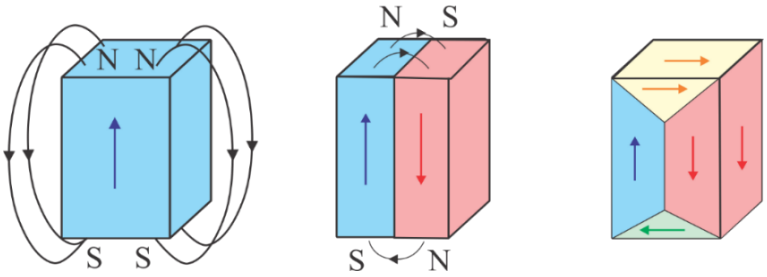

Source: Rezende (2022).

Consider a magnetic sample under the influence of an external magnetic field. The total field is

$$\boldsymbol{H} = (-D_x M_x)\hat{\boldsymbol{x}} + \big(-D_y M_y\big)\hat{\boldsymbol{y}} + (H_0 - D_z M_z)\hat{\boldsymbol{z}}$$

So that,

$$\frac{dM_x}{dt} = -\gamma M_y[H_0 + (D_x - D_z)M] \qquad \frac{dM_y}{dt} = \gamma M_x\big[H_0 + \big(D_y - D_z\big)M\big]$$

Resulting in a more realistic dispersion relation that accounts the external influences in the dipolar field,

$$\omega_0 = \mu_0\gamma[H_0 + (D_x - D_z)M]^{1/2}\big[H_0 + \big(D_y - D_z\big)M\big]^{1/2}$$

In a 2D film, the out-of-plane component of the demagnetization tensor is overwhelmingly larger than the in-plane component, so that,

$$E_D = -\mu_0 \int \boldsymbol{H}_d \cdot d\boldsymbol{M} = \mu_0 \int (D_{\hat{n}}\boldsymbol{M}_{\hat{n}}) \cdot d\boldsymbol{M} = \frac{1}{2}\mu_0 D_{\hat{n}} M_{\hat{n}}^2$$

$$E_D = \frac{1}{2}\mu_0(\hat{\boldsymbol{n}} \cdot \boldsymbol{M})^2$$

Where $D_{\hat{\boldsymbol{n}}} = 1$. In spherical coordinates,

$$E_D = \frac{1}{2}\mu_0 M^2 \cos^2\theta \tag{56}$$

This expression describes the tendency of magnetization to lie in the plane of a thin film. This is a convenient property for ferromagnetic resonance experiments performed in the plane of the sample because it compensates potential out-of-plane deviations of the magnetic field. In fact, it was shown that small out-of-plane deviations lower than 5° have little effect on the magnetization because the demagnetizing field in a 2D film effectively keeps the magnetization in the film plane [25].

Another mechanism that depends on the shape is caused by the break of translation symmetry of the crystalline electric fields at the surface of a material. This effect is more evident in thin films since the proportion of atoms in the interface per total of atoms is large. This originates another form of anisotropy known as **surface anisotropy**. The corresponding energy is described as an out-of-plane uniaxial anisotropy,

$$E_{surface} = -\frac{K_S}{M^2 t}(\hat{\boldsymbol{n}} \cdot \boldsymbol{M})^2$$

$$E_{surface} = -\frac{K_S}{t}\cos^2\theta \tag{57}$$

The relation between the atoms in the surface and the bulk may either favor an in-plane magnetization ($K_S < 0$), or an out-of-plane magnetization ($K_S > 0$).

Due to their equivalent dependence on the magnetization angle, the surface anisotropy energy (57) and the demagnetizing energy (56) may be combined in one resultant Hamiltonian,

$$E_S = E_D + E_{surface} = \frac{1}{2}\mu_0 M^2 \cos^2\theta - \frac{K_S}{t}\cos^2\theta = \frac{1}{2}\mu_0 M\left(M - \frac{2K_S}{\mu_0 M t}\right)\cos^2\theta$$

$$E_S = \frac{1}{2}\mu_0 M\left(M_{eff}\right)\cos^2\theta \tag{58}$$

$$M_{eff} = M - H_S \qquad\qquad H_S = \frac{2K_S}{\mu_0 M t}$$

2.7.4 Exchange bias

In favorable conditions, electrons from the interface of different media may become coupled by means of the exchange interaction. This effect, known as exchange bias (EB), can pin a FM's response, standing as a handy tool to control the magnetization of ferromagnets without the need for externally applied fields. Moreover, it has the advantages of being localized and partially tunable. The most characteristic signature of exchange bias is possibly the horizontal shift in the hysteresis loop and increased coercivity.

For our purposes, EB can be regarded as a unidirectional anisotropy (one cycle per revolution) occurring at the interface, with energy given by the Zeeman interaction with an effective field,

$$E_{EB} = -\mu_0 \boldsymbol{M} \cdot \boldsymbol{H}_{EB}$$

$$E_{EB} = -\mu_0 M H_{EB} [\cos\theta_M \cos\theta_{EB} + \sin\theta_M \sin\theta_{EB} \cos(\delta\varphi_{EB})] \quad (59)$$

FM/AFM bilayers are perhaps the most accessible prototypes for applications of exchange bias. The AFM spins – which are rather steady due to AFM internal compensation -- effectively pin the FM spins. Moreover, antiferromagnets have very low magnetic susceptibility, being magnetically neutral against stray fields, a feature that could prove to be vital in integrated devices with low dimensions that require shielding against crosstalk or external fields [14]. Such junctions have found commercial applications in HDD in tuning readback heads to their point of maximum sensitivity.

Furthermore, it has been shown that EB can persist through non-magnetic (NM) spacers with thicknesses up to a few angstroms in FM/NM/FM trilayers, by means of the RKKY interaction [21,33,34]. This interaction accounts for the indirect coupling of magnetic moments between nuclei and/or localized d- and f- shell electrons mediated by conduction electrons. The RKKY theory predicts an oscillatory behavior of the coupling between the two outermost FM layers as a function of the thickness of the spacer, together with an exponential decay in magnitude. This prediction had great importance in explaining the oscillation between FM and AFM coupling of FM layers found in the first experiments of GMR in FM/NM/FM films.

Another lively subject in spintronic addresses the generation and control of chiral spin textures such as skyrmions and chiral Néel domain walls [3,17,26,29]. Those structures are generated by the Dzyaloshinskii-Moriya interaction (DMI), which stands for the antisymmetric term of the exchange interaction that appears when considering SOC in the super-exchange interaction [7,19]. This term favors canted orientation of adjacent spins – in contrast to the symmetric term that favors collinear orientation – and requires spin-orbit interaction in an asymmetric crystal field, such as heterostructures lacking spatial inversion symmetry.

2.7.5 Spin Hall and Rashba-Edelstein Effects

In some materials, the coupling between spin and its orbit in a crystal lattice with structural asymmetry or with a scattering center (i.e.: impurities, or crystal defects) can result in the splitting of charge carriers according to their spin states, generating a transverse flow of spin polarization. In conventional terminology, this means that a charge current has converted into a spin current; and this effect is called the **spin Hall effect** (SHE). Remarkably, the inverse is also true. A spin current can be converted into a charge current by the same mechanism operating in reverse, effect known as the inverse spin Hall effect (ISHE), which is a valuable tool for probing internal physical properties of materials. The induced charge current density due to ISHE is,

$$\boldsymbol{J}_c = \frac{2e\theta_{SH}}{\hbar}(\boldsymbol{J}_s \times \hat{\boldsymbol{\sigma}})$$

where θ_{SH} is the spin Hall angle that gives the efficiency of the conversion, $\boldsymbol{J}_s$ stands for spin current density, and $\hat{\boldsymbol{\sigma}}$ is the spin polarization.

While SHE and ISHE are bulk effects, surfaces and interfaces are usually governed by the direct and inverse **Rashba-Edelstein effects** (REE and IREE) [5,8]. The broken inversion symmetry and different work functions at interfaces generate an outward electric field, which can be regarded as a magnetic field in the reference frame of the moving electron. For materials with strong interfacial spin-orbit coupling, this effective field may be strong enough to split electrons with opposite spins, causing the electrons to develop different energies and momenta, moving in opposite directions with spins locked perpendicular to the electrons' linear momenta. This coupling is called **spin-momentum locking** [12,15,37].

The surface charge current density produced by IREE is given by [30,31]:

$$\boldsymbol{J}_c = \frac{e\alpha_R}{\hbar}(\hat{\boldsymbol{n}} \times \boldsymbol{S})$$

Where α_R is the Rashba parameter, $\hat{\boldsymbol{n}}$ is the unit vector normal to the interface, and $\boldsymbol{S}$ represents the non-equilibrium spin density caused by spin injection.

In the field of quantum materials, **antimony** has drawn increasing attention for its unique properties while being an elemental material. Antimony is a diamagnetic semimetal that has been shown to host topological surface states, being a core component in many topological insulators. Moreover, Sb (111) has been confirmed to be protected against $180°$ backscattering, resulting in remarkable transmission through atomic steps such as defects and impurities [39,42]. This occurs because spin-momentum locking makes backscattering energetically unfavorable since a reversal of momentum must bring along a reversal of spin.

Generally, semimetals originate from the overlap of the valence and conduction bands, that become partially filled, thereby hosting electric currents under application of electric fields. They usually have small effective masses for holes and electrons due to the broadness of the energy bands, which, in turn, favors the aforementioned overlap. In addition, semimetals typically show high diamagnetic susceptibilities and high lattice dielectric constants. Although bulk Sb is a semimetal due to its negative indirect bandgap, its band order is inverted at the L point of the Brillouin zone. Antimony (electronic configuration $4d^{10}\ 5s^2\ 5p^3$) easily forms anions and covalent bonds; and have oxidation states $+3$ and $+5$. Moreover, its crystal structure is rhombohedral, and can be considered as a stacking of (111) bilayers.

3 EXPERIMENTAL TECHNIQUES AND FABRICATION PROCESSES

3.1 Ferromagnetic resonance spectroscopy

The ferromagnetic resonance (FMR) spectrometer is one of the most widely employed techniques for research in magnetism, for it enables comprehensive characterization of materials' magnetostatic and dynamic parameters, such as relaxation rate, Landé factor, magnetocrystalline anisotropies, exchange coupling, spin hall angle, etc.

Consider a magnetic sample that, in addition to the collective precession regime due to an applied magnetic field described in Section 2.4.3, is being stimulated by microwave fields in the precession plane (xy). Assuming a stationary regime, the total magnetic field and magnetization, including the microwave's fields contributions are then given by,

$$\boldsymbol{H} = \left[h_{\,x}(\boldsymbol{r})e^{-i\omega t}\right]\hat{\boldsymbol{x}} + \left[-ih_y(\boldsymbol{r})e^{-i\omega t}\right]\hat{\boldsymbol{y}} + (H_0)\hat{\boldsymbol{z}}$$

$$\boldsymbol{M} = \left[m_x(\boldsymbol{r})e^{-i\omega t}\right]\hat{\boldsymbol{x}} + \left[-im_y(\boldsymbol{r})e^{-i\omega t}\right]\hat{\boldsymbol{y}} + (M_0)\hat{\boldsymbol{z}}$$

Those, substituted in the Landau-Lifshitz equation gives,

$$\frac{d\left[m_x e^{-i\omega t}\right]}{dt} = i\gamma\left(m_y H_0 - h_y\, M_0\right) e^{-i\omega t} \quad \rightarrow \quad m_x(\boldsymbol{r}) = \frac{\gamma\left(h_y\, M_0 - m_y H_0\right)}{\omega} \qquad (60)$$

$$\frac{d\left[-im_y\, e^{-i\omega t}\right]}{dt} = -\gamma(h_x M_0 - m_x\, H_0)e^{-i\omega t} \quad \rightarrow \quad m_y(\boldsymbol{r}) = \frac{\gamma(h_x M_0 - m_x\, H_0)}{\omega} \qquad (61)$$

3.1.1 Building the susceptibility tensor

The magnetic susceptibility tensor (Equation 6) connects the magnetization and magnetic field at different axes. In the ferromagnetic resonance the components are related by Equations (60) and (61),

$$\begin{bmatrix} m_x \\ m_y \end{bmatrix} = \begin{bmatrix} \mathcal{X}_{xx} & \mathcal{X}_{xy} \\ \mathcal{X}_{yx} & \mathcal{X}_{yy} \end{bmatrix} \begin{bmatrix} h_x \\ h_y \end{bmatrix}$$

$$\mathcal{X}_{xx} = \mathcal{X}_{yy} = \frac{\omega_0 \omega_M}{{\omega_0}^2 - \omega^2} \qquad \mathcal{X}_{xy} = -\mathcal{X}_{yx} = \frac{\omega \omega_M}{{\omega_0}^2 - \omega^2}$$

$$\omega_0 \equiv \gamma H_0 \qquad \omega_M \equiv \gamma M_0$$

Where ω_0 is the frequency of system's natural response to the external magnetic field, ω_M is the response to the subsequent magnetization, and ω is the *rf* radiation's frequency.

A brief look at the susceptibilities reveals a clear unphysical situation: the susceptibilities go to infinity as $\omega \longrightarrow \omega_0$, meaning that the precession amplitude would reach a singularity in the resonance. This comes from the fact that I have not accounted for dissipation mechanisms, such as the energy dissipated by the crystal lattice through the spin-orbit interaction. This can be fixed by the phenomenological introduction of the relaxation rate (Γ), a damping factor with the form of exponential decay,

$$[m_x(r) - im_y(r)]e^{-i\omega_0 t} \xrightarrow{\times\left(e^{-i\Gamma t}\right)} \left[m_x(r) - im_y(r)\right]e^{-i(\omega_0 - i\Gamma)t}$$

So that the resonance frequency becomes $\omega_0 \rightarrow \omega_0 - i\Gamma$, and the susceptibilities become, for $\Gamma \ll \omega_0$,

$$\mathcal{X}_{xx} = \mathcal{X}_{yy} = \frac{\omega_0 \omega_M}{({\omega_0}^2 - \omega^2) - i2\omega_0\Gamma} \tag{62}$$

$$\mathcal{X}_{xy} = -\mathcal{X}_{yx} = \frac{\omega \omega_M}{({\omega_0}^2 - \omega^2) - i2\omega_0\Gamma} \tag{63}$$

It is worth noting that according to equations (62) and (63), $\mathcal{X}_{xx} = \mathcal{X}_{yy} = \mathcal{X}_{xy} = -\mathcal{X}_{yx}$ in the resonance.

3.1.2 Power absorbed in resonance

The probed quantity from a sample's response to the FMR experiment is the average power absorption. The measurement is done by a Schottky barrier diode that rectifies the reflected microwave, and a subsequent capacitor that stores DC voltage proportional to the wave amplitude, thereby quantifying the reflected/absorbed power. In terms of the susceptibility and microwave fields, the instantaneous power is,

$$P(t) = \frac{d(-\mu_0 \boldsymbol{M} \cdot \boldsymbol{H})}{dt} = -\frac{d\left[e^{-i2\omega t}\left(\mathcal{X}_{xx}{h_x}^2 + ih_x\mathcal{X}_{xy}h_y - ih_y\mathcal{X}_{yx}h_x + \mathcal{X}_{yy}{h_y}^2\right)\right]}{dt}$$

Noting that $\mathcal{X}_{xx} = \mathcal{X}_{yy}$, and that $\mathcal{X}_{xy} = -\mathcal{X}_{yx}$,

$$P(t) = i\mu_0 2\omega\left[\mathcal{X}_{xx}\left({h_x}^2 + {h_y}^2\right) + i2\mathcal{X}_{xy}h_x h_y\right]e^{-i2\omega t}$$

The active power is given by the real part of $P(t)$,

$$p(t) = Re\left[i\mu_0 2\omega\mathcal{X}_{xx}\left({h_x}^2 + {h_y}^2\right) - \mu_0 4\omega\mathcal{X}_{xy}h_x h_y\right]\cos\left(2\omega_{rf}t\right)$$

Or, in terms of the average power only,

$$\bar{P} = \mu_0\omega_{rf}\left({h_x}^2 + {h_y}^2\right)Im[\mathcal{X}_{xx}] - \mu_0 2\omega_{rf}h_x h_y Re\left[\mathcal{X}_{xy}\right] \qquad (64)$$

$$Im[\mathcal{X}_{xx}] = \frac{\omega_M\omega_0(2\omega_0\Gamma)}{(\omega_0^2 - \omega_{rf}^2)^2 + (2\omega_0\Gamma)^2} \qquad Re\left[\mathcal{X}_{xy}\right] = \frac{\omega_{rf}^2\omega_M\left(\omega_0^2 - \omega_{rf}^2\right)}{(\omega_0^2 - \omega_{rf}^2)^2 + (2\omega_0\Gamma)^2}$$

In general, the external field is modulated resulting in a modulated absorbed frequency that is ultimately sent to the lock-in amplifier, an active filter able to recover signals buried in noise. As shall be demonstrated in Section 3.1.4, the output of the lock-in amplifier is the derivative of the input with respect to the magnetic field,

$$v_{lock-in} = c_1\frac{\partial P}{\partial H_0} = c_1\gamma^{-1}\frac{\partial P}{\partial\omega_0}$$

Taking the derivatives and assuming $h_x = h_y$, this gives,

$$\frac{\partial P}{\partial\omega_0} = \left(4\mu_0 h_x^2\omega_{rf}\omega_0\omega_M\right)\frac{\left[\omega_{rf}^2\left(\omega_0^2 - \omega_{rf}^2\right) - \left(\omega_0^4 - \omega_{rf}^4\right)(2\Gamma) - \omega_{rf}^4(2\Gamma)^2\right]}{\left[(\omega_0^2 - \omega_{rf}^2)^2 + (2\omega_0\Gamma)^2\right]^2}$$

This equation can be further simplified assuming $\omega_0, \omega_{rf} \gg 2\Gamma$ so that the second order term on 2Γ can be disregarded, and having in mind that the susceptibility is large only in the vicinity of resonance, we consider $\omega_0 \approx \omega_{rf}$ so that $\left(\omega_0^2 - \omega_{rf}^2\right) \approx 2\omega_0\left(\omega_0 - \omega_{rf}\right)$.

$$\frac{\partial P}{\partial\omega_0} = \left(4\mu_0 h_x^2\omega_{rf}^3\omega_M\right)\frac{\left(\omega_0 - \omega_{rf}\right)\left(\Gamma - \frac{1}{4}\right)}{\left[(\omega_0 - \omega_{rf})^2 + \Gamma^2\right]^2}$$

Moreover, $\Gamma \gg 1$ so that the $\left(\Gamma - \frac{1}{4}\right) \approx \Gamma$, and the output signal from the lock-in can be written in terms of the effective fields as:

$$v_{lock-in} = c_1 \frac{(H_0 - H_R)\Delta H}{[\Delta H_0{}^2 + (H_0 - H_R)^2]^2} \tag{65}$$

Where all constants have been absorbed by c_1. Equation (65) is the derivative of a Lorentz curve with linewidth $\Delta H = \Gamma/\gamma$. This expression shall be used to numerically fit experimental curves in order to obtain the parameters ΔH and H_R. Lorentzian curves have the property that the arithmetic average of several Lorentzian curves results in a Lorentzian curve as well.

3.1.3 Instrumentation of FMR

Generally speaking, the FMR set up (**Figure 15**) consists of microwave bridge, resonant cavity, gaussmeter, electromagnet, lock-in amplifier, and Helmholtz modulating coil; furthermore, for feasibility's sake, automation and data acquisition are nearly indispensable. In this work the microwave frequency is kept fixed, and the magnetic field is swept through quasi-static values, although the reverse approach is also possible (keep the magnetic field fixed and vary the frequency).

Figure 15 - Ferromagnetic resonance experiment setup.

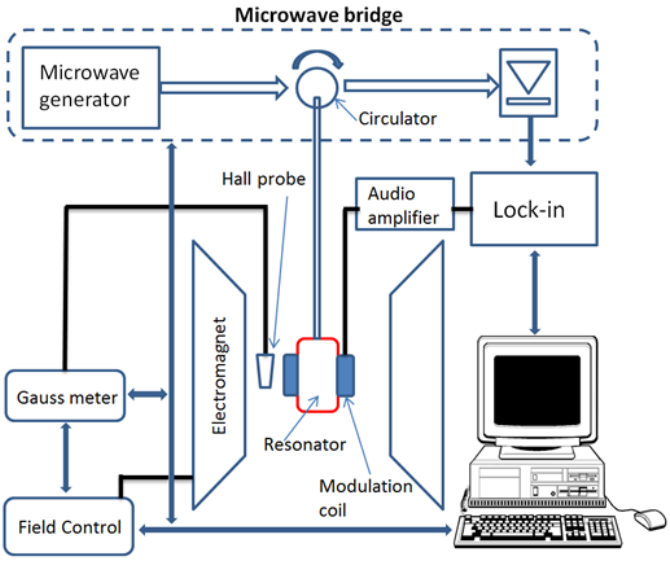

Source: Chi-Kuen (2013).

The microwave bridge is the assembly of a microwave generator, a detector and a transmission line. The transmission consists of waveguide; a circulator that redirects the reflected wave towards the detector at the end of the circuit; and a resonant cavity. The latter is responsible for optimizing the microwave transmission to the sample, this is a critical matter because it involves passage through different mediums.

Moreover, it is key that the sample is strongly affected by the magnetic field component of the *rf* radiation, and unaffected by the electric field. In this sense, the cavity's geometry and metallic walls are designed to sustain a constant spatial distribution of the electric and magnetic fields, thereby creating regions where the magnetic field is maximum, and the electric field is minimum (**Figure 16**.**a**). Naturally, such a setting depends greatly on the sample's shape, position, and angle so that resonant cavities are equipped with an iris, that permits a fine adjustment of the system's spatial configuration (**Figure 16**.**b**).

In fact, this whole system can be modelled as a RLC circuit as in **Figure 16**.**c**, in which the iris works as a LC reactive impedance compensation, and the empty space between the cavity and the *rf* bridge works as an ideal transformer [16]. According to transmission line theory, the energy transfer is optimized when the line and load impedances are matched ($\approx 50\ \Omega$), so that the iris has a pivotal role in optimizing the energy transfer.

Figure 16 - Resonant cavity for FMR measurements. (a) Distribution of electric and magnetic fields inside the cavity. (b) Schematic of the cavity. (c) Equivalent RLC circuit of the cavity scheme.

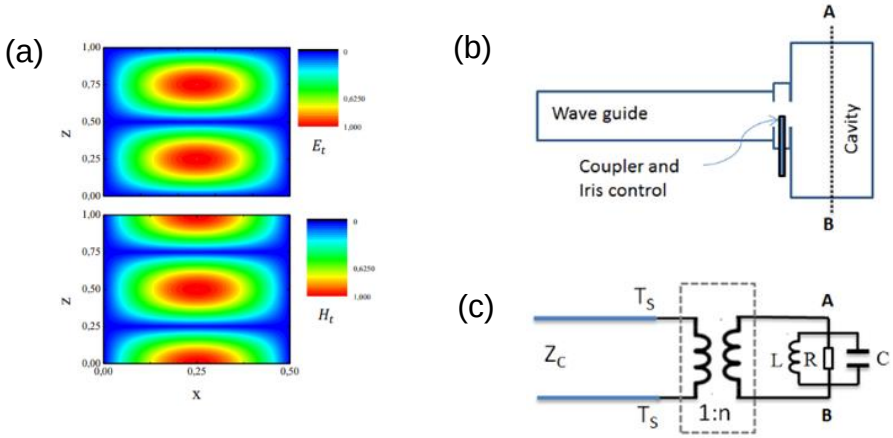

Sources: (a) Mendes (2009); (b) and (c) Chi-Kuen (2013].

3.1.4 Lock-in amplifier

The extraction of small signals buried in noise is a common problem in many areas such as nanotechnology, material science, optics and photonics, quantum technologies, scanning probe microscopy, and sensing. In this sense, the lock-in amplifier, an active filter with high noise suppression, is an essential part of many research laboratories, expanding greatly the reach of experimental setups. In the case of the ferromagnetic resonance spectrometer utilized in this work a Schottky diode measures the reflected intensity of rf waves casted onto a magnetized thin film, and the amount of energy absorbed by the sample is thereby inferred by subtracting the reflected intensity from the incident intensity. Reflectometers of this kind have a low signal-to-noise ratio (SNR), requiring a high-quality filter in order to raise SNR to an acceptable value (typically greater than 5).

The working principle of the lock-in amplifier, called demodulation or phase-sensitive detection, lies on mixing the measured signal with a reference frequency followed by low-pass filtering. Choosing the modulation frequency of the measured signal makes it possible to sort it away from dominant noise sources, because the latter is often spread over a much wider range of frequencies than the signal. Mathematically, it relies on the orthogonality of sinusoidal functions,

$$\int_0^{T_0} \sin(\omega_i t + \phi_i)\sin(\Omega t)\,dt = \frac{1}{2}\int_0^{T_0} \cos[(\omega_i - \Omega)t + \phi_i] - \cos[(\omega_i + \Omega)t + \phi_i]\,dt$$

$$= \left(\frac{T_0 \sin\phi_i}{2}\right)\delta[\omega_i - \Omega] \qquad (66)$$

This is essentially the procedure to obtain the coefficient at the reference frequency Ω in a Fourier series, regarding the input signal as composed of several superposed sinusoidal functions at different frequencies ($f(t) = \sum_{i=0}^{\infty} F_i \sin(\omega_i t + \phi_i)$).

With effect, we should be able to extract the desired signal as long as we (1) supply a reference signal at fixed frequency; (2) assure a modulation at the same frequency of the physical quantity one intends to measure and (3) suppress every other frequency besides the reference frequency.

(1) can be easily accomplished by utilizing a conventional signal generator.

(2) the tricky part is to assure a smooth modulation of the measured quantity, for it depends on the response of the physical system to a certain stimulus.

(3) Modern equipment such as DSP and FPGA can easily deliver this multiplication and integration over a period. Note however, that, for a $\omega_i = \Omega$, we get a constant term (frequency zero) and a twofold frequency term. Therefore, a low pass filter should suffice to allow only frequencies near the vicinity of Ω to pass through.

$$\sin(\omega_i t + \phi_i)\sin(\Omega t) = \frac{1}{2} - \cos[(\omega_i + \Omega)t + \phi_i]$$

In order to assure (2), one can disturb the input variable with a modulated stimulus near an equilibrium point ($\bar{p}$),

$$p(t) = \bar{p} + M\sin(\omega t)$$

Which, in turn, causes a variation in the output of the system. If the modulation amplitude (M) is small enough, the output signal can be expanded in a Taylor Series around the equilibrium point:

$$v[p(t)] = v(\bar{p}) + \frac{\frac{dv}{dp}(\bar{p})[\bar{p} + M\sin(\omega t) - \bar{p}]}{1!} + \cdots + \frac{\frac{d^n v}{dp^n}(\bar{p})[\bar{p} + M\sin(\omega t) - \bar{p}]^n}{n!}$$

$$= v(\bar{p}) + \frac{dv}{dp}(\bar{p})[M\sin(\omega t)] + O(M^2) \approx v(\bar{p}) + \frac{dv}{dp}(\bar{p})[M\sin(\omega t)]$$

Applying (66) into the expansion and dismissing higher frequency terms, the output will be,

$$v_{out}(t) = \left(\frac{MV_{ref}T_0\sin\phi_i}{2}\right)\frac{dv(\bar{p})}{dp}\delta[\omega_i - \Omega] = k\frac{dv(\bar{p})}{dp}\delta[\omega_i - \Omega] \qquad (67)$$

It is then important to notice that the output of the lock-in amplifier is proportional to the derivative of the physical system's output in relation to the modulated quantity (in our case, the magnetic field) at the equilibrium point $\bar{p}$.

3.1.5 Effective field and FMR frequency

Now let's work out an equation to correlate the data from a FMR measurement and the sample's characteristics. In a constant external field, the work done to magnetize a material (12) can be written in differential form as follows,

$$dE = -\mu_0 \boldsymbol{H_{eff}} \cdot d\boldsymbol{M}$$

So that the resultant field represents the gradient of the energy with respect to the magnetization,

$$\boldsymbol{H_{eff}} = -\frac{1}{\mu_0}\nabla_M E \tag{68}$$

Where small deviations in magnetization are given by,

$$\delta\boldsymbol{M} = \delta m_\rho \hat{\boldsymbol{\rho}} + \delta m_\theta \hat{\boldsymbol{\theta}} + \delta m_\varphi \hat{\boldsymbol{\varphi}}$$

For most purposes, one can assume a quasi-static regime at which $\boldsymbol{M}$ is aligned with the z axis, constant in magnitude and all deviations occur around this such that,

$$\delta m_\rho = 0 \qquad \delta m_\theta = M_z \delta\theta \qquad \delta m_\varphi = M_z sin\theta_0 \delta\varphi$$

Assuming that the system is initially balanced in an equilibrium position, we have,

$$\frac{\partial E(\boldsymbol{M_0})}{\partial m_\theta} = \frac{\partial E(\boldsymbol{M_0})}{\partial m_\varphi} = 0$$

So that the gradient in equation (68) is dominated by the second order terms, namely,

$$\frac{\partial E(\boldsymbol{M})}{\partial m_\theta} = \frac{\partial E(\boldsymbol{M_0})}{\partial m_\theta} + \frac{\partial^2 E(\boldsymbol{M_0})}{\partial {m_\theta}^2}\delta m_\theta + \frac{\partial^2 E(\boldsymbol{M_0})}{\partial m_\theta \partial m_\varphi}\delta m_\varphi \tag{69}$$

$$\frac{\partial E(\boldsymbol{M})}{\partial m_\varphi} = \frac{\partial E(\boldsymbol{M_0})}{\partial m_\varphi} + \frac{\partial^2 E(\boldsymbol{M_0})}{\partial {m_\varphi}^2}\delta m_\varphi + \frac{\partial^2 E(\boldsymbol{M_0})}{\partial m_\varphi \partial m_\theta}\delta m_\theta \tag{70}$$

Generally, it is more useful to express the differentials in terms of the angles' displacements, as in,

$$\frac{\partial^2 E}{\partial m_\theta^2} = \frac{\partial^2 E}{\partial \theta^2}\left(\frac{\partial \theta}{\partial m_\theta}\right)^2 = \frac{1}{M^2} E_{\theta\theta}$$

$$\frac{\partial^2 E}{\partial {m_\varphi}^2} = \frac{\partial^2 E}{\partial \varphi^2}\left(\frac{\partial \varphi}{\partial m_\varphi}\right)^2 = \frac{1}{(M sin\theta_0)^2} E_{\varphi\varphi}$$

$$\frac{\partial^2 E}{\partial m_\theta \partial m_\varphi} = \frac{\partial^2 E}{\partial m_\varphi \partial m_\theta} = \frac{\partial^2 E}{\partial \theta \partial \varphi}\left(\frac{\partial \theta}{\partial m_\theta}\right)\left(\frac{\partial \varphi}{\partial m_\varphi}\right) = \frac{1}{M^2 sin\theta_0} E_{\theta\varphi}$$

Those substituted into equations (69) and (70) give,

$$\left[\boldsymbol{H}_{eff}\right]_\theta = -\frac{1}{\mu_0}\frac{\partial E(\boldsymbol{M})}{\partial m_\theta} = -\frac{1}{\mu_0 M}\left(E_{\theta\theta}\delta\theta + E_{\theta\varphi}\delta\varphi\right) \tag{71}$$

$$\left[\boldsymbol{H}_{eff}\right]_\varphi = -\frac{1}{\mu_0}\frac{\partial E(\boldsymbol{M})}{\partial m_\varphi} = -\frac{1}{\mu_0 M sin\theta_0}\left(E_{\varphi\theta}\delta\theta + E_{\varphi\varphi}\delta\varphi\right) \tag{72}$$

$$\left[\boldsymbol{H}_{eff}\right]_\rho \propto \frac{\partial E(\boldsymbol{M})}{\partial m_\rho} = 0$$

Substituting these terms in the Landau-Lifshitz equation gives,

$$\frac{dm_\theta}{dt} = -\gamma M\left[\boldsymbol{H}_{eff}\right]_\varphi \tag{73}$$

$$\frac{dm_\varphi}{dt} = \gamma M\left[\boldsymbol{H}_{eff}\right]_\theta \tag{74}$$

Posed that in the resonance the magnetization follows the microwave fields,

$$m_\theta(t) = (M\delta\theta)e^{-i\omega_{rf}t} \qquad\qquad m_\varphi(t) = (M sin\theta_0 \delta\varphi)e^{-i\omega_{rf}t}$$

Equations (73) and (74) give a system of two equations,

$$(E_{\theta\theta})\delta\theta + \left(E_{\theta\varphi} - \frac{i\omega_0\mu_0 M sin\theta_0}{\gamma}\right)\delta\varphi = 0$$

$$\left(E_{\varphi\theta} + \frac{i\omega_0\mu_0 M sin\theta_0}{\gamma}\right)\delta\theta + \left(E_{\varphi\varphi}\right)\delta\varphi = 0$$

Or, in matrix form,

$$\begin{bmatrix} E_{\theta\theta} & E_{\theta\varphi} - \frac{i\omega_0\mu_0 M sin\theta_0}{\gamma} \\ E_{\varphi\theta} + \frac{i\omega_0\mu_0 M sin\theta_0}{\gamma} & E_{\varphi\varphi} \end{bmatrix} \begin{bmatrix} \delta\theta \\ \delta\varphi \end{bmatrix} = 0$$

The solution for the resonance frequency is obtained by equating the determinant to zero,

$$\omega_0 = \frac{\gamma}{\mu_0 M sin\theta_0}\left(E_{\theta\theta}E_{\varphi\varphi} - {E_{\theta\varphi}}^2\right)^{1/2} \quad (75)$$

This is the central equation for interpreting the outcomes of FMR experiments since it directly connects the resonance frequency/field with the energies' signatures from the internal magnetic mechanisms [10,18,25]. The usual course of action for characterizing a magnetic sample by FMR consists of scanning the resonance field at several angles, and then numerically fitting (75) into the experimental data.

3.1.6 Evaluating the energy contributions to the spectrum

In order to apply (75), we must evaluate the derivatives of the system's Hamiltonian, which consists of several contributions such as the Zeeman interaction, exchange interaction and magnetic anisotropy,

$$\mathcal{H} = \sum_i \mathcal{H}_i$$

After accounting with all of these concomitant phenomena, we may now write the resonance frequency equation. The following tables (**Table 4**, **Table 5**, **Table 6**, **Table 7**, **Table 8**, and **Table 9**) summarize the free energy terms and their derivatives. In this study, the scan of the field's incidence angle shall be carried out solely in the plane of the sample, thus keeping the polar (out-of-plane) angle constant, and largely simplifying the calculations.

Table 4 - Summary of Zeeman energy and its derivatives.

External field / Zeeman
$E_Z = -\mu_0 M H_0 \sin(\delta\theta_H)\cos(\delta\varphi_H)$
$\frac{\partial E_Z}{\partial \varphi} = \mu_0 M H_0 \sin(\delta\theta_H)\sin(\delta\varphi_H)$
$\frac{\partial E_Z}{\partial \theta} = -\mu_0 M H_0 \cos(\delta\theta_H)\cos(\delta\varphi_H)$
$\frac{\partial^2 E_Z}{\partial \varphi^2} = \mu_0 M H_0 \sin(\delta\theta_H)\cos(\delta\varphi_H)$
$\frac{\partial^2 E_Z}{\partial \theta^2} = \mu_0 M H_0 \sin(\delta\theta_H)\cos(\delta\varphi_H)$

Source: the author.

The boundary conditions give,

$$\left.\frac{\partial^2 E_Z}{\partial \theta^2}\right|_{\theta=\frac{\pi}{2}} = \left.\frac{\partial^2 E_Z}{\partial \varphi^2}\right|_{\theta=\frac{\pi}{2}} = \mu_0 M H_0 \tag{76}$$

$$\frac{\partial^2 E_Z}{\partial \theta \partial \varphi} = \frac{\partial^2 E_Z}{\partial \varphi \partial \theta} = \mu_0 M H_0 [\cos\theta_M \sin(\delta\varphi_H)]$$

$$\left.\frac{\partial^2 E_Z}{\partial \theta \partial \varphi}\right|_{\theta=\frac{\pi}{2}} = \left.\frac{\partial^2 E_Z}{\partial \varphi \partial \theta}\right|_{\theta=\frac{\pi}{2}} = 0$$

Table 5 - Summary of shape anisotropy energy and its derivatives.

Demagnetizing and surface anisotropy
$E_s = \frac{1}{2}\mu_0 M M_{eff} \cos^2 \theta_M$
$\frac{\partial E_s}{\partial \varphi} = 0$
$\frac{\partial E_s}{\partial \theta} = -\frac{1}{2}\mu_0 M M_{eff} \sin 2\theta_M$
$\frac{\partial^2 E_s}{\partial \varphi^2} = 0$
$\frac{\partial^2 E_s}{\partial \theta^2} = -\mu_0 M M_{eff} \cos 2\theta_M$

Source: the author.

So that,

$$\left.\frac{\partial^2 E_{dip}}{\partial \theta^2}\right|_{\theta=\frac{\pi}{2}} = \mu_0 M M_{eff} \tag{77}$$

$$\left.\frac{\partial^2 E_{dip}}{\partial \varphi^2}\right|_{\theta=\frac{\pi}{2}} = \left.\frac{\partial^2 E_{dip}}{\partial \theta \partial \varphi}\right|_{\theta=\frac{\pi}{2}} = \left.\frac{\partial^2 E_{dip}}{\partial \varphi \partial \theta}\right|_{\theta=\frac{\pi}{2}} = 0$$

Table 6 - Summary of exchange bias energy and its derivatives.

Exchange bias
$E_{EB} = -\mu_0 M H_{EB}[\cos\theta_M \cos\theta_{EB} + \sin\theta_M \sin\theta_{EB} \cos(\delta\varphi_{EB})]$
$\frac{\partial E_{EB}}{\partial \varphi} = -\mu_0 M H_{EB}[-\sin\theta_M \sin\theta_{EB} \sin(\delta\varphi_{EB})]$
$\frac{\partial E_{EB}}{\partial \theta} = -\mu_0 M H_{EB}[-\sin\theta_M \cos\theta_{EB} + \cos\theta_M \sin\theta_{EB} \cos(\delta\varphi_{EB})]$

$$\frac{\partial^2 E_{EB}}{\partial \varphi^2} = \mu_0 M H_{EB}[\sin\theta_M \sin\theta_{EB} \cos(\delta\varphi_{EB})]$$

$$\frac{\partial^2 E_{EB}}{\partial \theta^2} = \mu_0 M H_{EB}[\cos\theta_M \cos\theta_{EB} + \sin\theta_M \sin\theta_{EB} \cos(\delta\varphi_{EB})]$$

Source: the author.

The boundary conditions give,

$$\left.\frac{\partial^2 E_{EB}}{\partial \theta^2}\right|_{\theta=\pi/2} = \left.\frac{\partial^2 E_{EB}}{\partial \varphi^2}\right|_{\theta=\pi/2} = \mu_0 M H_{EB} \cos\varphi \tag{78}$$

$$\frac{\partial^2 E_{EB}}{\partial \theta \partial \varphi} = \frac{\partial^2 E_{EB}}{\partial \varphi \partial \theta} = \mu_0 M H_{EB}[\cos\theta \sin\theta_{EB} \sin(\varphi - \varphi_{EB})]$$

$$\left.\frac{\partial^2 E_{EB}}{\partial \theta \partial \varphi}\right|_{\theta=\pi/2} = \left.\frac{\partial^2 E_{EB}}{\partial \varphi \partial \theta}\right|_{\theta=\pi/2} = 0$$

Table 7 - Summary of uniaxial anisotropy energy and its derivatives.

Uniaxial anisotropy
$E_u = K_u \sin^2(\delta\theta_u) \sin^2(\delta\phi_u)$
$\frac{\partial E_u}{\partial \varphi} = K_u \sin^2(\delta\theta_u) \sin(2\delta\phi_u)$
$\frac{\partial E_u}{\partial \theta} = K_u \sin(2\delta\theta_u) \sin^2(\delta\phi_u)$

$$\frac{\partial^2 E_u}{\partial \varphi^2} = 2K_u \sin^2(\delta\theta_u)\cos(2\delta\phi_u)$$

$$\frac{\partial^2 E_u}{\partial \theta^2} = 2K_u \cos(2\delta\theta_u)\sin^2(\delta\phi_u)$$

Source: the author.

That gives,

$$\left.\frac{\partial^2 E_u}{\partial \theta^2}\right|_{\theta=\frac{\pi}{2}} = -2K_u \sin^2(\varphi_M - \phi_u) \quad (79)$$

$$\left.\frac{\partial^2 E_u}{\partial \phi^2}\right|_{\theta=\frac{\pi}{2}} = 2K_u \cos\ 2(\varphi_M - \phi_u) \quad (80)$$

Table 8 - Summary of first order cubic anisotropy energy and its derivatives.

First order cubic anisotropy
$E_{c1} = \frac{1}{4}K_{c1}[\sin^4(\delta\theta_c)\sin^2(2\delta\varphi_c) + \sin^2(2\delta\theta_c)]$
$\frac{\partial E_{c1}}{\partial \varphi} = \frac{1}{2}K_{c1}\sin^4(\delta\theta_c)\sin(4\delta\varphi_c)$
$\frac{\partial E_{c1}}{\partial \theta} = K_{c1}\left[\sin^2(2\delta\varphi_c)\sin^3(\delta\theta_c)\cos(\delta\theta_c) + \frac{1}{2}\sin(4\delta\theta_c)\right]$
$\frac{\partial^2 E_{c1}}{\partial \varphi^2} = 2K_{c1}\sin^4(\delta\theta_c)\cos(4\delta\varphi_c)$
$\frac{\partial^2 E_{c1}}{\partial \theta^2} = K_{c1}\{\sin^2(2\delta\varphi_c)\,[3\sin^2(\delta\theta_c)\cos^2(\delta\theta_c) - \sin^4(\delta\theta_c)] + 2\cos(4\delta\theta_c)\}$

Source: the author.

Unlike the other energies, the cubic anisotropy energy depends largely on the growth plane of the sample. For samples grown in the $\{100\}$ planes ($\theta_{c1} = 0, \theta_M = \pi/2$), we get,

$$\left.\frac{\partial^2 E_{c1}}{\partial\theta^2}\right|_{<100>} = K_{c1}(2-\sin^2 2\varphi_H) = \frac{K_{c1}}{2}[3+\cos 4(\varphi_H-\varphi_c)] \tag{81}$$

$$\left.\frac{\partial^2 E_{c1}}{\partial\varphi^2}\right|_{<100>} = 2K_{c1}\cos 4\varphi_H \tag{82}$$

$$\frac{\partial^2 E_{c1}}{\partial\theta\partial\varphi} = \frac{\partial^2 E_{c1}}{\partial\varphi\partial\theta} = 2K_{c1}\sin 4\varphi\sin^3\theta\cos\theta$$

$$\left.\frac{\partial^2 E_{c1}}{\partial\theta\partial\varphi}\right|_{<100>} = 0$$

Table 9 - Summary of second order cubic anisotropy energy and its derivatives.

Second order cubic anisotropy
$E_{c2} = \frac{1}{64}K_{c2}[1-\cos(2\delta\theta_c)-\cos^2(2\delta\theta_c)+\cos^3(2\delta\theta_c)][1-\cos(4\delta\varphi_c)]$
$\frac{\partial E_{c2}}{\partial\varphi} = \frac{1}{16}K_{c2}[1-\cos(2\delta\theta_c)-\cos^2(2\delta\theta_c)+\cos^3(2\delta\theta_c)][\sin(4\delta\varphi_c)]$
$\frac{\partial E_{c2}}{\partial\theta} = \frac{1}{64}K_{c2}\{\sin(2\delta\theta_c)\,[2-12\cos^3(2\delta\theta_c)]+2\sin(4\delta\theta_c)\}[1-\cos(4\delta\varphi_c)]$
$\frac{\partial^2 E_{c2}}{\partial\varphi^2} = \frac{1}{64}K_{c2}[1-\cos(2\delta\theta_c)-\cos^2(2\delta\theta_c)+\cos^3(2\delta\theta_c)][\cos(4\delta\varphi_c)]$
$\frac{\partial^2 E_{c2}}{\partial\theta^2} = \frac{1}{64}K_{c2}[4\cos(2\delta\theta_c)-24\cos^4(2\delta\theta_c)+144\sin^2(2\delta\theta_c)\cos^3(2\delta\theta_c)+8\cos(4\delta\theta_c)][1-\cos(4\delta\varphi_c)]$

Source: the author.

Likewise, the boundary conditions give,

$$\left.\frac{\partial^2 E_{c2}}{\partial\theta^2}\right|_{<100>} = \frac{K_{c2}}{64}(1-\cos 4\varphi)(-4-24+0+8)$$

$$\left.\frac{\partial^2 E_{c2}}{\partial\theta^2}\right|_{<100>} = \frac{10K_{c2}}{32}[1-\cos 4(\varphi_M-\phi_{C2})] \tag{83}$$

$$\left.\frac{\partial^2 E_{C2}}{\partial\varphi^2}\right|_{<100>} = \frac{K_{c2}}{64}(1+1-1-1)\cos 4\varphi = 0$$

$$\frac{\partial^2 E_{c2}}{\partial\theta\partial\varphi} = \frac{K_{c2}}{16}[\sin 2\theta\,(2-12\cos^3 2\theta)+2\sin 4\theta](\sin 4\varphi)$$

$$\left.\frac{\partial^2 E_{c2}}{\partial\theta\partial\varphi}\right|_{<100>} = 0$$

$$\frac{\partial E_{c2}}{\partial\varphi} = \frac{K_{c2}}{16}(1+1-1\pm 1)(\sin 4\varphi) = 0$$

Assembling all of these we get for the (100) plane, $E_{\theta\varphi}=0$ and,

$$E_{\theta\theta} = \left[\frac{\partial^2 E_Z}{\partial\theta^2}+\frac{\partial^2 E_{dip}}{\partial\theta^2}+\frac{\partial^2 E_{EB}}{\partial\theta^2}+\frac{\partial^2 E_u}{\partial\theta^2}+\frac{\partial^2 E_{c1}}{\partial\theta^2}+\frac{\partial^2 E_{c2}}{\partial\theta^2}\right]\Bigg|_{\theta=\pi/2,\varphi=\varphi_0}$$

$$= \Big[\mu_0 MH_R+\mu_0 MM_{eff}+\mu_0 MH_{EB}\cos\varphi-2K_u\sin^2(\varphi_H-\phi_u)$$

$$+2K_{c1}\left(1-\frac{1}{2}\sin^2 2\varphi\right)+\frac{10K_{c2}}{32}[1-\cos 4(\varphi_M-\phi_{C2})]\Big]$$

$$E_{\varphi\varphi} = \left[\frac{\partial^2 E_Z}{\partial\varphi^2}+\frac{\partial^2 E_{dip}}{\partial\varphi^2}+\frac{\partial^2 E_{EB}}{\partial\varphi^2}+\frac{\partial^2 E_u}{\partial\varphi^2}+\frac{\partial^2 E_{MC}}{\partial\varphi^2}+\frac{\partial^2 E_{C2}}{\partial\varphi^2}\right]\Bigg|_{\theta=\pi/2,\varphi=\varphi_0}$$

$$= [\mu_0 MH+\mu_0 MH_{EB}\cos\varphi+2K_u\cos\,2(\varphi_H-\phi_u)+2K_{c1}\cos 4\varphi]$$

That, substituted in equation (75) gives in the CGS system,

$$\omega_0 = \frac{\gamma}{\mu_0 M sin\theta_0}\left(E_{\theta\theta}E_{\varphi\varphi} - {E_{\theta\varphi}}^2\right)^{1/2}$$

$$\begin{aligned}\omega_0 = \gamma\Big[&H_R\cos(\varphi_M-\varphi_H) + \frac{K_{c1}}{2M}(3+\cos 4(\varphi_M-\phi_C)) + \frac{10K_{c2}}{32M}[1-\cos 4(\varphi_M-\phi_{C2})]\\ &+ 4\pi M_{eff} + H_{EB}\cos(\varphi_M-\varphi_{EB})\\ &- \frac{2K_u}{M}\sin^2(\varphi_M-\phi_U)\Big]^{1/2}\Big[H_R\cos(\varphi_M-\varphi_H) + \frac{2K_{c1}}{M}\cos 4(\varphi_M-\phi_C)\\ &+ H_{EB}\cos(\varphi_M-\phi_{EB}) + \frac{2K_u}{M}\cos\ 2(\varphi_M-\phi_U)\Big]^{1/2}\end{aligned}$$

Or, in terms of effective anisotropy fields, $\frac{2K_i}{M} = H_i$,

$$\begin{aligned}\omega_0 = \gamma\Big[&H_R\cos(\varphi_M-\varphi_H) + \frac{H_{c1}}{4}(3+\cos 4(\varphi_M-\phi_{c1}))\\ &+ \frac{5H_{c2}}{32}[1-\cos 4(\varphi_M-\phi_{c2})] + 4\pi M_{eff} + H_{EB}\cos(\varphi_M-\varphi_{EB})\\ &- H_U\sin^2(\varphi_M-\phi_U)\Big]^{1/2}[H_R\cos(\varphi_M-\varphi_H) + H_C\cos 4(\varphi_M-\phi_C)\\ &+ H_{EB}\cos(\varphi_M-\phi_{EB}) + H_U\cos\ 2(\varphi_M-\phi_U)]^{1/2}\end{aligned} \tag{84}$$

We now have the general dependence of the resonance frequency/field with the magnetization azimuthal angle. In order to numerically obtain the sample's magnetic parameters, we must isolate the resonance field. This is done by noticing that equation (84) is a second order polynomial equation on H_R,

$$A_{100}H_R^2 + B_{100}H_R + C_{100} = 0$$

$$H_R = \frac{-B_{100} + \sqrt{B_{100}^2 - 4A_{100}C_{100}}}{2A_{100}} \tag{85}$$

Where,

$$A_{100} = H_R^2[\cos^2(\varphi_M - \varphi_H)]$$

$$B_{100} = H_R \cos(\varphi_M - \varphi_H)\left[H_{C1}(1 + 2\cos 4(phiM)) + \frac{5H_{c2}}{32}[1 - \cos 4(\varphi_M - \phi_{c2})] + 2H_{EB}\cos\varphi M + 4\pi M_{eff}\right]$$

$$C_{100} = \left[\frac{H_{c1}}{4}(3 + \cos 4(\varphi_M - \phi_{c1})) + \frac{5H_{c2}}{32}[1 - \cos 4(\varphi_M - \phi_{c2})] + 4\pi M_{eff} + H_{EB}\cos(\varphi_M - \varphi_{EB}) - H_U \sin^2(\varphi_M - \phi_U)\right][H_C \cos 4(\varphi_M - \phi_C) + H_{EB}\cos(\varphi_M - \phi_{EB}) + H_U \cos\ 2(\varphi_M - \phi_U)] - \left(\frac{\omega_0}{\gamma}\right)^2$$

And the magnetization's equilibrium condition is given by nulling the first derivative,

$$H_0 \sin(\varphi_M - \varphi_H) - \frac{1}{4}H_{c1}\sin 4(\varphi_M - \varphi_C) - \frac{H_u}{2}\sin 2(\varphi_M - \varphi_U) = 0 \qquad (86)$$

3.1.7 Samples grown on planes $\{\mathbf{111}\}$

As discussed, the cubic anisotropy is especially sensitive to the plane of growth of the sample. While planes $\{100\}$ put the cubic symmetry axis parallel to the plane of the sample ($\theta_C = 0 \rightarrow \theta_M - \theta_C = \pi/2$), the tilting in relation to the plane of the sample must be accounted for materials grown in the plane (111). Consider that the sample is in the xy plane, and that the cubic crystal is in a tilted coordinate plane, say $x'y'$, so that,

$$\boldsymbol{x} = a\hat{\boldsymbol{x}} \qquad\qquad \boldsymbol{y} = a\hat{\boldsymbol{y}}$$

$$\boldsymbol{x}' = a(\hat{\boldsymbol{x}} - \hat{\boldsymbol{z}}) \rightarrow |\boldsymbol{x}'| = a\sqrt{2} \qquad\qquad \boldsymbol{y}' = a(\hat{\boldsymbol{y}} - \hat{\boldsymbol{z}})$$

To find the angle between the coordinate systems, let's build an orthogonal basis for the plane (111) by the Gram-Schmidt process. The component of y' that is perpendicular to x' is,

$$\boldsymbol{y}'_{\perp} = \boldsymbol{y}' - \frac{(\boldsymbol{y}' \cdot \boldsymbol{x}')\boldsymbol{x}'}{|\boldsymbol{x}'|^2} = a(\hat{\boldsymbol{y}} - \hat{\boldsymbol{z}}) - \frac{a(\hat{\boldsymbol{x}} - \hat{\boldsymbol{z}})}{2} = a\left(\hat{\boldsymbol{y}} - \frac{\hat{\boldsymbol{x}}}{2} - \frac{\hat{\boldsymbol{z}}}{2}\right)$$

$$|\boldsymbol{y}'_{\perp}| = a\sqrt{3/2}$$

Now we find the normal of the planes xy and $x'y'$, that is: $\hat{\boldsymbol{z}}$ and $\widehat{\boldsymbol{z}'}$

$$\begin{aligned}\hat{\boldsymbol{z}}' &= \frac{(\boldsymbol{x}' \times \boldsymbol{y}'_{\perp})}{\sin(\pi/2)|\boldsymbol{x}'||\boldsymbol{y}'_{\perp}|} = \frac{1}{\sqrt{3}}\left[(\hat{\boldsymbol{x}} - \hat{\boldsymbol{z}}) \times \left(\hat{\boldsymbol{y}} - \frac{\hat{\boldsymbol{x}}}{2} - \frac{\hat{\boldsymbol{z}}}{2}\right)\right] \\ &= \frac{1}{\sqrt{3}}\left[(\hat{\boldsymbol{x}} \times \hat{\boldsymbol{y}}) - \frac{(\hat{\boldsymbol{x}} \times \hat{\boldsymbol{x}})}{2} - \frac{(\hat{\boldsymbol{x}} \times \hat{\boldsymbol{z}})}{2} - (\hat{\boldsymbol{z}} \times \hat{\boldsymbol{y}}) + \frac{(\hat{\boldsymbol{z}} \times \hat{\boldsymbol{x}})}{2} + \frac{(\hat{\boldsymbol{z}} \times \hat{\boldsymbol{z}})}{2}\right] \\ &= \frac{1}{\sqrt{3}}(\hat{\boldsymbol{x}} + \hat{\boldsymbol{y}} + \hat{\boldsymbol{z}})\end{aligned}$$

Finally, we find the angle between the coordinate systems to be,

$$\delta\theta_C = ang(\hat{\boldsymbol{z}}, \hat{\boldsymbol{z}}') = \cos^{-1}\left(\frac{\hat{\boldsymbol{z}} \cdot \hat{\boldsymbol{z}}'}{|\hat{\boldsymbol{z}}||\hat{\boldsymbol{z}}'|}\right) = \cos^{-1}\left(\frac{1}{\sqrt{3}}\right) \approx -54.7356°$$

Moreover, one may notice that the angle between $\hat{\boldsymbol{x}}'$ and $\hat{\boldsymbol{y}}'$ is

$$\cos^{-1}\left(\frac{\hat{\boldsymbol{z}} \cdot \hat{\boldsymbol{z}}}{2}\right) = 60°$$

Since this represents the angle at which the unit base's atoms are at, there should be a hindrance at these points, possibly leading to some deformation in the cubic anisotropy periodicity provided the easy axes change its angular configuration, as in **Table 10**.

Table 10 - Angles of symmetry axes in (100) and (111) planes.

Azimuthal angle of easy axes in (100) plane	Azimuthal angle of easy axes in (111) plane
0°	0°
90°	60°
180°	180°

$270°$	$240°$

Source: the author.

By considering $\delta\theta_C \approx -54.7356°$, we can adapt the dispersion relation (84) to the (111) grown crystal,

$$\begin{aligned}\omega_0 = \gamma\{&H_R\cos(\varphi_M-\varphi_H)+H_{c1}[-0.77775+0.1111\sin^2 2(\varphi_M-\phi_c)]\\&+H_{c2}(0.11690295)[-1+\cos 4(\varphi_M-\phi_C)]+4\pi M_{eff}\\&+H_{EB}\cos(\varphi_M-\varphi_{EB})\\&-H_u(0.5)[1-\cos 2(\varphi_M-\phi_u)]\}^{1/2}\{H_R\cos(\varphi_M-\varphi_H)\\&+H_{c1}[0.44445\cos 4(\varphi_M-\phi_c)]\\&+H_{c2}[0.009259259257\cos 4(\varphi_M-\phi_c)]+H_{EB}\cos(\varphi_M-\phi_{EB})\\&+H_u\cos\ 2(\varphi_M-\phi_u)\}^{1/2}\end{aligned} \tag{87}$$

Or, isolating the resonance field,

$$H_R=\frac{-B_{111}+\sqrt{B_{111}^2-4A_{111}C_{111}}}{2A_{111}} \tag{88}$$

Where,

$$A_{111}=\cos^2(\varphi_M-\varphi_H)$$

$$\begin{aligned}B_{111}=\cos(\varphi_M-\varphi_H)\{&H_{c1}[0.77775+0.4445\cos 4\varphi_M-0.1111\sin^2 2(\varphi_M-\phi_c)]\\&+H_{c2}[-0.11690295+0.1261622\cos 4(\varphi_M-\phi_c)]\\&+H_u[0.5+1.5\cos 2(\varphi_M-\phi_u)]+H_{EB}[2\cos(\varphi_M-\phi_{EB})]+4\pi M_{eff}\}\end{aligned}$$

$$\begin{aligned}C_{111}=\{&H_{c1}[-0.77775+0.1111\sin^2 2(\varphi_M-\phi_c)]\\&+H_{c2}(0.11690295)[-1+\cos 4(\varphi_M-\phi_c)]+4\pi M_{eff}+H_{EB}\cos(\varphi_M\\&-\varphi_{EB})-H_u(0.5)[1-\cos 2(\varphi_M-\phi_u)]\}\{H_{c1}[0.44445\cos 4(\varphi_M-\phi_c)]\\&+H_{c2}[0.009259259257\cos 4(\varphi_M-\phi_c)]+H_{EB}\cos(\varphi_M-\phi_{EB})\\&+H_u\cos\ 2(\varphi_M-\phi_u)\}-\left(\frac{\omega_0}{\gamma}\right)^2\end{aligned}$$

And the positions of equilibrium of the magnetization are,

$$H_R \sin(\varphi_M - \varphi_H) - H_{c1}[0.11111 \sin 4(\varphi_M - \phi_c)] - H_{c2}[0.037037 \sin 4(\varphi_M - \phi_c)] - H_u[0.5 \sin 2(\varphi_M - \phi_u)] = 0 \quad (89)$$

Those expressions have all been fed to a code in *python* (**APPENDIX**) to numerically compute the desired magnetic parameters. The code starts reading the data from resonance field versus application angle. Then, it finds the equilibrium position of the magnetization at all angles by minimizing the free energy (equations 86 and 89). Finally, it fits either equation (85) or (88) into the data whether the sample was grown in planes $\{100\}$ or $\{111\}$, respectively. The fit employs the function *curve_fit* from *scipy* library, that solves a non-linear least-squares problem with bounds on the variables by minimizing the sum of the residuals' squares. This process may be iteratively repeated several times feeding the new initial parameters with the output from the previous iteration.

3.2 Techniques for attaining magnetization curves

Magnetic materials may be placed into one of three groups: permanent magnets, high permeability materials and magnetic recording materials. Usually, each material's application is determined by its hysteresis loop, which is a curve that depicts the magnetic field induction ($\boldsymbol{B}$) against the applied magnetic field. Several techniques are available to raise the hysteresis loop of magnetic samples, two of which are used in this work: the vibrating-sample magnetometer (VSM) and the magneto-optical Kerr effect spectroscopy (MOKE).

In VSM, a sample is subjected to a constant magnetic field that orients the sample's magnetic dipole moment towards the poles of pickup coils. Then, piezoelectric materials put the sample in an up and down vibration motion, causing a varying magnetic field which is detected by the Faraday's law of induction thus enabling measurement of the total magnetization of the sample. On the other hand, the MOKE spectroscopy consists of throwing light over a sample and measuring the shift in the angle of polarization from the reflected beam. This shift is proportional to the local magnetization by the magneto-optical Kerr effect (MOKE), thus enabling the measurement of important parameters such as coercive field, saturation field and exchange bias fields relatively easily. Moreover, since the laser's transverse section is

small, it is possible to raise the magnetization curves region-wise throughout the magnetic film, so that MOKE spectroscopy makes it relatively easy to characterize more complicated films.

3.3 Sputtering deposition

With the success of vacuum technology in sustaining very low pressures (about $10^{-11} - 10^{-9}\ \mathrm{Torr}$ in volumes at the order of $1\ \mathrm{m}^3$), layer by layer deposition of thin films have spread out as one of the main manufacturing techniques in the investigation of thin films. In general, deposition techniques consist of gradual deposition of atoms/molecules over the surface of a neutral material, called the **substrate**; and can be carried out in a variety of methods, depending on composition, structure, thickness, and application.

The processes consist of three steps: (1) the raw material (called **target**) is fragmented into neutral atoms, ions, or molecules by the action of some thermal source (e.g.: plasma, laser, electron bombardment, accelerated ions, etc.); then, (2) the fluid consisting of the fragments of the substance is accelerated towards the substrate; and, finally, (3) the fragments deposited in the substrate interact physically and chemically leading to nucleation processes that ultimately form larger portions of the material.

In thermodynamics, nucleation is the first step in the formation of either a new thermodynamic phase or structure via self-assembly within a substance or mixture. It happens when an unusually large fluctuation occurs, in contrast with the common low amplitude fluctuations, thus triggering the transition: the new phase nucleus begins to expand instead of decay. The rate of nucleation is very sensitive to impurities in the system, occurring differently depending on the region of the sample. Whereas near surfaces there is the formation of heterogeneous nucleation sites, apart from the surface there will be more homogeneous nucleation sites.

Cathodic vaporization, or sputtering deposition, is a deposition technique widely employed in industry for production of thin films and multilayers [24]. First, the chamber is evacuated to very low pressures ($10^{-11} - 10^{-8}\ \mathrm{Torr}$) for several hours in order to eliminate residual gases and impurities. Next, a noble gas (e.g.: Ar, Ne) is injected into the chamber, forming an atmosphere with pressure in the order of $10^{-3}\ \mathrm{Torr}$. Then a voltage is applied between the substrate (cathode) and the target

(anode), simultaneously ionizing the gas into a plasma state ($e^- + Ar \leftrightarrow 2e^- + Ar^+$); and accelerating the Ar^+ ions towards the target with enough kinetic energy to fragment the raw material. This forms a vapor that, in turn, settles down over the substrate's surface.

Figure 17 - Illustration of sputtering deposition.

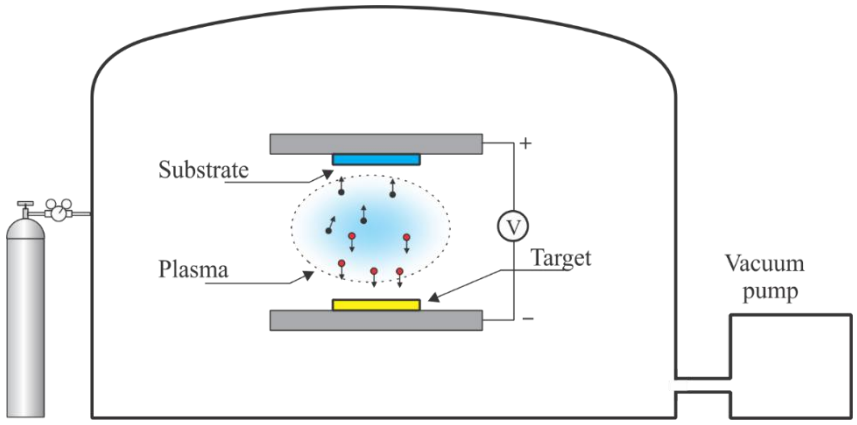

Source: Rezende (2022).

Moreover, by using different targets, it is possible to pile up layers of several materials forming a multilayer. Current cathodic vaporization systems employ magnetic fields to confine the plasma in the target's vicinity, thus enhancing the efficiency of the deposition process, this configuration is called magnetron sputtering. Naturally, it is important to adjust the voltage in order to minimize elastic collisions or penetrations into the target, which are detrimental to the quality of the film. For metals and other conductors, a DC voltage is applied; whereas in the case of insulators, a radiofrequency AC voltage is used to bypass the high resistance of the material, exploiting the reactive terms of the impedance.

3.4 Liquid phase epitaxy

The lattice-matched crystalline growth of one material over another is called epitaxy. In this work a few samples of yttrium iron garnet were produced by a homemade liquid phase epitaxy (LPE) system. This growth process exploits the fact

that is possible to grow monocrystals of certain materials at temperatures much lower than their fusion point due to the properties of mixtures of two substances.

In LPE a supersaturated solution of the material to be grown is brought into contact with the substrate for a certain period of time. If the substrate is single crystalline and the material to be grown has nearly the same lattice constant as the substrate, some of the material precipitates on the substrate while maintaining the crystalline quality. Thus, the precipitated material forms a lattice-matched epitaxial layer on the surface of the substrate. LPE is most frequently employed to produce semiconductor devices, and garnets of yttrium iron and rare earth materials. Its main advantages include high purity of outcomes, with wide variety of dopants available, lower cost than other epitaxy techniques, and high growth rate.

3.5 Magnetic annealing

In this work we study the effect of annealing with magnetic field in the magnetic anisotropies of YIG/IrMn thin films. By increasing the temperature and pressure the crystal lattice rearranges itself in a process of allotropy. In the case of alloys, allotropy stands for an element becoming soluble in the base element, followed by diffusion spreading of the solute towards a homogeneous distribution throughout the base metal. Then, when the solute is cooled back to their insoluble state, the dissolved constituents surge out of the solution, regrouping at the grain-boundaries. This precipitation ignites nucleation, which is the process of formation of the smallest stable aggregates of a crystalline phase.

Annealing is a heat treatment that consists of heating up a material above its recrystallization temperature for a set amount of time before cooling. It works in three stages: (1) recovery: increase temperature until the internal stresses are relieved; (2) recrystallization: formation of new grains; and (3) granulation: growth of grains. In this stage, the grain size and phase composition have strong dependence on the cooling rate. Magnetic annealing stands for annealing performed with magnetic field. The induced magnetization aligns the atomic magnetic moments, introducing magnetic symmetry in the lattice's formation. It causes irreversible changes in structure-sensitive magnetic properties, affecting properties such as magnetostriction and magnetoresistance [6].

4 EXPERIMENTAL RESULTS

I hereby present the results of this investigation on the origins of exchange bias in FM/AFM bilayers, as well as the effects of introducing antimony interlayers between these FM/AFM junctions. The FM layers (here standing for ferrimagnet and ferromagnet) employed are permalloy and yttrium iron garnet, or $Ni_{81}Fe_{19}$ (Py) and $Y_3Fe_5O_{12}$ (YIG); and the antiferromagnet of choice is iridium manganese, or $Ir_{20}Mn_{80}$ (IrMn). Samples were grown in the (111) plane in order to favor exchange coupling with IrMn [2].

Antiferromagnetic spintronics is a thriving field. AFMs possess excellent magnetotransport properties which would allow the generation of large spin currents through which magnetization in an adjacent FM layer could be efficiently switched [9,38]. AFMs also offer dynamics in the terahertz range suitable for ultrafast information processing [28]. In this picture, iridium manganese is a central material due to convenient features such as metallic nature, high Néel temperature and exceptionally high magnetocrystalline anisotropy. It has been observed in many crystallographic phases depending on the arrangement of iridium and manganese atoms in the unit cell, resulting in a variety of crystallographic and magnetic structures, although the majority of the structures found in spintronics can be considered to have an underlying *fcc* lattice (**Figure 18**) due to the large Ir atoms spacing out the Mn atoms.

Figure 18 - Face-centered cubic (*fcc*) conventional cell.

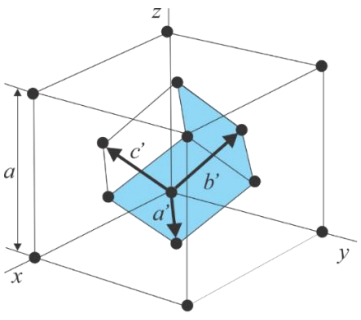

Source: Rezende (2022).

Regarding the fabrication processes used in this work, sputtering deposition was the most used since all samples were partially or completely fabricated this way. The sputtering system used here is the **Balzers-Pfeiffer PLS 500**, which comprises

gas injection system, pumping system, DC power supply, *rf* generator, rotary substrate holder that enables multilayer deposition, quartz crystal microbalance, and space for complementary accessories (**Figure 19**). It is general procedure to heat the chamber at temperatures near $120\ °\mathrm{C}$ for a couple hours in order to remove moisture before initiating the process. Then, high vacuum is established (at the order of $10^{-7}\ \mathrm{Torr}$) at room temperature until it is time for deposition, when the argon flow kicks in, thus increasing the pressure to the order of $10^{-3}\ \mathrm{Torr}$.

Figure 19 - Photograph of the sputtering deposition equipment. (a) Balzers-Pfeiffer PLS 500 system. (b) rotary substrate holder.

(a) (b)

Source: the author.

The FMR setup is homemade (**Figure 20**), consisting of a sweep oscillator with frequency stabilized at the resonance of a microwave cavity. The cavity is rectangular, with a quality factor $Q = 2500$ in the TE_{102} mode and is kept fixed relative to the poles of a **Varian 9" magnet**. Helmholtz coils on the cavity walls modulate the field at $1\ \mathrm{kHz}$. The samples were cut in rectangular shape, glued to the end face of a phenolic rod, and located at the center of the cavity. The rod, in turn, is mounted on a goniometer that enables control of the sample's angle in relation to the magnetic field axis. The gaussmeter is **F.W. Bell model 9640**, and the lock-in amplifier is a **Signal Recovery 7265 DSP Lock-in amplifier**.

Figure 20 - Photograph of FMR setup. (a) electromagnet field control. (b) electromagnet's coil, resonant cavity, microwave bridge and Helmholtz coil. (c) rf generator and modulation control. (d) goniometer.

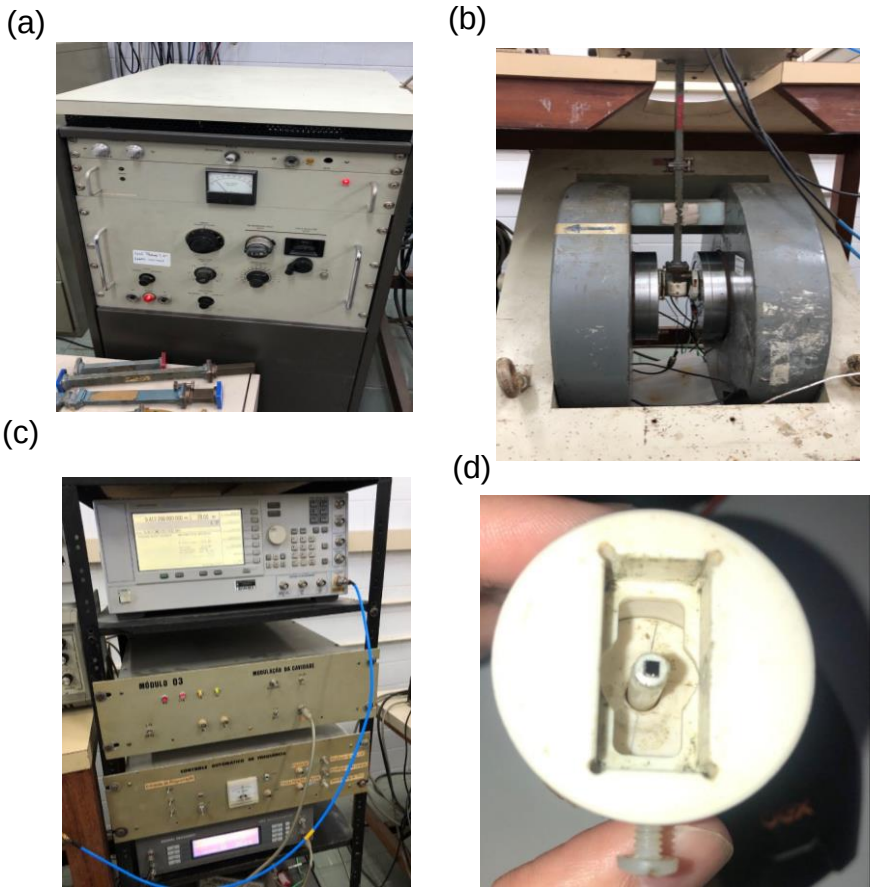

Source: the author.

4.1 Effect of magnetic annealing in YIG/IrMn thin films

YIG, as many ferrites, respond to magnetic anneal [41]. In this section, the effects of magnetic annealing on YIG/IrMn thin films are studied. At first, YIG(30nm) samples were sputtering deposited (parameters given in **Table 11**), followed by a post-deposition two-step heat treatment in O_2 pressure near $0.4\ \mathrm{kgf/cm^3}$. Then, the samples were heated at a rate of $10\ °\mathrm{C/min}$ until $700\ °\mathrm{C}$, kept at this temperature for 60 minutes; then cooled down to room temperature at a rate of $0.1\ °\mathrm{C/min}$. Finally, the samples were heated at the same $10\ °\mathrm{C/min}$ rate until $550\ °\mathrm{C}$, kept in this level for 30 minutes, and cooled down again at the $0.1\ °\mathrm{C/min}$ rate. After confirming the quality of the film, the $Ir_{20}Mn_{80}$ (74nm) layer was deposited by sputtering.

Table 11 - Deposition parameters of sample 1.

Target	Deposition time	Dep. rate $\left(\mathrm{nm}/\mathrm{min}\right)$	Pressure (Torr)	Ag flux (sccm)	Plasma		
					$I(\mathrm{mA})$	$P(\mathrm{W})$	$V(\mathrm{V})$
YIG	$11\,\mathrm{min}\,54\,\mathrm{s}$	2.52	9.4×10^{-4}	550	--	80	$235(rms)^*$
IrMn	$10\,\mathrm{min}$	7.4	4×10^{-3}	840	50	16	297

*In the case of YIG the voltage is in alternate current.

Source: the author.

With the bilayer ready, annealing with magnetic field ($H = 4\,\mathrm{kOe}$) was carried out. The heating element, a resistive wire ($R = 3.5\,\Omega$), wraps around the metallic sample holder (**Figure 21**) while being manually energized by a **Hewlett-Packard 6274B DC power supply**. At the highest temperature achieved ($600\,°\mathrm{C}$), the DC current was set to about $9\,\mathrm{A}$. The temperature near the sample is probed by a thermocouple sharing the same metallic plate as the sample.

Figure 21 - Heating element. (a) Inner part. (b) Housing.

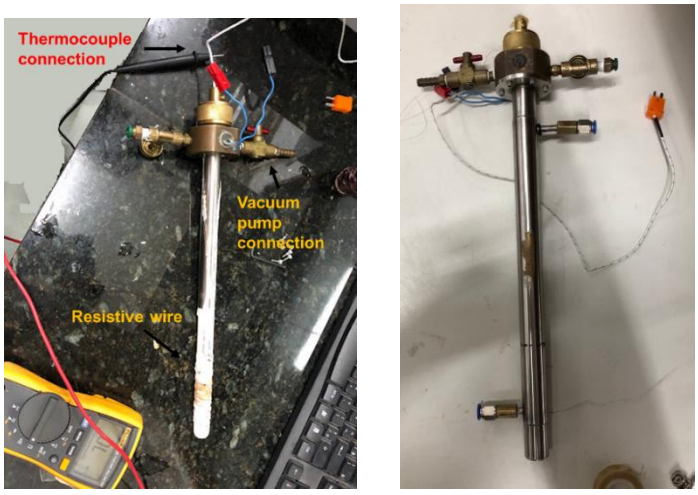

(a) (b)

Source: the author.

Moreover, a flowing water-cooling system is employed to prevent overheating, and the hot site is thermally isolated from the external environment by vacuum produced by a pump that draws the air out of the space between the resistive wire and the equipment housing. **Figure 22** shows the complete system.

Figure 22 - Setup employed to perform annealing with magnetic field. (a) Side view. (b) Front view.

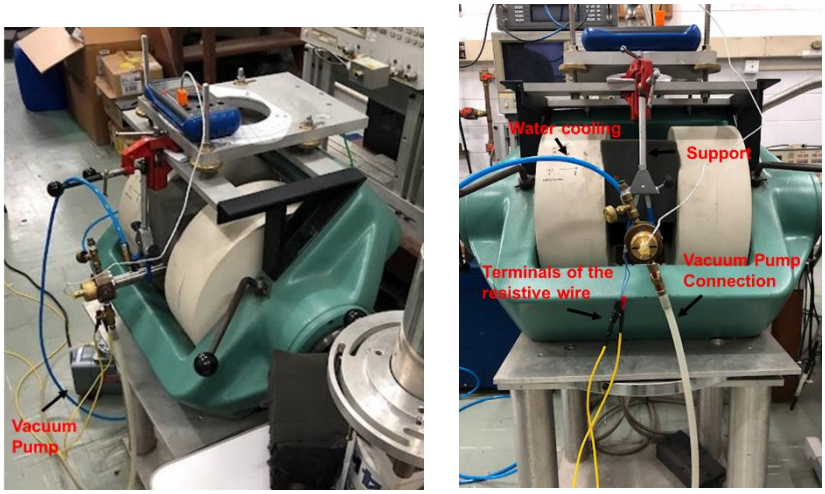

(a) (b)

Source: the author.

4.1.1 Sample 1 – YIG(30nm)/IrMn(74nm)

Sample 1 was heated up to $570\ °C$ ($843.15\ K$), which is well above the Curie temperature of YIG ($286\ °C / 559\ K$), and slightly lower than the estimated Néel temperature of $Ir_{20}Mn_{80}$ of about $600\ °C$ ($873.15\ K$); and then let cool down naturally to room temperature. After the first annealing, FMR measurements were carried out. **Figure 23** shows the derivative of power absorbed for one of the measurements.

Figure 23 – Derivative of power absorption. Output obtained from the FMR measurement in sample 1 after first annealing. The experiments ran with rf power at $20\ \mathrm{dbm}$, $\omega_{rf} = 9.418\ \mathrm{GHz}$, and Gaussmeter scale at $1\ \mathrm{kOe}$.

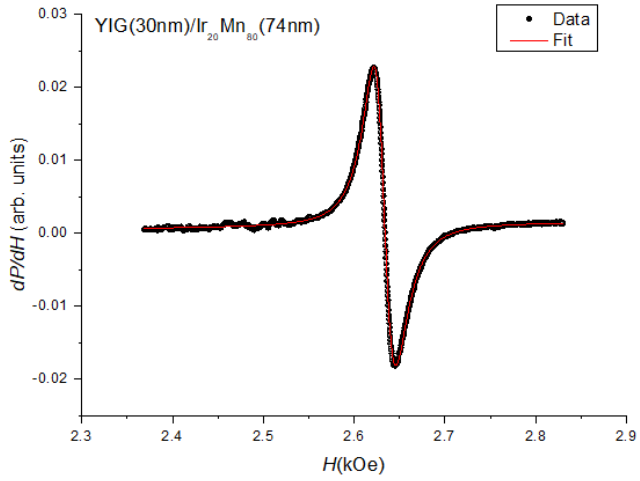

Source: the author.

The resonance field versus angle of the applied field is plotted in **Figure 24**, along with the curve from Equation 88 numerically fitted to the data with standard deviation $\sigma = 3\ \mathrm{Oe}$.

Figure 24 - Plot of resonance field versus applied field angle for sample 1 after first annealing. Red dots stand for data. Blue solid line for fitted curve. Black dashed line for the exchange bias contribution.

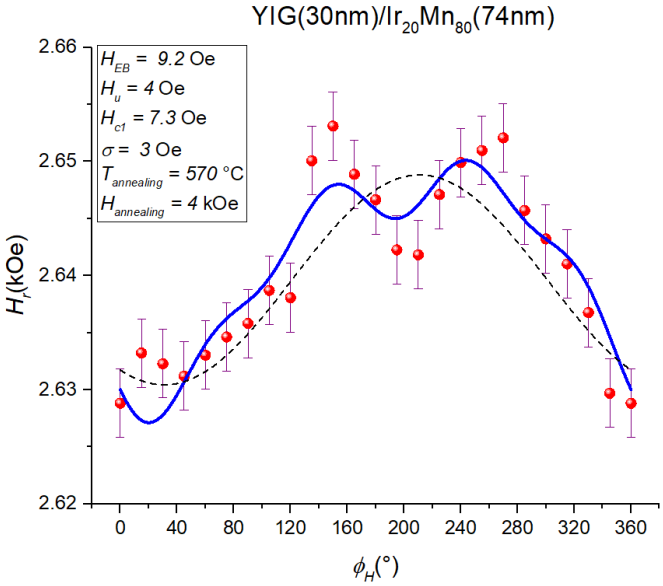

Source: the author.

Uniaxial anisotropy ($H_u = 4\ \mathrm{Oe}$) was induced as a consequence of the directional order from the magnetic field during annealing. The obtained cubic anisotropy field ($H_{c1} = 7.3\ \mathrm{Oe}$) confirms the cubic crystal structure of YIG. Remarkably, the fitted exchange bias field ($H_{EB} = 9.2\ \mathrm{Oe}$) is about seven times larger than previous measurements in the same sample prior to magnetic annealing [36].

Next, the same sample was subjected to a second annealing with applied field $4\ \mathrm{kOe}$ and maximum temperature $400\ ^{\circ}\mathrm{C}$ ($673\ \mathrm{K}$), higher than the Curie temperature of YIG. FMR spectrum is shown in **Figure 25**.

Figure 25 - Derivative of power absorption. Output obtained from the FMR measurement in sample 1 after second annealing. The experiments ran with rf power at $10\ \mathrm{dbm}$, $\omega_{rf} = 9.4171\ \mathrm{GHz}$, and Gaussmeter scale at $1\ \mathrm{kOe}$.

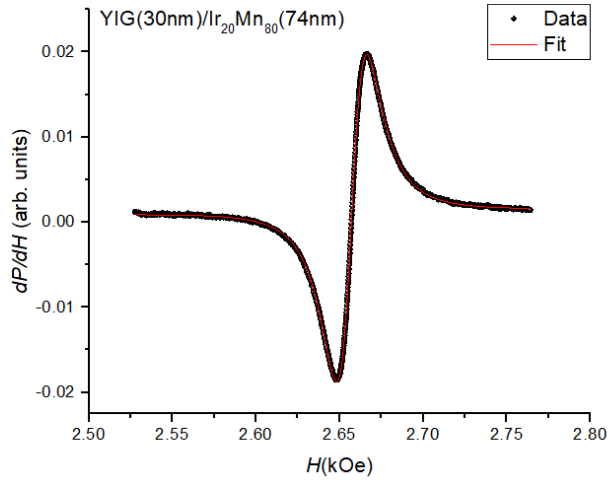

Source: the author.

Figure 26 shows the curve that fits the data with standard deviation of $\sigma = 1.6\ \mathrm{Oe}$. The twofold increase in cubic anisotropy ($H_{c1} = 15\ \mathrm{Oe}$) indicates susbtantial improvement of the crystal structure. Likewise, uniaxial anisotropy was slightly strengthened ($H_u = 5.4\ \mathrm{Oe}$), indicating unidirectional order. On the other hand, exchange bias field has decreased drastically ($H_{EB} = 2\ \mathrm{Oe}$). It is possible that the release of stresses in the lattice have wiped out the magnetic defects at the FM/AFM interface, which otherwise could be sources of exchange bias.

Figure 26 - Plot of resonance field versus applied field angle for sample 1 after second annealing. Red dots stand for data. Blue solid line for fitted curve. Black dashed line for the exchange bias contribution.

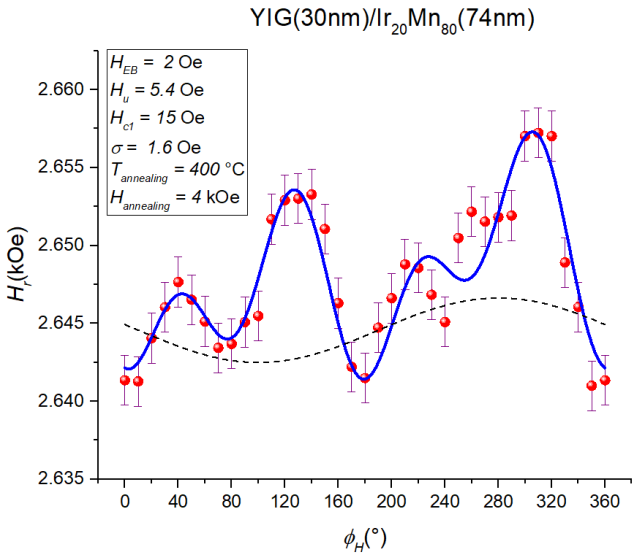

Source: the author.

4.1.2 Sample 2 – YIG(100nm)/IrMn(250nm)

The rate of cooling also is an important parameter in annealing processes. For instance, it is a established practice for induction of uniaxial anisotropy to keep a slow cooling rate at temperatures just above the critical point for ordering; followed by a faster rate to avoid long-range ordering which is detrimental to uniaxial anisotropy in an alloy. We have prepared a sample of YIG(100nm)/$Ir_{20}Mn_{80}$(250nm) and carried annealing similar with before, except that now roughly controlling the cooling rate. The sample was heated up to $600\ ℃$ $(873{,}15\ K)$ and kept at this level for 25 minutes. Then, it was cooled at a rate of $-10°C/min$ until about $195\ ℃$, well below the Currie temperature of YIG. From this point, the sample was let cool down naturally to room temperature.

Comparison of the power absorption spectra at $0°$ and $180°$ (**Figure 27**) shows that from the two resonance modes, one of them shifts while the other remains almost the same, suggesting that the mode of higher magnitude has exchange bias.

Figure 27 - Derivative of power absorption. Output obtained from the FMR measurement in sample 2 after first annealing. The experiments ran with rf power at $1\ \mathrm{dbm}$, $\omega_{rf} = 9.4177\ \mathrm{GHz}$, and Gaussmeter scale at $300\ \mathrm{Oe}$. (a) $180°$. (b) $0°$.

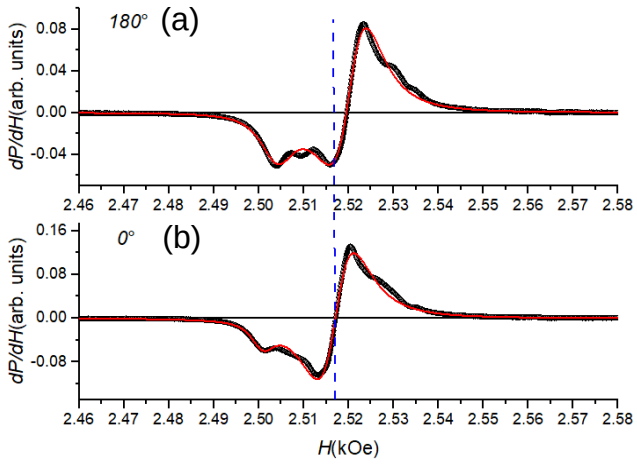

Source: the author.

Figure 28 shows the curve fit with standard deviation of $\sigma = 0.8\ \mathrm{Oe}$. There was $H_{c1} = 8.4\ \mathrm{Oe}$, $H_u = 1.7\ \mathrm{Oe}$, and $H_{EB} = 2\ \mathrm{Oe}$ indicating an increase in crystallographic order, but a weak exchange coupling with the antiferromagnet.

Figure 28 - Plot of resonance field versus applied field angle for sample 2 after first annealing. Red dots stand for data. Blue solid line for fitted curve. Black dashed line for the exchange bias contribution.

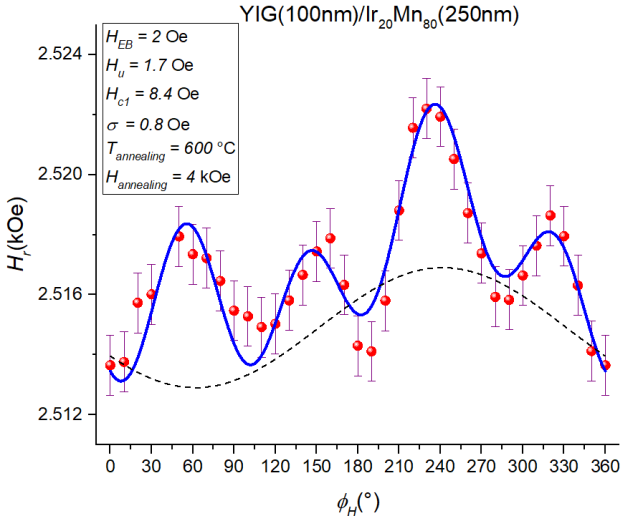

Source: the author.

4.2 Exchange bias in trilayers FM/Sb/AFM

Still on our investigation for exchange bias in YIG/AFM bilayers, YIG (66nm) samples were prepared by LPE following the traditional PbO/B_2O_3 method [32]. The synthesis parameters are found in **Table 12**.

Table 12 - LPE parameters for samples 3 and 4.

Material	Growth time	Growth temperature $(°C)$	Warm up time	Growth rate (rpm)	Spin-off rate (rpm)	Spin-off time
YIG	$1\,\mathrm{min}\,30\,s$	943	$5\,min$	120	700	$10\,s$

Source: the author.

Then, two samples were separated (samples 3 and 4) and layers of IrMn(150nm) and Sb(25nm)/IrMn(150nm), respectively, were sputtering deposited over two of the YIG samples (deposition parameters in **Table 13**). The FMR spectra for each sample are shown in **Figure 29** and **Figure 31**.

Table 13 - Deposition parameters for samples 3 and 4.

Target	Deposition time	Deposition rate $(\mathrm{nm/min})$	Pressure (Torr)	Ag flux (sccm)	Plasma		
					$I(\mathrm{mA})$	$P(\mathrm{W})$	$V(\mathrm{V})$

Sb	6 min	4.3	7.5×10^{-4}	550	50	20	376
IrMn	20 min 16 s	7.4	2.9×10^{-3}	840	50	16	303

Source: the author.

4.2.1 Sample 3 – YIG(66nm)/IrMn(150nm)

Sample 3 is YIG made by LPE, which typically has very low relaxation rate (< 10 Oe). The power absorption spectrum is in **Figure 29**.

Figure 29 - Derivative of power absorption. Output obtained from the FMR measurement in sample 3. The experiments ran with rf power at 1 dbm, $\omega_{rf} = 9.417$ GHz, and Gaussmeter scale at 300 Oe.

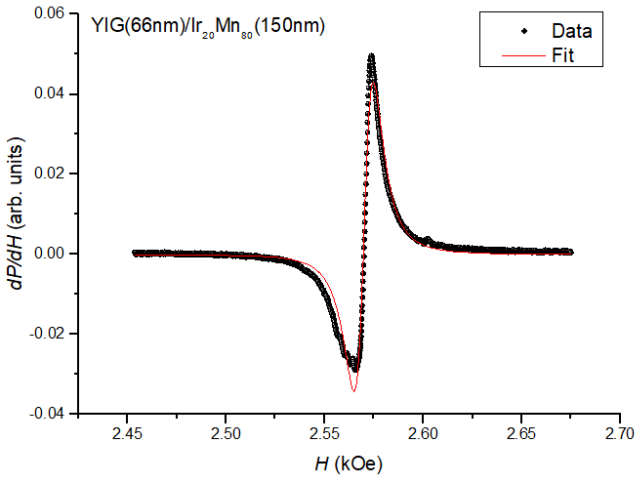

Source: the author.

Figure 30 shows a clear signature of cubic anisotropy for sample 3, with $H_{c1} = 6$ Oe which is typical of YIG grown by LPE. Influences from uniaxial anisotropy and exchange bias were barely found, $H_u = 1$ Oe and $H_{EB} = 0.4$ Oe, and the fit's standard deviation is $\sigma = 0.93$ Oe.

Figure 30 - Plot of resonance field versus applied field angle for sample 3. Red dots stand for data. Blue solid line for fitted curve. Black dashed line for the exchange bias contribution.

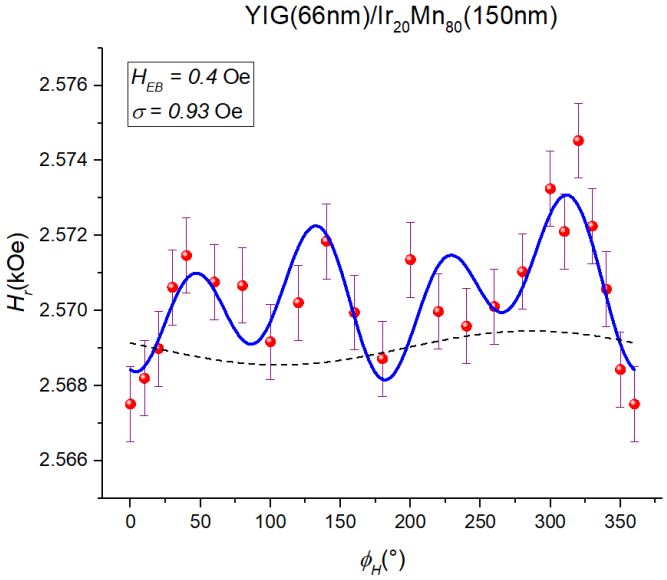

Source: the author.

4.2.2 Sample 4 - YIG(66nm)/Sb(25nm)/IrMn(150nm)

In sample 4 we have tried to evaluate the influence of an antimony interlayer on exchange bias. There are reports of antimony holding on to its topological surface states in Sb(15nm)/YIG bilayers, demonstrated by observing the invariance of spin-pumping signal to the direction of the spin current [1]. If this is the case, the interfacial spin polarization produced by spin-momentum locking may have an effect on the FM magnetization.

Figure 31 shows the FMR power absorption spectrum obtained for sample 4. Due to the good quality of our YIG films made by LPE, magnetostatic modes are excited both below (surface modes) and above (volume modes) the FMR field. This indicates that the current flowing through the Sb layers does not introduce extra damping or change the FMR field.

Figure 31 - Derivative of power absorption. Output obtained from the FMR measurement in sample 4. The experiments ran with rf power at -5 dbm, $\omega_{rf} = 9.4164$ GHz, and Gaussmeter scale at 100 Oe.

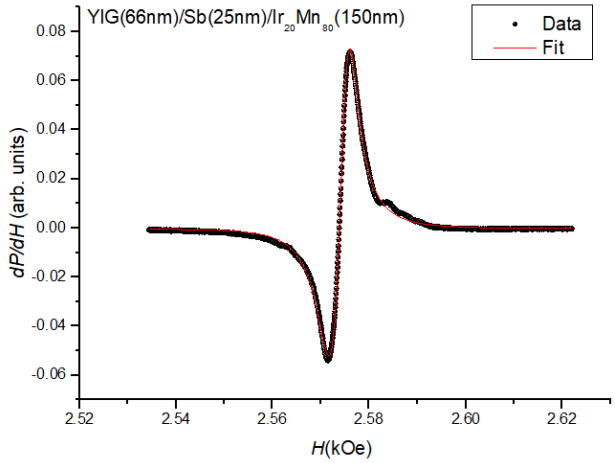

Source: the author.

The curve for the YIG/Sb/IrMn (**Figure 32**) is similar to its no-antimony counterpart, with the difference that the peak near $120°$ is slightly shifted upwards, suggesting the existence of unidirectional anisotropy. Indeed, the fitting (standard deviation $\sigma = 1.7$ Oe) gave exchange bias field of $H_{EB} = 3$ Oe, and, as expected, a dominant cubic anisotropy field of $H_{c1} = 7$ Oe. Uniaxial anisotropy was also found with $H_u = 3.5$ Oe.

Figure 32 - Plot of resonance field versus applied field angle for sample 4. Red dots stand for data. Blue solid line for fitted curve. Black dashed line for the exchange bias contribution.

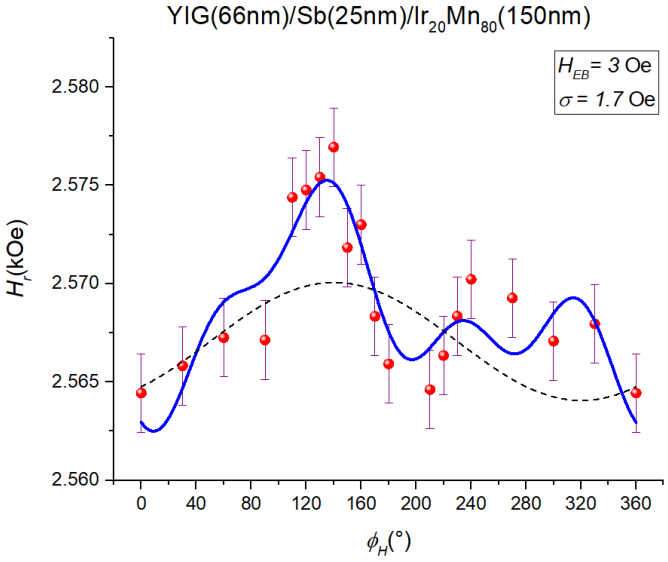

Source: the author.

In order to confirm the FMR result, we have raised the hysteresis loops by the VSM technique (**Figure 33**). The displacement between the $0°$ and $90°$ curves give an estimation of the exchange bias field. In this case, $H_{EB} = 3.2\ \mathrm{Oe}$, which is in good agreement with the FMR measurement.

Figure 33 – VSM measurements at (a) 0° and (b) 90°. Each point corresponds to the average over thirty magnetization values for every applied field.

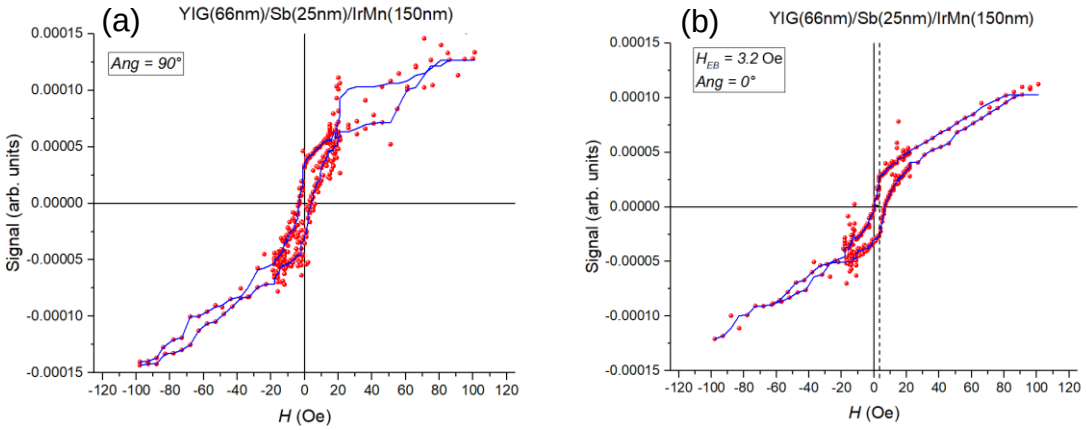

Source: the author.

4.2.3 Sample 5 – Py(12nm)/IrMn(15nm)

Assuming that the previous results were due to antimony's properties, we have decided to verify if a similar effect would happen to another material used as the FM layer, thus giving room to comparison with the results in YIG. For that role permalloy ($Ni_{81}Fe_{19}$) stands out as a natural choice to due to its smooth resonance curves and strong exchanges bias fields. Moreover, it has been shown [35] that antimony in Sb/Py bilayers maintains its surface states at Sb thicknesses up $30\ \mathrm{nm}$.

Invented in 1914, permalloy is a polycrystalline nickel-iron ferromagnetic alloy that features high relative permeability ($\approx 10^5$), very small coercivity, near zero magnetostriction, and significant anisotropic magnetoresistance. Moreover, it has face-centered cubic (fcc) crystal structure with lattice constant of approximately $a = 0.355\ \mathrm{nm}$ in most cases [4,20,40]. For reference, **Figure 34** shows the angular dependence of the resonance field in a regular Py(12nm)/IrMn(15nm) bilayer that gives a clear exchange bias field of $H_{EB} = 63\ \mathrm{Oe}$; while the sputtering parameters are displayed in **Table 14**.

Table 14 - Deposition parameters for sample 5.

Target	Deposition time	Deposition rate $(\mathrm{nm/min})$	Pressure (Torr)	Ag flux (sccm)	Plasma		
					$I(\mathrm{mA})$	$P(\mathrm{W})$	$V(\mathrm{V})$
Py	$2\,\mathrm{min}\,17\,s$	5.23	9.5×10^{-4}	550	50	21	390
$Ir_{20}Mn_{80}$	$2\,\mathrm{min}\,2\,s$	7.4	2.9×10^{-3}	840	50	16	298

Source: the author.

Figure 34 - Plot of resonance field versus applied field angle for sample 5. Red dots stand for data. Blue solid line for fitted curve. Black dashed line for the exchange bias contribution.

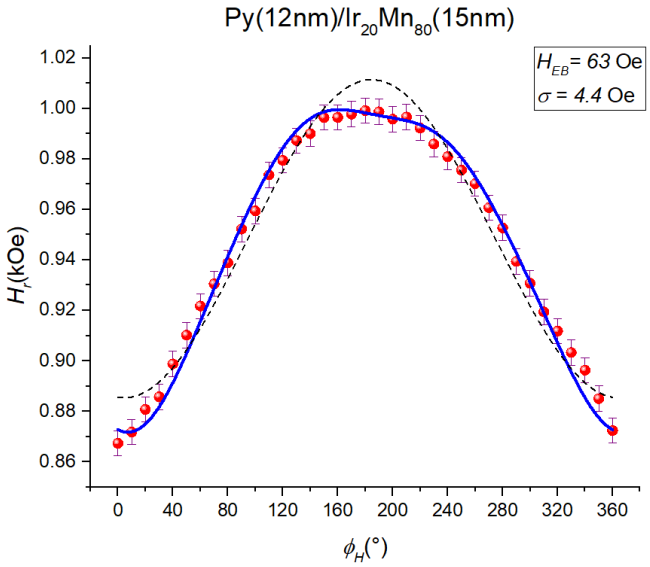

Source: the author.

Next, Py(10nm)/Sb(t)/IrMn(30nm) trilayers ($t = 30, 20, 10, 5\,\mathrm{nm}$) were deposited over a SiO_2 substrate by DC sputtering, corresponding to samples 6, 7, 8 and 9, respectively. The power absorption spectra of the samples are summarized in **Figure 35**.

Figure 35 – Summary of the derivatives of power absorption for several Sb thicknesses. Output obtained from the FMR measurement in samples 6 (d), 7 (c), 8 (b) and 9 (a). The experiments ran with rf power at $20\ \mathrm{dbm}$, and (a) $\omega_{rf} = 9.412\ \mathrm{GHz}$, and Gaussmeter scale at $1\ \mathrm{kOe}$; (b) $\omega_{rf} = 9.414\ \mathrm{GHz}$, and Gaussmeter scale at $300\ \mathrm{Oe}$; (c) $\omega_{rf} = 9.411\ \mathrm{GHz}$, and Gaussmeter scale at $1\ \mathrm{kOe}$; (d) $\omega_{rf} = 9.416\ \mathrm{GHz}$, and Gaussmeter scale at $1\ \mathrm{kOe}$.

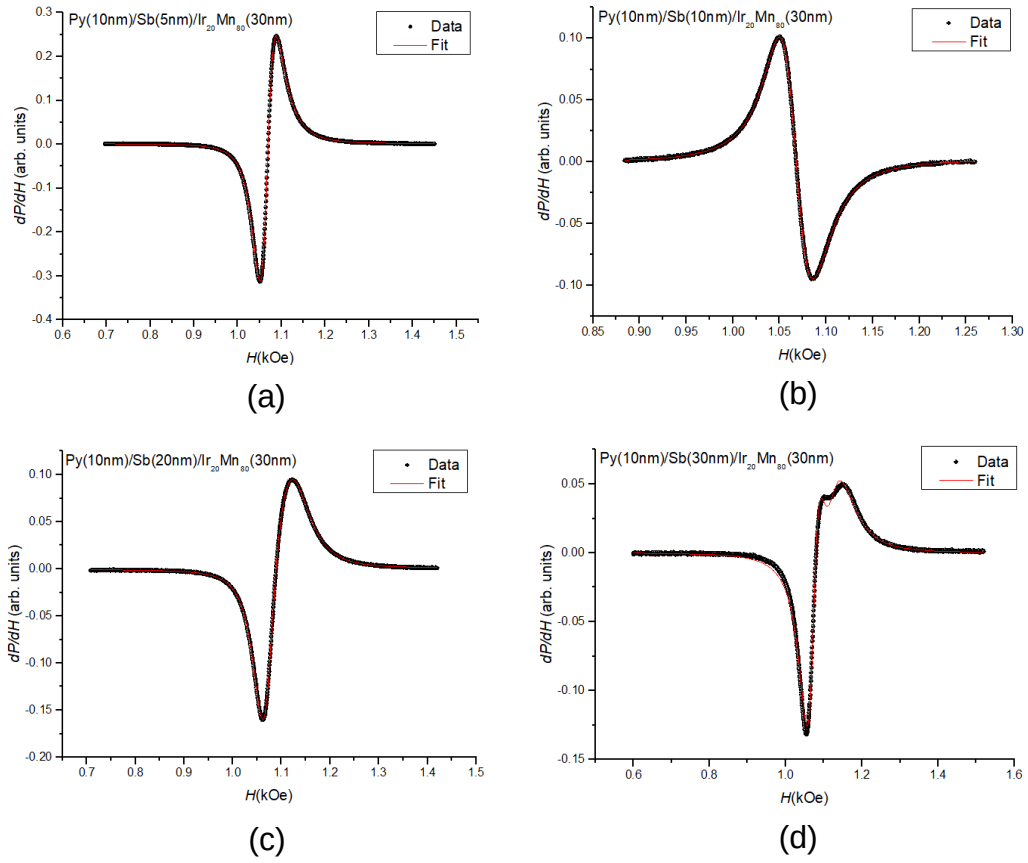

Source: the author.

4.2.4 Sample 6 – Py(10nm)/Sb(30nm)/IrMn(30nm)

For sample 6, the pre-deposition pressure was at $1.6 \times 10^{-7}\ \mathrm{Torr}$ and temperature at $24\ °\mathrm{C}$, and the deposition parameters are given in **Table 15**.

Table 15 - Deposition parameters for sample 6.

Target	Deposition time	Deposition rate $(\mathrm{nm/min})$	Pressure (Torr)	Ag flux (sccm)	Plasma		
					$I(\mathrm{mA})$	$P(\mathrm{W})$	$V(\mathrm{V})$
Py	$1\ \mathrm{min}\ 55\ \mathrm{s}$	5.23	9.5×10^{-4}	550	50	21	390
Sb	$6\ \mathrm{min}\ 59\ \mathrm{s}$	4.29	8×10^{-4}	550	50	18	336
$Ir_{20}Mn_{80}$	$4\ \mathrm{min}\ 3\ \mathrm{s}$	7.4	2.9×10^{-3}	840	50	16	298

Source: the author.

Figure 36 plots the measured resonance fields versus angle in a fashion typical of uniaxial anisotropy and exchange bias combined. The parameters were numerically evaluated, giving exchange bias field $H_{EB} = 2.5\ \mathrm{Oe}$, cubic anisotropy field $H_{c1} = 1.7\ \mathrm{Oe}$, and uniaxial anisotropy field $H_u = 4.4\ \mathrm{Oe}$ with standard deviation $\sigma = 1.5\ \mathrm{Oe}$.

Figure 36 - Plot of resonance field versus applied field angle for sample 6. Red dots stand for data. Blue solid line for fitted curve. Black dashed line for the exchange bias contribution.

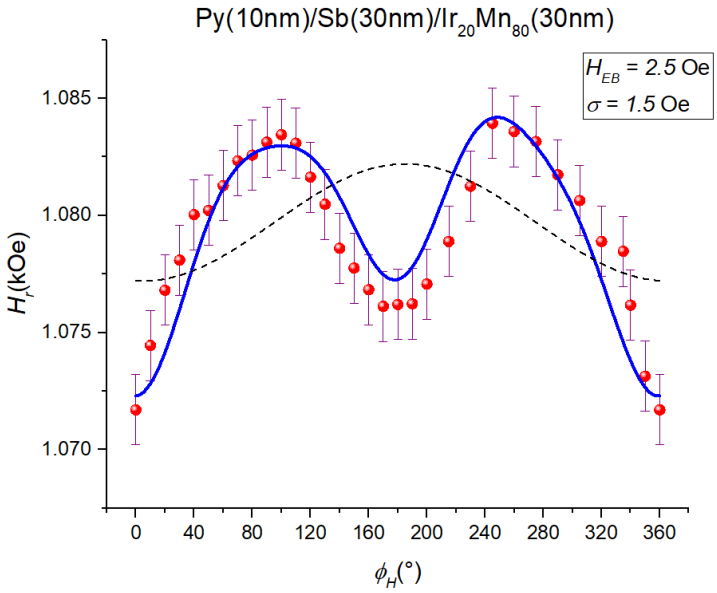

Source: the author.

4.2.5 Sample 7 – Py(10nm)/Sb(20nm)/IrMn(30nm)

For sample 7 the pre-deposition pressure was stabilized at $1.3 \times 10^{-7}\ \mathrm{Torr}$ and the temperature at $23\ °\mathrm{C}$. **Table 16** shows the deposition parameters. The fitted curve in **Figure 37** gives $H_{EB} = 1.4\ \mathrm{Oe}$, $H_u = 2.5\ \mathrm{Oe}$, $H_{c1} = 1.7\ \mathrm{Oe}$ with $\sigma = 0.75\ \mathrm{Oe}$.

Table 16 - Deposition parameters for sample 7.

Target	Deposition time	Deposition rate (nm/min)	Pressure (Torr)	Ag flux (sccm)	Plasma		
					I(mA)	P(W)	V(V)
Py	1 min 55 s	5.23	9.5×10^{-4}	550	50	21	390
Sb	4 min 40 s	4.29	7×10^{-4}	550	50	20	375
$Ir_{20}Mn_{80}$	4 min 3 s	7.4	2.9×10^{-3}	840	50	15	292

Source: the author.

Figure 37 - Plot of resonance field versus applied field angle for sample 7. Red dots stand for data. Blue solid line for fitted curve. Black dashed line for the exchange bias contribution.

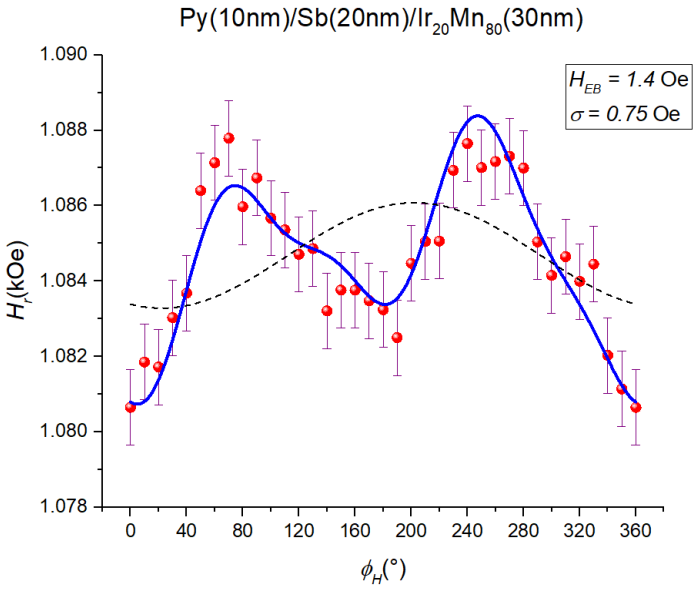

Source: the author.

4.2.6 Sample 8 – Py(10nm)/Sb(10nm)/IrMn(30nm)

Pre-deposition pressure was stabilized at 1.4×10^{-7} Torr, and temperature at 23 °C. Deposition parameters are found in **Table 17**. The fitted curve (**Figure 38**) give $H_{EB} = 0.8$ Oe, $H_u = 2$ Oe, $H_{c1} = 1$ Oe; with $\sigma = 0.8$ Oe.

Table 17 - Deposition parameters for sample 8.

Target	Deposition time	Deposition rate (nm/min)	Pressure (Torr)	Ag flux (sccm)	Plasma		
					I(mA)	P(W)	V(V)
Py	1 min 55 s	5.23	9.5×10^{-4}	550	50	21	390
Sb	2 min 20 s	4.29	8.5×10^{-4}	560	50	19	359
$Ir_{20}Mn_{80}$	4 min 3 s	7.4	2.9×10^{-3}	840	50	15	295

Source: the author.

Figure 38 - Plot of resonance field versus applied field angle for sample 8. Red dots stand for data. Blue solid line for fitted curve. Black dashed line for the exchange bias contribution.

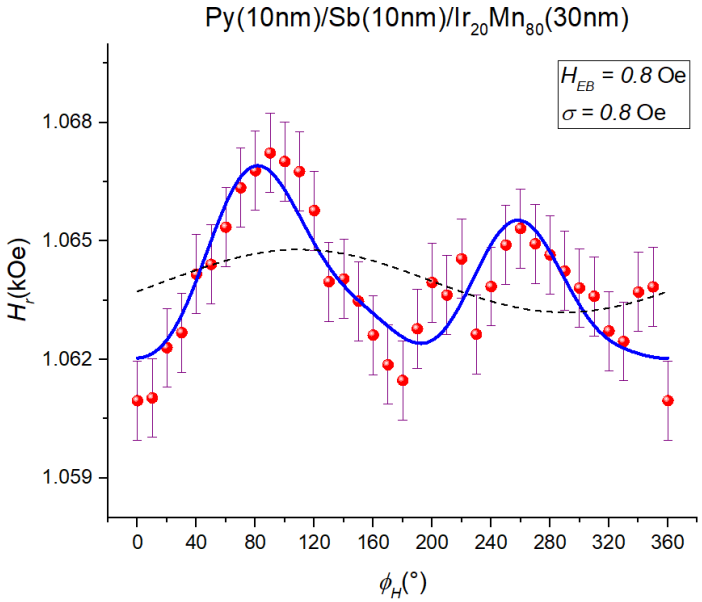

Source: the author.

4.2.7 Sample 9 – Py(10nm)/Sb(5nm)/IrMn(30nm)

Pre-deposition pressure was stabilized at 1.6×10^{-7} Torr, and temperature at 24 °C. Deposition parameters in **Table 18**. The fitted curve (**Figure 39**) gives $H_{EB} = 0.6$ Oe, $H_u = 3.4$ Oe, $H_{c1} = 0$ Oe, with $\sigma = 0.23$ Oe. In this case, uniaxial anisotropy dominates.

Table 18 - Deposition parameters for sample 9.

Target	Deposition time	Deposition rate (nm/min)	Pressure (Torr)	Ag flux (sccm)	Plasma		
					I(mA)	P(W)	V(V)
Py	1 min 55 s	5.23	9.5×10^{-4}	550	50	21	390
Sb	1 min 10 s	4.3	8×10^{-4}	550	50	18	336
$Ir_{20}Mn_{80}$	4 min 3 s	7.4	2.9×10^{-3}	840	50	16	298

Source: the author.

Figure 39 - Plot of resonance field versus applied field angle for sample 9. Red dots stand for data. Blue solid line for fitted curve. Black dashed line for the exchange bias contribution.

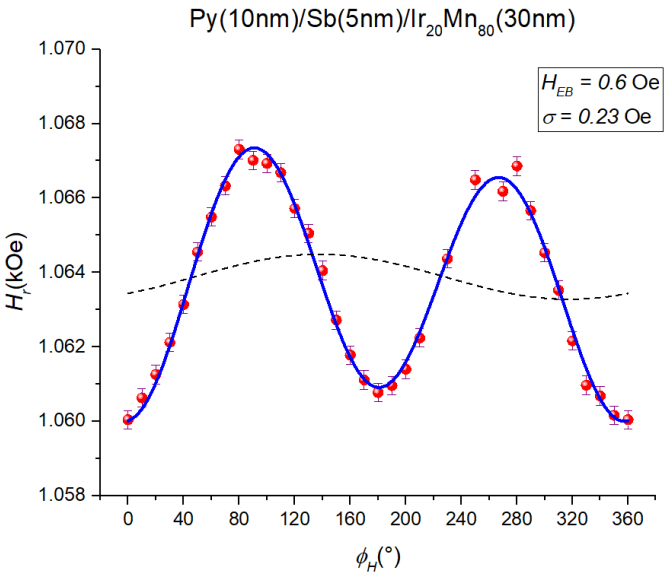

Source: the author.

Figure 40 shows the dependence of exchange bias effective fields versus thickness of the Sb layer. The data was fitted by a 2nd order polynomial curve. It is important to have in mind, however, that in spite of this apparently exotic increase, the estimated exchange bias fields are much lower than those for Py/IrMn without antimony (**Figure 34**), so that further measurements at thicker interlayers are desirable to unambiguously confirm whether this increase is indeed a consistent effect, or random fluctuations.

Figure 40 – Plot of exchange bias effective field versus thickness of antimony layer.

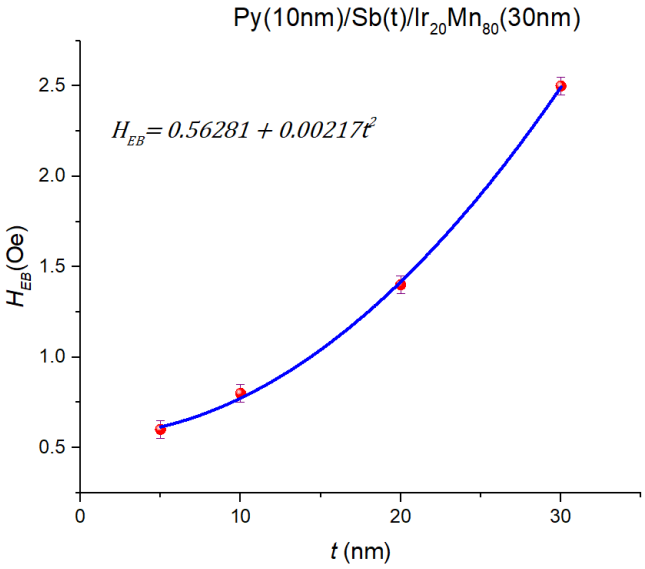

Source: the author.

5 FINAL CONSIDERATIONS

In the first round of experiments, two sputtering deposited YIG/IrMn samples were subjected to magnetic annealing in order to evaluate the heat treatment influence in the crystallographic structure, as well as to tentatively establish the parameters that most effectively induce exchange bias in such films. Indeed, this was accomplished to Sample 1 – YIG(30nm)/IrMn(74nm), that developed exchange bias field of $H_{EB} = 9.3\ \mathrm{Oe}$ after the first annealing (**Figure 24**), corresponding to a sevenfold increase from the field in the same sample prior to annealing, which was measured to be $H_{EB} = 1.4\ \mathrm{Oe}$ [36].

This result was obtained for annealing at temperature $T = 570\ ^{\circ}\mathrm{C}$ followed by natural cooling. On the other hand, longer times at high temperatures and slower cooling rate seemed to be detrimental to exchange bias, while favoring uniaxial anisotropy, as seen in **Figure 26** and **Figure 28** for Sample 1 – YIG(30nm)/IrMn(74nm) after second annealing, and Sample 2 – YIG(100nm)/IrMn(250nm), respectively. Moreover, annealing seemed to strengthen the cubic anisotropy in both cases. A possible explanation to this result is that, as annealing releases stresses in the IrMn crystal lattice it generates lattice order, thereby reducing terraces and steps which, in turn, reduce the number of magnetic domains at the interface that would otherwise contribute to exchange bias.

Alternatively, the discrepancy between the two samples could be caused by the difference in the thermal expansion coefficients of YIG and IrMn, so that the heating and cooling processes may induce strain at the interface of the two mismatched materials, modifying the magnetic properties with strong dependence on the cooling rate and maximum temperature.

The second round of measurements addresses the effect of antimony interlayers in ferromagnet-antiferromagnet arrangements. Antimony is a diamagnetic semimetal known to host topological surface states, thereby drawing much attention for its unique quantum properties. First, measurements on YIG/Sb(25nm)/IrMn were carried out, suggesting the existence of unidirectional anisotropy, having this assumption been tested both by FMR (**Figure 32**) and VSM (**Figure 33**). Looking further onto that surprising result, Py/Sb(t)/IrMn samples with ($t = 5, 10, 20, 30\ \mathrm{nm}$)

were deposited by DC sputtering, hoping to gain further insights by comparison of the responses from YIG and Py.

The results provide evidence of exchange bias acting (faintly) in the trilayers, which could be caused either by the distance action of the FM/AFM coupling persisting through the Sb layer; or by the direct coupling between antimony and the FM. The first explanation seems unlikely since **Figure 40** shows an increase of exchange bias field with the thickness of antimony, which is not consistent with several reports of exponential decay limited to the distance of a few dozens of angstroms based on the RKKY interaction [21,33,34]. Instead, I am inclined to believe that the change in exchange bias is due to different conditions at the interface for the different samples, which brings me back to the second hypothesis: a coupling between antimony's spin-momentum locked electrons and the FM electrons.

As discussed in Section 2.7.5, spin-momentum locking is a facet of Rashba spin-orbit splitting that causes spins' orientations to be locked perpendicular to the electrons' linear momentum. Assuming antimony to be hosting surface states, the spin-pumped current in Sb would be topologically locked, which could result in coupling with the FM spins by the exchange interaction. In fact, there are reports of antimony maintaining its topological surface states in Sb/YIG and Sb/Py interface for Sb thicknesses up to a few dozens of nanometers [1,35], which is compatible with the present results. Moreover, magnetoresistance measurements in topological insulator-based spin-valve devices of Bi_2Se_3 with Ni contact electrodes have found convincing evidence of spin polarization from spin-momentum locked topological surface states influencing the magnetization of adjacent FM layers [37].

If confirmed, the induction of exchange bias mediated by spin-momentum locking could open new avenues in spintronics. For instance, one could control exchange bias intensity by passing current at the Sb surface; or, by finding the polarization of exchange bias, one could estimate the angle of polarization of the topological currents in Sb, as well as their momentum vector.

REFERENCES

[1] ABRÃO, J. E. et al. Probing the spin momentum locking in Rashba surfaces via spin current. **ArXiv**. 2404.14630 (2024). DOI: https://doi.org/10.48550/arXiv.2404.14630. Disponível em: https://arxiv.org/abs/2404.14630. Acesso em 4 jul. 2024.

[2] ALEY, N. P. *et al*., Texture effects in IrMn/CoFe exchange bias systems. **IEEE Transactions on Magnetics**, vol. 44, no. 11, p. 2820-2823. (2008). DOI: 10.1109/TMAG.2008.2001317

[3] BODE, M. *et al.* Chiral magnetic order at surfaces driven by inversion asymmetry. **Nature** 447, 190–193 (2007). DOI: https://doi.org/10.1038/nature05802

[4] BOZORTH, R. M. The permalloy problem. **Rev. Mod. Phys**. 25, 42 (1953). DOI: https://doi.org/10.1103/RevModPhys.25.42

[5] BYCHKOV, Y.A. RASHBA, É.I. Properties of a 2D electron gas with lifted spectral degeneracy. Journal of Experimental and Theoretical Physics Letters, v 39, p 78 (1984).

[6] CHEN, C. **Magnetism and metallurgy of soft magnetic materials**. New York: North-Holland Publishing Co., 1977.

[7] DZYALOSHINSKY, I. A thermodynamic theory of “weak” ferromagnetism of antiferromagnetics. **Journal of Physics and Chemistry of Solids**. V. 4, 4. p. 241-255. (1958). DOI: https://doi.org/10.1016/0022-3697(58)90076-3

[8] EDELSTEIN, V.M. Spin polarization of conduction electrons induced by electric current in two-dimensional asymmetric electron systems. **Solid State Communications.** v 73, 3. p 233-235. DOI: https://doi.org/10.1016/0038-1098(90)90963-C

[9] FUKAMI, S. *et al*. Magnetization switching by spin–orbit torque in an antiferromagnet–ferromagnet bilayer system. **Nature Materials.** v 15, p 535–541 (2016). DOI: https://doi.org/10.1038/nmat4566

[10] GIL-MONSALVE, J. Twofold and fourfold anisotropies in zinc ferrite thin films investigated by ferromagnetic resonance. **Phys. Rev. B**. 105, 014420 (2022). DOI: https://doi.org/10.1103/PhysRevB.105.014420

[11] GRIFFITHS, D. J. **Introduction to electrodynamics**. 4. ed. Upper Saddle River: Prentice Hall, 1999.

[12] JIANG, Z. *et al.* Enhanced spin Seebeck effect signal due to spin-momentum locked topological surface states. **Nature Communications**. 7, 11458 (2016). DOI: https://doi.org/10.1038/ncomms11458

[13] JOHNSTON Hamish. How the Stern-Gerlach experiment made physicists believe in quantum mechanics. Physics World. 2022. Disponível em: https://physicsworld.com/a/how-the-stern-gerlach-experiment-made-physicists-believe-in-quantum-mechanics/. Acesso em: 9 jun. 2024.

[14] KHAN, R. A. *et al*. Magnetic domain texture and the Dzyaloshinskii-Moriya interaction in Pt/Co/IrMn and Pt/Co/FeMn thin films with perpendicular exchange bias. **Physical Review B**. 98, 064413 (2018). DOI: https://doi.org/10.1103/PhysRevB.98.064413

[15] LEIS, A. *et al*. Lifting the spin-momentum locking in ultra-thin topological insulator films. **Advanced Quantum Technologies**. v 4, 2100083 (2021). DOI: https://doi.org/10.1002/qute.202100083

[16] LO, C.K. Instrumentation for Ferromagnetic Resonance Spectrometer. InTech. (2013). DOI: 10.5772/56069. Disponível em: https://www.intechopen.com/chapters/45531. Acesso em: 9 jun. 2024.

[17] MECKLER, S. *et al*. Real-Space Observation of a Right-Rotating Inhomogeneous Cycloidal Spin Spiral by Spin-Polarized Scanning Tunneling Microscopy in a Triple Axes Vector Magnet. Phys. Rev. Lett. **103**, 157201 (2009). DOI: https://doi.org/10.1103/PhysRevLett.103.157201

[18] MENDES, J. B. S. **Investigação de relaxação e anisotropias magnéticas em filmes obliquamente depositados**. 2009. Dissertação (Mestrado em Física) – CCEN, Física, Universidade Federal de Pernambuco, Recife, 2009.

[19] MORIYA, T. Anisotropic superexchange interaction and weak ferromagnetism. **Phys. Rev.** 120, 91. (1960). DOI: https://doi.org/10.1103/PhysRev.120.91

[20] NAHRWOLD, G. Structural, magnetic, and transport properties of Permalloy for spintronic experiments. **J. Appl. Phys**. 108, 013907 (2010). DOI: https://doi.org/10.1063/1.3431384

[21] NAYYEF, H. *et al*. Tunable interplay between exchange coupling and uniaxial magnetic anisotropy in epitaxial CoO/Au/Fe trilayers. **Scientific Reports**. 13: 10902 (2023). DOI: https://doi.org/10.1038/s41598-023-38098-6

[22] PRINCEP, A. J. *et al*. The full magnon spectrum of yttrium iron garnet. **Npj Quantum Materials**. 2(1):63 (2017). DOI: http://dx.doi.org/10.1038/s41535-017-0067-y

[23] REZENDE, S. M. **Fundamentals of magnonics**. 1. ed. Berlim: Spinger, 2020.

[24] REZENDE, S. M. **Introduction to electronic materials and devices**. 1. ed. Berlim: Springer, 2022.

[25] REZENDE, S. M.; MOURA, J. A. S.; AGUIAR, F. M. Ferromagnetic resonance of Fe(111) thin films and Fe(111)/Cu(111) multilayers. **Physical Review B**. V. 49, n. 21, p. 105-109 (1994).

[26] RYU, KS. *et al.* Chiral spin torque at magnetic domain walls**. Nature Nanotech** 8, 527–533 (2013). DOI: https://doi.org/10.1038/nnano.2013.102

[27] SAKURAI, J. J. **Modern quantum mechanics**. 3. ed. Cambridge: Cambridge University Press, 2021.

[28] SATOH, T. *et al*. Spin Oscillations in Antiferromagnetic NiO Triggered by Circularly Polarized Light. **Phys. Rev. Lett**. 105, 077402 (2010). DOI: https://doi.org/10.1103/PhysRevLett.105.077402

[29] SCHULZ, T. *et al.* Emergent electrodynamics of skyrmions in a chiral magnet. **Nature Phys** 8, 301–304 (2012). DOI: https://doi.org/10.1038/nphys2231

[30] SHEN, J. *et al*. Spin-to-charge conversion in Ag/Bi bilayer revisited. **Phys. Rev. Lett.** 126, 197201 (2021). DOI: https://doi.org/10.1103/PhysRevLett.126.197201

[31] SHEN, K. VIGNALE, G. RAIMONDI, R. Microscopic Theory of the Inverse Edelstein Effect. **Phys. Rev. Lett**. 112, 096601 (2014). DOI: https://doi.org/10.1103/PhysRevLett.112.096601

[32] SHONE, M. The technology of YIG film growth. **Circuits Systems and Signal Process**. 4, 89–103 (1985). DOI: https://doi.org/10.1007/BF01600074

[33] SILVA, E. F. *et al*. Asymmetric magnetoimpedance effect in ferromagnetic multilayered biphase films. **Journal of Magnetism and Magnetic Materials**. v. 393. p 260-264 (2015). DOI: https://doi.org/10.1016/j.jmmm.2015.05.079

[34] SILVA, E. F. *et al*. On the nature of the interlayer magnetic interactions in biphase ferromagnetic films. **Scientific Reports**. 13: 4409 (2023). DOI: https://doi.org/10.1038/s41598-023-31563-2

[35] SILVA, E.G. *et al*. Surface-state mediated spin-to-charge conversion in Sb. **Applied Physics Letters**. 123, 202402 (2023). DOI: https://doi.org/10.1063/5.0169242

[36] SOUZA, E. C. **Estudo de fenômenos de interface em heteroestruturas $Y_3Fe_5O_{12}$/(NM e AFM) produzidas por magnetron sputtering**. 2023. Dissertação (Mestrado em Física) – CCEN, Física, Universidade Federal de Pernambuco, Recife, 2023.

[37] TIAN, J. *et al*. Topological insulator based spin valve devices: evidence for spin polarized transport of spin-momentum locked topological surface states. **Solid State Communications**. v. 191, p. 1-5 (2014). DOI: https://doi.org/10.1016/j.ssc.2014.04.005

[38] TISHITOYAN, V. *et al.* Electrical manipulation of ferromagnetic NiFe by antiferromagnetic IrMn. **Phys. Rev. B**. 92, 214406 (2015). DOI: https://doi.org/10.1103/PhysRevB.92.214406

[39] YAO, G. *et al.* Evolution of Topological Surface States in Antimony Ultra-Thin Films. **Sci Rep***.* 3, 2010 (2013). DOI: https://doi.org/10.1038/srep02010

[40] YIN, L. F. *et al*. Magnetocrystalline anisotropy in Permalloy revisited. **Phys. Rev. Lett**. 97, 067203. (2006). DOI: https://doi.org/10.1103/PhysRevLett.97.067203

[41] ZAEZJEV, M.V. *et al.* Crystallization of yttrium-iron garnet (YIG) in thin films: nucleation and growth aspects. **MRS Online Proceedings Library.** 1036, 419 (2007). DOI: https://doi.org/10.1557/PROC-1036-M04-19

[42] ZHANG, P. *et al*. Topological and electronic transitions in a Sb(111) nanofilm: the interplay between quantum confinement and surface effect. **Phys. Rev. B.** 85, 201410(R) (2012). DOI: https://doi.org/10.1103/PhysRevB.85.201410

APPENDIX A - NUMERICAL FITTING

Python code for numeric fitting of FMR curve. Code ran in IDE Visual Studio Code.

```
import numpy as np
import matplotlib.pyplot as plt
import sympy as smp
from scipy import optimize
from scipy.optimize import curve_fit, bisect, minimize,least_squares, fsolve
import pandas as pd
from scipy import interpolate
#algumas dessas bibliotecas não serão usadas
import scipy as sp

#Só para vizualizar os dados do arquivo que deve ser ajustado
Dados = pd.read_excel("")
print(Dados)
Degree = np.array(Dados['Deg'])   #Degree e Degree_rad se refere aos ângulos phi_H
Degree_rad = np.pi*Degree/180
H_resonance = np.array(Dados['Hr'])
Linewidth = np.array(Dados['dH'])
plt.plot(Degree, H_resonance, 'o')
plt.plot(Degree, Linewidth, 'o')
plt.show()
ang_rad = np.linspace(0, 2*np.pi, 500)
ang = 180*ang_rad/np.pi

#definindo as equações que governam a dinâmica da magnetização num experimento de FMR

#Resolver a equação para o modo uniforme de FMR, sob as condições apropriadas, nos permite escrever H_r como uma função de segundo grau
```

```
def A(phi_H,phi_M):
  return (np.cos(phi_M - phi_H))**2

def B(phi_H, phi_M, M_eff, Heb, phi_Heb, Hc1, phi_Hc1, Hc2, Hu, phi_Hu):
  return ((Hc1)*(-0.77775+((0.1111)*(np.sin(2*(phi_M-phi_Hc1)))**2)+(0.44445)*np.cos(4*(phi_M-phi_Hc1)))+Hc2*(-0.11690295+0.1261622*np.cos(4*(phi_M-phi_Hc1)))+(Hu*0.5)*(1+3*np.cos(2*(phi_M-phi_Hu)))+2*Heb*np.cos(phi_M-phi_Heb)+4*np.pi*M_eff)*np.cos(phi_M-phi_H)

def C(phi_H, phi_M, M_eff, Heb, phi_Heb, Hc1, phi_Hc1, Hc2, Hu, phi_Hu, gamma):
  return ((Hc1)*(-0.77775+0.1111*(np.sin(2*(phi_M-phi_Hc1)))**2)+(Hc2*0.11690295)*(-1+np.cos(4*(phi_M-phi_Hc1)))+4*np.pi*M_eff+Heb*(np.cos(phi_M-phi_Heb))-(Hu*0.5)*(1-np.cos(2*(phi_M-phi_Hu))))*(Hc1*0.44445*np.cos(4*(phi_M-phi_Hc1))+Hc2*0.009259259257*np.cos(4*(phi_M-phi_Hc1))+Heb*np.cos(phi_M-phi_Heb)+Hu*np.cos(2*(phi_M-phi_Hu))) - (9.416/gamma)**2



Heb_min = 0.00
Heb_0 = Heb_min + 0.001
Heb_max = 0.01

Hc1_min = 0.00
Hc1_0 = Hc1_min + 0.0005
Hc1_max = 0.03

Hc2_min = 0
Hc2_0 = Hc2_min + 0.05
Hc2_max = 0.1

Hu_min = 0.00
```

```
Hu_0 = Hu_min + 0.001
Hu_max = 0.02

phi_EB_min = (-180)*(np.pi/180)
phi_EB_max = (180)*(np.pi/180)
phi_EB_0 = (phi_EB_min + phi_EB_max)/2


phi_C1_min = (-50)*(np.pi/180)
phi_C1_max = (50)*(np.pi/180)
phi_C1_0 =  (phi_C1_min + phi_C1_max)/2


phi_Hu_min = (-90)*(np.pi/180)
phi_Hu_max = (90)*(np.pi/180)
phi_Hu_0 = (phi_Hu_min + phi_Hu_max)/2

M_eff_min = 0
M_eff_max = 3
M_eff_0 = (M_eff_min + M_eff_max)/2


#Usando f_solve para achar as raízes (É mais simples do que o método da secante)


def Phi_M_equilibrio(phi_M, phi_H, Hr, Hc1, phi_Hc1, Hc2, Hu, phi_Hu):
    return                Hr*np.sin(phi_M-phi_H)-0.11111*Hc1*np.sin(4*(phi_M-phi_Hc1))-
0.037037*Hc2*np.sin(4*(phi_M-phi_Hc1))-0.5*Hu*np.sin(2*(phi_M-phi_Hu))


rootsz = []
for i in range(len(H_resonance)):                                    # (Hc1, AngC1,
Hc2, Hu, phi_Hu)
```

```
   roots = fsolve(Phi_M_equilibrio, x0 = Degree_rad[i], args = (Degree_rad[i], H_resonance[i], Hc1_0, phi_C1_0, Hc2_0, Hu_0, phi_Hu_0), xtol=1.49012e-08) #antes era args = (...0.4, phi_u=0)
   rootsz.append(roots)
#ROOTS = np.array(roots)
phi_M_eq = np.squeeze(np.array(rootsz))
plt.plot(Degree_rad, phi_M_eq,'o')
plt.show()

#Phi_M_equilibrio(phi_H, phi_M, Hr, Hu, phi_U):

#Fazendo o ajuste utlizando o método curve_fit

def H_r(X, M_eff, Heb, phi_Heb, Hc1, phi_Hc1, Hc2, Hu, phi_Hu, gamma):
   phi_H, phi_M = X
   return -0.5*B(phi_H, phi_M, M_eff, Heb, phi_Heb, Hc1, phi_Hc1, Hc2, Hu, phi_Hu)/A(phi_H,phi_M) + 0.5*np.sqrt((B(phi_H, phi_M, M_eff, Heb, phi_Heb, Hc1, phi_Hc1, Hc2, Hu, phi_Hu))**2 - 4*A(phi_H,phi_M)*C(phi_H, phi_M, M_eff, Heb, phi_Heb, Hc1, phi_Hc1, Hc2, Hu, phi_Hu, gamma))/A(phi_H,phi_M)



def H_r_plot(phi_H, phi_M, M_eff, Heb, phi_Heb, Hc1, phi_Hc1, Hc2, Hu, phi_Hu, gamma):
   return -0.5*B(phi_H, phi_M, M_eff, Heb, phi_Heb, Hc1, phi_Hc1, Hc2, Hu, phi_Hu)/A(phi_H,phi_M) + 0.5*np.sqrt((B(phi_H, phi_M, M_eff, Heb, phi_Heb, Hc1, phi_Hc1, Hc2, Hu, phi_Hu))**2 - 4*A(phi_H,phi_M)*C(phi_H, phi_M, M_eff, Heb, phi_Heb, Hc1, phi_Hc1, Hc2, Hu, phi_Hu, gamma))/A(phi_H,phi_M)

phi_M_interp = np.interp(ang_rad, Degree_rad, phi_M_eq)
#                                                    # (1-Meff, 2-Heb, 3-|_°, 4-Hc1, 5-|_º, 6-Hc2,  7-Hu,  8-|_°, 9-gamma)                    (1-Meff, 2-Heb, 3-|_°, 4-Hc1, 5-|_º, 6-Hc2,  7-Hu,  8-|_°, 9-gamm9a)
```

```
Hr_opt, Hr_cov = curve_fit(H_r, (Degree_rad, phi_M_eq), H_resonance, p0 = [M_eff_0, Heb_0, phi_EB_0, Hc1_0, phi_C1_0, Hc2_0, Hu_0, phi_Hu_0, 2.96], bounds = ((M_eff_min, Heb_min, phi_EB_min, Hc1_min, phi_C1_min, Hc2_min, Hu_min, phi_Hu_min, 2.9),(M_eff_max, Heb_max, phi_EB_max, Hc1_max, phi_C1_max, Hc2_max, Hu_max, phi_Hu_max, 2.98)), maxfev = 2000000)

M_eff, Heb, phi_eb, Hc1, phi_Hc1, Hc2, Hu, phi_Hu, gamma = Hr_opt
#Erro = np.sqrt(np.diag(Hr_cov))

print("Valores:", "M_eff", Hr_opt[0], "Heb", Hr_opt[1], "phi_Heb", (180/np.pi)*Hr_opt[2], "Hc1", Hr_opt[3], "phi_Hc1", (180/np.pi)*Hr_opt[4], "Hc2", Hr_opt[5], "Hu" , Hr_opt[6],"phi_Hu", (180/np.pi)*Hr_opt[7], "gamma", Hr_opt[8], sep = '\n')
#print("Erros:", Erro)
plt.plot(ang, H_r_plot(ang_rad, phi_M_interp, Hr_opt[0], Hr_opt[1], Hr_opt[2], Hr_opt[3], Hr_opt[4], Hr_opt[5], Hr_opt[6], Hr_opt[7], Hr_opt[8]), 'r', linewidth = 2)
plt.plot(Degree, H_resonance, 'o')
plt.show()


r = H_resonance - H_r_plot(Degree_rad, phi_M_eq, Hr_opt[0], Hr_opt[1], Hr_opt[2], Hr_opt[3], Hr_opt[4], Hr_opt[5], Hr_opt[6], Hr_opt[7], Hr_opt[8])
Desvio_padrao = np.sqrt(np.average(r**2))
print("Desvio Padrão:", Desvio_padrao)


#refazendo o ajuste realimentando os parâmetros obtidos anteriormente

for i in range(1, 50):
    rootsz = []
    for i in range(len(H_resonance)):
        roots = fsolve(Phi_M_equilibrio, x0 = Degree_rad[i], args = (Degree_rad[i], H_resonance[i], Hr_opt[3], Hr_opt[4], Hr_opt[5], Hr_opt[6], Hr_opt[7]), xtol=1.49012e-08)
```

```
        rootsz.append(roots)

    phi_M_eq = np.squeeze(np.array(rootsz))

# (1-Meff, 2-Heb, 3-|_°, 4-Hc1, 5-|_º, 6-Hc2,  7-Hu,  8-|_°, 9-gamma)
    Hr_opt, Hr_cov = curve_fit(H_r, (Degree_rad, phi_M_eq), H_resonance, p0 = [Hr_opt[0], Hr_opt[1], Hr_opt[2], Hr_opt[3], Hr_opt[4], Hr_opt[5], Hr_opt[6], Hr_opt[7], Hr_opt[8]], bounds = ((M_eff_min, Heb_min, phi_EB_min, Hc1_min, phi_C1_min, Hc2_min, Hu_min, phi_Hu_min, 2.9),(M_eff_max, Heb_max, phi_EB_max, Hc1_max, phi_C1_max, Hc2_max, Hu_max, phi_Hu_max, 2.98)),  maxfev = 2000000)

    M_eff, Heb, phi_eb, Hc1, phi_Hc1, Hc2, Hu, phi_Hu, gamma = Hr_opt
    r = H_resonance - H_r_plot(Degree_rad, phi_M_eq, Hr_opt[0], Hr_opt[1], Hr_opt[2], Hr_opt[3], Hr_opt[4], Hr_opt[5], Hr_opt[6], Hr_opt[7], Hr_opt[8])
    Desvio_padrao = np.sqrt(np.average(r**2))

#plotando
print("Valores:", "M_eff", Hr_opt[0], "Heb", Hr_opt[1], "phi_Heb", (180/np.pi)*Hr_opt[2], "Hc1", Hr_opt[3], "phi_Hc1", (180/np.pi)*Hr_opt[4], "Hc2", Hr_opt[5], "Hu" , Hr_opt[6],"phi_Hu", (180/np.pi)*Hr_opt[7], "gamma", Hr_opt[8],  sep = '\n')
plt.plot(ang, H_r_plot(ang_rad, phi_M_interp, Hr_opt[0], Hr_opt[1], Hr_opt[2], Hr_opt[3], Hr_opt[4], Hr_opt[5], Hr_opt[6], Hr_opt[7], Hr_opt[8]), 'r', linewidth = 2)
plt.plot(ang, H_r_plot(ang_rad, phi_M_interp, Hr_opt[0], Hr_opt[1], Hr_opt[2], 0, 0, 0, 0, 0, Hr_opt[8]), color = 'black', linewidth = 1, linestyle = "dashed")
#plt.plot(ang, H_r_plot(ang_rad, phi_M_interp, Hr_opt[0], 0, 0, Hr_opt[3], Hr_opt[4], 0, 0, 0, Hr_opt[8]), color = 'black', linewidth = 0.5, linestyle = "dashed")
#plt.plot(ang,  H_r_plot(ang_rad,  phi_M_interp,  Hr_opt[0],  0,  0,  0,  0,  0,  Hr_opt[6], Hr_opt[7], Hr_opt[8]), color = 'black', linewidth = 0.5, linestyle = "dashed")

#curva teste
#plt.plot(ang, H_r_plot(ang_rad, phi_M_interp, Hr_opt[0], Hr_opt[1], Hr_opt[2], 0.005, Hr_opt[4], 0, Hr_opt[6], Hr_opt[7], Hr_opt[8]), color = 'black', linewidth = 1, linestyle = 'dashed')
```

```
plt.errorbar(Degree, H_resonance, fmt = 'o',  yerr = 0.005, ecolor = 'blue', elinewidth = 1)
plt.show()

print("Desvio Padrão:", Desvio_padrao)

# Exportando o ajuste
#GERAL
#Hr = H_r_plot(ang_rad, phi_M_interp, Hr_opt[0], Hr_opt[1], Hr_opt[2], Hr_opt[3], Hr_opt[4], Hr_opt[5], Hr_opt[6], Hr_opt[7], Hr_opt[8])

#Exchange Bias apenas
Hr = H_r_plot(ang_rad, phi_M_interp, Hr_opt[0], Hr_opt[1], Hr_opt[2], 0, 0, 0, 0, 0, Hr_opt[8])



resultadosFMR = open('ResultsFMR.txt','w')
resultadosFMR.write("Ang (°)" + " "+ "Hr (kOe)") # Titulo do arquivo de saida
resultadosFMR.write("\n")#Pula uma linha no arquivo de saida
for i in range(0,500):
    resultadosFMR.write(str(180*ang_rad[i]/np.pi)+'     '+str(Hr[i])+'\n')
resultadosFMR.close()
```